

NEAR-ULTRAVIOLET SPECTROSCOPY OF STAR-FORMING GALAXIES FROM eBOSS: SIGNATURES OF UBIQUITOUS GALACTIC-SCALE OUTFLOWS

GUANGTUN BEN ZHU^{1,12}, JOHAN COMPARAT^{2,3}, JEAN-PAUL KNEIB^{4,5}, TIMOTHÉE DELUBAC⁴, ANAND RAICHOOR⁶,KYLE S. DAWSON⁷, JEFFREY NEWMAN⁸, CHRISTOPHE YÈCHE⁶, XU ZHOU⁹, AND DONALD P. SCHNEIDER^{10,11}¹ Department of Physics & Astronomy, Johns Hopkins University, 3400 N. Charles Street, Baltimore, MD 21218, USA; guangtun@jhu.edu² Instituto de Física Teórica, UAM/CSIC, Universidad Autónoma de Madrid, Cantoblanco, E-28049 Madrid, Spain³ Departamento de Física Teórica, Universidad Autónoma de Madrid, Cantoblanco, E-28049 Madrid, Spain⁴ Laboratoire d'astrophysique, Ecole Polytechnique Fédérale de Lausanne, Observatoire de Sauverny, 1290 Versoix, Switzerland⁵ Aix Marseille Université, CNRS, LAM (Laboratoire d'Astrophysique de Marseille), UMR 7326, F-13388, Marseille, France⁶ CEA, Centre de Saclay, Irfu/SPP, F-91191 Gif-sur-Yvette, France⁷ Department of Physics and Astronomy, University of Utah, Salt Lake City, UT 84112, USA⁸ PITT PACC, Department of Physics and Astronomy, University of Pittsburgh, Pittsburgh, PA 15260, USA⁹ Key Laboratory of Optical Astronomy, National Astronomical Observatories, Chinese Academy of Sciences, Beijing, 100012, China¹⁰ Department of Astronomy and Astrophysics, The Pennsylvania State University, University Park, PA 16802, USA¹¹ Institute for Gravitation and the Cosmos, The Pennsylvania State University, University Park, PA 16802, USA

Received 2015 July 28; accepted 2015 October 29; published 2015 December 8

ABSTRACT

We present rest-frame near-ultraviolet (NUV) spectroscopy of star-forming galaxies (SFGs) at $0.6 < z < 1.2$ from the Extended Baryon Oscillation Spectroscopic Survey (eBOSS) in SDSS-IV. One of the eBOSS programs is to obtain $2''$ (about 15 kpc) fiber spectra of about 200,000 emission-line galaxies (ELGs) at redshift $z \gtrsim 0.6$. We use the data from the pilot observations of this program, including 8620 spectra of SFGs at $0.6 < z < 1.2$. The median composite spectra of these SFGs at $2200 \text{ \AA} < \lambda < 4000 \text{ \AA}$ feature asymmetric, preferentially blueshifted non-resonant emission, Fe II*, and blueshifted resonant absorption, e.g., Fe II and Mg II, indicating ubiquitous outflows driven by star formation at these redshifts. For the absorption lines, we find a variety of velocity profiles with different degrees of blueshift. Comparing our new observations with the literature, we do not observe the non-resonant emission in the small-aperture ($< 40 \text{ pc}$) spectra of local star-forming regions with the *Hubble Space Telescope*, and find the observed line ratios in the SFG spectra to be different from those in the spectra of local star-forming regions, as well as those of quasar absorption-line systems in the same redshift range. We introduce an outflow model that can simultaneously explain the multiple observed properties and suggest that the variety of absorption velocity profiles and the line ratio differences are caused by scattered fluorescent emission filling in on top of the absorption in the large-aperture eBOSS spectra. We develop an observation-driven, model-independent method to correct the emission infill to reveal the true absorption profiles. Finally, we show that the strengths of both the non-resonant emission and the emission-corrected resonant absorption increase with [O II] $\lambda\lambda 3727, 3730$ rest equivalent width and luminosity, with a slightly larger dependence on the former. Our results show that the eBOSS and future dark-energy surveys (e.g., Dark Energy Spectroscopic Instrument survey and Prime Focus Spectrograph survey) will provide rich data sets of rest-frame NUV spectroscopy for astrophysical applications.

Key words: galaxies: evolution – galaxies: ISM – intergalactic medium – quasars: absorption lines – surveys – ultraviolet: galaxies

1. INTRODUCTION

Spectroscopy is one of the most important tools in modern astronomy. Historically, ground-based observations have mostly been focused on the optical window of the spectrum because of the extinction effects of the Earth's atmosphere and the low brightness of most cosmological sources. In the rest-frame near-ultraviolet (NUV) range at $2000 \text{ \AA} \lesssim \lambda \lesssim 3000 \text{ \AA}$, the most-studied sources are quasars (e.g., Schmidt 1963; Francis et al. 1991; Vanden Berk et al. 2001) and quasar absorption-line systems (e.g., Burbidge & Kinman 1966; Bergeron 1986; Steidel & Sargent 1992; Churchill et al. 2000) at moderate redshifts ($0.5 \lesssim z \lesssim 2.5$), thanks to the high energy-conversion efficiency of supermassive black holes. After space-based telescopes became available, such as the *International Ultraviolet Explorer* (IUE) and the *Hubble Space Telescope* (HST), astronomers started to explore the rest-frame UV part of the spectral energy distributions (SEDs) of

stars and galaxies. Most of the space-based observations are dedicated to the far-UV (FUV) window at $\lambda \lesssim 2000 \text{ \AA}$ because of the large number of transitions available at those energies, leaving the NUV window of the SEDs of stars and galaxies as largely unexplored territory. Most of our knowledge about galaxy SEDs in the rest-frame NUV have originated from recent observations with the 8-m or larger telescopes such as the Keck and VLT telescopes (e.g., Martin & Bouché 2009; Weiner et al. 2009; Rubin et al. 2011; Erb et al. 2012; Talia et al. 2012).

The most useful spectral features in the rest-frame NUV have been the resonant¹³ absorption lines induced by the low-ionization species Mg II and Fe II in the interstellar medium (ISM) and/or circumgalactic medium (CGM). In the spectra of star-forming galaxies (SFGs), these absorption lines are observed to be almost always blueshifted from the systemic

¹² Hubble Fellow.¹³ We refer to a transition between two terms as a resonant transition if and only if the lower energy level is the lowest (ground) level of the ground term. See Appendix A for clarification.

velocity of the galaxy, which serves as direct evidence for ubiquitous outflows driven by star formation (Tremonti et al. 2007; Martin & Bouché 2009; Weiner et al. 2009; Rubin et al. 2010, 2014; Erb et al. 2012; Kornei et al. 2012; Martin et al. 2012; Talia et al. 2012).

More recently, observations have also revealed the non-resonant emission features Fe II^* in the NUV spectra of SFGs (Rubin et al. 2011; Erb et al. 2012; Kornei et al. 2012, 2013; Talia et al. 2012; Tang et al. 2014). These non-resonant emission lines are likely caused by scattered fluorescent photons after the occurrence of resonant absorption. As the non-resonant emission lines in the FUV (e.g., Shapley et al. 2003; Jones et al. 2012), they have provided a new means to study the radiative transfer physics in the complex baryon processes in galaxy evolution (e.g., Rubin et al. 2011; Prochaska et al. 2011; Scarlata & Panagia 2015).

The non-resonant emission, e.g., Fe II^* , was sometimes referred to as fine-structure emission in the literature, because the lower energy level of the transition is an excited level due to fine-structure splitting, as opposed to the ground level for the corresponding resonant transition. The term *fine-structure emission*, however, is used more often for the emission between two fine-structure levels (with different J -values) in the same term (with the same L, S), which usually occurs in the infrared (IR), such as $[\text{C II}] \lambda 157.7 \mu\text{m}$. To avoid confusion, we here simply use the term *non-resonant emission* and reserve *fine-structure emission* for those infrared emission lines. We also label the (permitted) non-resonant emission lines with a right superscript asterisk “*,” although the origin of this convention appears to have been lost in the literature.¹⁴

The fine-structure splitting causes multiple transitions, i.e., multiplets, with energies only slightly different from each other. In her pioneering multiplet tables (Moore 1945, 1950), Charlotte E. Moore grouped the multiplets in ascending order of excited terms and this numbering convention has been widely used since. We follow the same convention for the multiplets in the UV (Moore 1950, 1952), though we skip the numbering of multiplets in the optical as in the recent literature. In Appendix A, we summarize our choices of conventions and also present the atomic data needed in this analysis for references.

In the last decade, the detection of the baryon acoustic oscillation (BAO) in the large-scale distribution of galaxies (Cole et al. 2005; Eisenstein et al. 2005) has shifted the focus of observational cosmology to massive redshift surveys over the entire observable sky, and we are now in the course of measuring the scale of BAO as a function of cosmic time and chronicling the expansion history of the universe. Among them are the Extended Baryon Oscillation Spectroscopic Survey (eBOSS, Dawson et al. 2015) within the fourth phase of the Sloan Digital Sky Survey (SDSS-IV, M. Blanton et al. 2015, in preparation), the Dark Energy Spectroscopic Instrument survey (DESI, Schlegel et al. 2011; Levi et al. 2013), and the Prime Focus Spectrograph survey (PFS, Takada et al. 2014). These programs will obtain optical spectra in the observer frame for tens of millions of galaxies at redshift $0.6 \lesssim z \lesssim 2.0$, providing unprecedentedly rich spectroscopic data sets with the coverage in the rest-frame NUV.

Among the new BAO projects, the eBOSS survey started taking data in Fall 2014. One of the large-scale structure tracers in eBOSS is emission-line galaxies (ELGs). We have obtained about 12,000 ELG spectra across the redshift range $0 < z \lesssim 1.5$ in the pilot observations, conducted to optimize targeting strategies. We discuss the whole sample briefly and focus on the NUV spectroscopy of 8620 ELGs at redshift $0.6 < z < 1.2$. We describe the observations and the data set in detail in Section 2.

The rest of the paper is organized as follows. In Section 3, we present the composite spectrum of ELGs in the NUV and compare it with those of quasar absorption-line systems and local star-forming (SF) regions. We interpret the observations with a spherical gas outflow model in Section 4. In Section 5, we investigate the dependence of the spectral features on the $[\text{O II}] \lambda\lambda 3727, 3730$ properties. We summarize our results in Section 6. When necessary, we assume the Λ CDM cosmogony, with $\Omega_\Lambda = 0.7$, $\Omega_m = 0.3$, and $H_0 = 70 \text{ km s}^{-1} \text{ Mpc}^{-1}$. Throughout the paper, we use vacuum wavelength and some of the lines are therefore labeled as 1 Å longer than if labeled with the air wavelength, such as $[\text{O III}] \lambda 5008$.

2. DATA

2.1. The eBOSS Survey

The eBOSS survey is the cosmology survey within SDSS-IV, an extension of the BOSS survey (Dawson et al. 2013) in SDSS-III (Eisenstein et al. 2011). Over a six-year period beginning in Fall 2014, eBOSS will observe four independent tracers of the underlying density field: luminous red galaxies (LRGs), quasars, $\text{Ly}\alpha$ forest, and ELGs, and measure the cosmological distances as a function of redshift with BAO as a standard ruler and record the expansion history of the universe at $0.6 \lesssim z \lesssim 2.3$.

The eBOSS survey uses the same two identical, multi-object spectrographs as in BOSS (Smee et al. 2013) on the 2.5-m SDSS Telescope (Gunn et al. 2006) at the Apache Point Observatory in New Mexico. Each spectrograph is equipped with two cameras, one blue and one red, with a dichroic splitting the light at roughly 6000 Å and a combined coverage spanning between 3600 and 10400 Å. The spectral resolution \mathcal{R} is 1560–2270 in the blue and 1850–2650 in the red channel, with a mean approximately $\bar{\mathcal{R}} \approx 2000$. The spectrographs are fed by 1000 optical fibers (500 for each), covering a field of view (FOV) of about 7.5 square degrees. The aperture diameter of the fibers is 2", smaller than 3" in SDSS-I/II. The typical total exposure time for each pointing is about 75 minutes.

eBOSS selects targets primarily based on the SDSS imaging, obtained through a set of *ugriz* filters (Fukugita et al. 1996) with a wide-field camera (Gunn et al. 1998) in a drift-scan mode. As the desired targets are fainter than those in SDSS I-III, in order to achieve high targeting efficiency, eBOSS includes supplementary imaging data with other instruments, including the infrared photometry (Lang et al. 2014) by the *Wide-field Infrared Survey Explorer* (WISE, Wright et al. 2010), the *U*-band imaging from the South Galactic Cap *U*-band Sky Survey (SCUSS)¹⁵ conducted at the 2.3-m Bok telescope at the Kitt Peak National Observatory, and the deep *grz* imaging with the Dark Energy Camera (DECam, Flaugher

¹⁴ In *Symbols, Units, Nomenclature and Fundamental Constants in Physics*, or the “Red Book,” compiled by International Union of Pure and Applied Physics (IUPAP), the authors recommended this convention for excited atomic levels (see Section 2.1, Cohen et al. 1987).

¹⁵ <http://batc.bao.ac.cn/Uband/>

et al. 2012) on the 4-m Blanco telescope at the Cerro Tololo Inter-American Observatory (CTIO) in Chile.

The spectral-reduction and redshift-fitting pipeline in eBOSS is a continuation of the BOSS pipeline (Bolton et al. 2012), improved to yield required performance on spectra with a lower signal-to-noise ratio (S/N) than in BOSS. Like BOSS, eBOSS classifies objects and derives redshifts based upon principal-component-analysis (PCA) templates for quasars and galaxies, and archetypal templates for stars, though the team is currently exploring an alternative approach that is fully based on archetypal templates. For the analysis presented here, we use the results derived from the pipeline version v5_7_8, which still uses the PCA templates for galaxies and quasars. The pipeline flags a redshift with a warning (ZWARNING) based on various quantitative criteria, such as a small χ^2 difference between the best and second-best fits. Tests have shown that the ZWARNING is conservatively defined and the redshift success rate for objects with ZWARNING==0 is better than 99%. We only use objects classified as a GALAXY with ZWARNING==0 in this analysis.

For more details regarding the eBOSS survey, we refer the reader to Dawson et al. (2015).

2.2. Emission-line Galaxies

ELGs are one of the four tracers targeted in eBOSS. The primary tracer of the large-scale structures in BAO observations (at $z \lesssim 1$) has been LRGs (Eisenstein et al. 2001), because of their broadband brightness and well-understood SEDs. At higher redshift, however, most of the distinctive features of LRGs, such as the 4000 Å break, G4300-band, and MgH/Mg b absorption bands, are redshifted into the Meinel hydroxyl forest. Blueward of the 4000 Å break, the cool giant stars dominating the continuum emit little flux, which makes spectral classification and redshift determination difficult. Moreover, the number density of red galaxies is lower at higher redshift due to galaxy evolution (e.g., Bell et al. 2004; Faber et al. 2007; Moustakas et al. 2013), rendering them less useful for cosmological purposes. On the other hand, the cosmic star formation rate (SFR) density increases precipitously with redshift, and at $z \sim 1$, is about an order-of-magnitude higher than at present (e.g., Madau et al. 1996; Hopkins 2004; Madau & Dickinson 2014). SFGs exhibit the strong [O II] $\lambda\lambda 3727, 3730$ emission feature, which is a doublet distinguishable at a medium spectral resolution $\mathcal{R} \sim 4000$. The number density of [O II] $\lambda\lambda 3727, 3730$ emitters increases steadily with redshift up to $z \sim 2$ (e.g., Zhu et al. 2009; Comparat et al. 2015b; Sobral et al. 2015). The next-generation BAO surveys, e.g., DESI (Schlegel et al. 2011; Levi et al. 2013) and PFS (Takada et al. 2014), will primarily target these [O II] emitters at redshift $z > 1$.

At redshift $z \lesssim 1$, the strong emission lines of SFGs enhance their brightness in the optical (in the observer frame), facilitating their detection even in the relatively shallow SDSS imaging. Comparat et al. (2013) demonstrated that it is feasible to conduct an ELG survey with the BOSS spectrographs that can achieve the number density and the volume coverage required for BAO measurements at $0.6 \lesssim z \lesssim 1.0$, with targets selected from the SDSS imaging. As the continuum of SFGs is dominated by the emission of hot O/B stars in the rest-frame NUV and that of dust and polycyclic aromatic hydrocarbons (PAHs) in the IR, u/U -band and/or IR data can help improve the targeting efficiency of these objects. We have been working

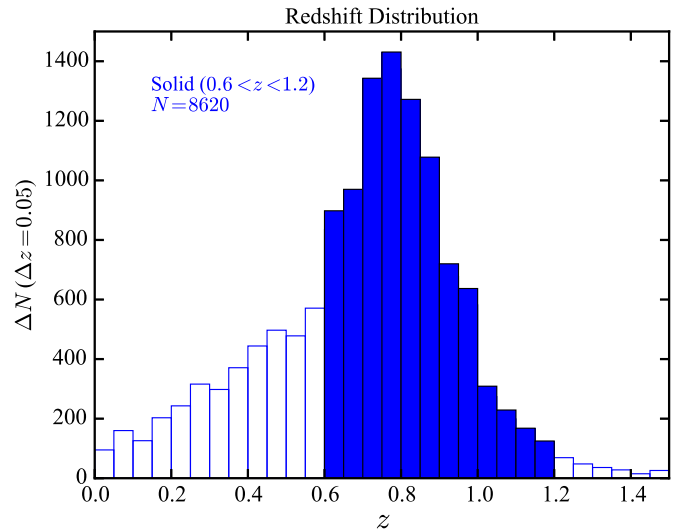


Figure 1. Redshift distribution of all emission-line galaxies (ELGs) from the eBOSS pilot observations. The solid area shows 8620 galaxies at $0.6 < z < 1.2$.

on optimizing the ELG selection strategies with additional data, including the U -band photometry from SCUSS, the IR photometry from WISE, and the deeper grz imaging with DECam.

Favorable weather during SDSS-III led to an early completion of the BOSS survey. A fraction of the remaining time was allocated to an eBOSS pilot program known as the Sloan Extended Quasar, ELG, and LRG Survey (SEQUELS, Alam et al. 2015). In Fall 2014, within eBOSS, we also conducted a series of pilot observations to test possible techniques for the ELG target selection. With data from these pilot observations, the team is currently investigating different selection algorithms to maximize the targeting efficiency (Comparat et al. 2015a; T. Delubac et al. 2015, in preparation; Jovel et al. 2015; Raichoor et al. 2015). The ELG cosmology survey will begin in Fall 2016, the third year of eBOSS, with the optimal selection strategy to be defined from these pilot data and investigations. The survey aims at obtaining secure redshift for about 200,000 ELGs at $0.6 \lesssim z \lesssim 1.0$ and measuring the BAO scale with an accuracy of about 2% at an effective redshift $\langle z \rangle \sim 0.8$.

For more details regarding the ELG target selections and the cosmological applications, we refer the reader to references above and Dawson et al. (2015) and Zhao et al. (2015).

2.3. The ELGs from the eBOSS Pilot Observations

In total, the BOSS/SEQUELS ancillary program and the early eBOSS pilot observations provided about 12,000 ELGs spanning $0 < z \lesssim 1.5$, peaked at $z \sim 0.8$. We show the redshift distribution in Figure 1. In Figure 2, we present the median composite spectrum of all the ELGs, in the wavelength range $2000 \text{ Å} < \lambda < 7500 \text{ Å}$. As we included *all* the ELGs in this composite spectrum, the objects contributing at each wavelength are different, with high-redshift objects dominating in the NUV and low-redshift ones in the optical. The composite spectrum appears as a typical active SFG spectrum (e.g., Kennicutt 1992). We have labeled the prominent features in the figure. In the optical, it features strong hydrogen Balmer recombination emission on top of relatively weak stellar

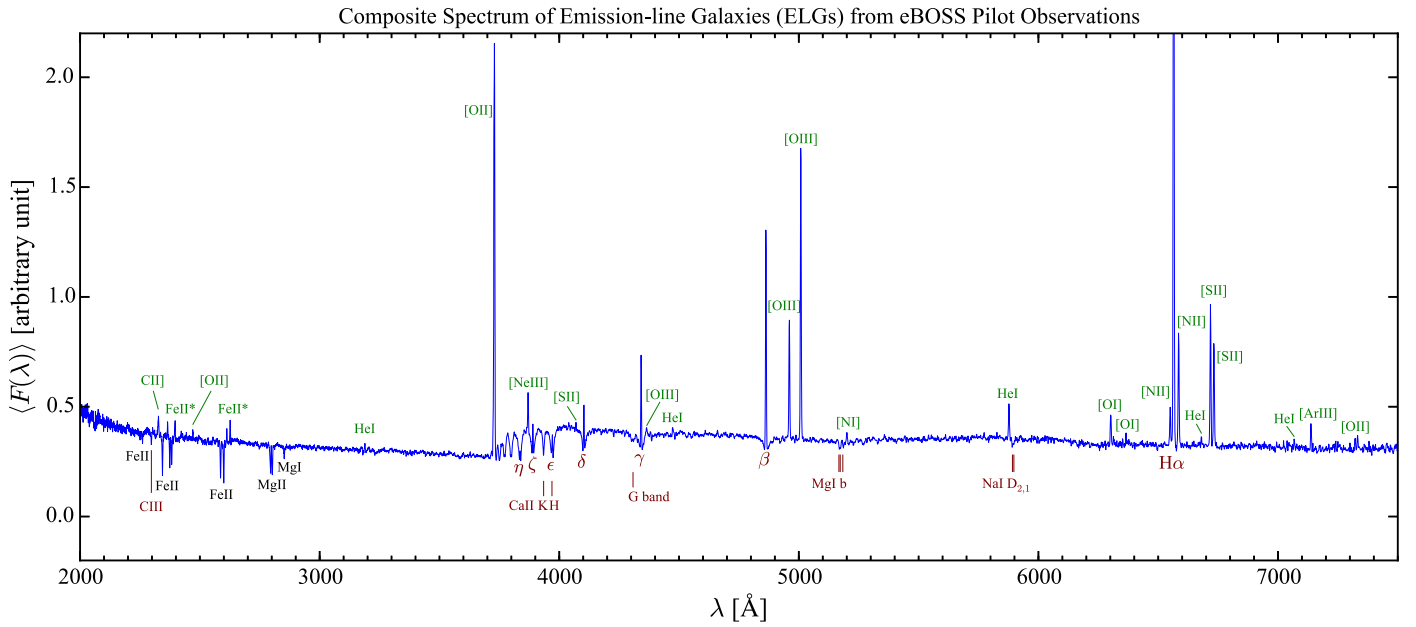


Figure 2. Median composite spectrum of all ELGs (at $0 < z \lesssim 1.5$) at $2000 \text{ \AA} < \lambda < 7500 \text{ \AA}$ from the eBOSS pilot observations. We label emission features in green, stellar absorption features in brown, and ISM/CGM absorption lines in black. The Greek symbols indicate hydrogen Balmer lines, which appear as nebular recombination emission on top of stellar absorption.

Balmer absorption, strong nebular forbidden lines due to collisionally excited metal atoms, e.g., N, O, N⁺, O⁺, S⁺, O²⁺, Ne²⁺, and Ar²⁺. As the BOSS spectrographs cover the [O III] $\lambda 5008$ up to redshift $z \sim 1.0$, we expect that eBOSS will provide an important opportunity for studies of the ISM properties, such as the gas-phase metallicity, in strong SFGs at moderate redshift. The full composite spectrum also displays some relatively weak stellar metal absorption lines, e.g., the Fraunhofer Ca II H & K, G4300-band, Mg I b, and Na I D lines. We summarize the identified lines in the list given in Appendix A.

Comparat et al. (2015a) describes the full sample in detail and we refer the reader to that paper for more information. The mean precision of the redshift at $z \sim 0.8$ is about 20 km s^{-1} thanks to the strength of the emission lines. From the SED fitting of the composite spectra with different line strengths, the average stellar mass (M_*) at $z \sim 0.8$ is about $10^{10} M_\odot$. The investigations of the physical properties of individual galaxies, such as stellar mass (M_*), SFR, and metallicity, are ongoing and will be presented in future papers.

The redshift coverage of the ELG observations at $z > 0.6$ allows us to probe the NUV part of their SEDs, as shown in Figure 2. The composite spectrum between 2900 \AA and the Balmer Break at 3646 \AA is essentially featureless except for the weak He I $\lambda 3189$ emission line. Blueward of 2900 \AA , we see strong absorption lines similar to those in intervening quasar absorption-line systems, Mg I, Mg II and Fe II, and non-resonant Fe II* emission as well as the C II] emission. The underlying stellar continuum rises toward higher energy, as is typical of hot O/B stellar spectra. We fit a power law, $f(\lambda) \propto \lambda^\beta$, to the continuum between 2000 and 2200 \AA and obtain a slope $\beta \sim -2.1$, as expected for an SED dominated by O/B stellar emission in the UV. In the rest of the paper, we will focus on the absorption and emission features in the NUV.

3. NEAR-ULTRAVIOLET SPECTROSCOPY

3.1. The NUV ELG Sample

The eBOSS pilot observations have obtained spectra for a large sample of ELGs at redshift $z > 0.6$ with rest-frame NUV coverage, providing us with a good opportunity to investigate the gas processes associated with these objects. We here focus on the wavelength range between 2200 and 4000 \AA . We choose the shorter wavelength limit so as to cover Fe II $\lambda 2250$ and Fe II $\lambda 2261$, and the longer limit to cover [O II] $\lambda \lambda 3727, 3730$. To ensure the same wavelength coverage for all the objects and thus the same contributing objects at all the wavelengths, we select ELGs between redshift 0.6 and 1.2 , which include 8620 objects.

As discussed in Section 2.1, we use the reduction outputs based on the spectroscopic pipeline version v5_7_8, and consider only objects classified as a GALAXY with no redshift warning, i.e., ZWARNING==0. The classification selection automatically rejects broad-line active galactic nuclei (AGNs). We do not make further cuts in our sample selection. At the redshifts we are interested in, some of the lines required in the narrow-line AGN classification schemes (e.g., Baldwin et al. 1981), such as H α and [N II] $\lambda 6585$, are not covered by eBOSS. For those with [O III] $\lambda 5008$ and H β measurements (at $z \lesssim 1$), based on the blue optical color and line ratios (e.g., Trouille et al. 2011; Yan et al. 2011), we expect the fraction of narrow-line AGNs to be at most a few percent. We also do not expect many low-ionization nuclear emission-line regions (LINERs, Heckman 1980) in our sample. The ELGs are selected to be blue galaxies, while the majority of LINERs are found in red galaxies (e.g., Ho et al. 1997). We therefore expect the line emission in the integrated spectra of the eBOSS ELGs to be dominated by contributions from SF activities and will use the terms ELGs and SFGs interchangeably.

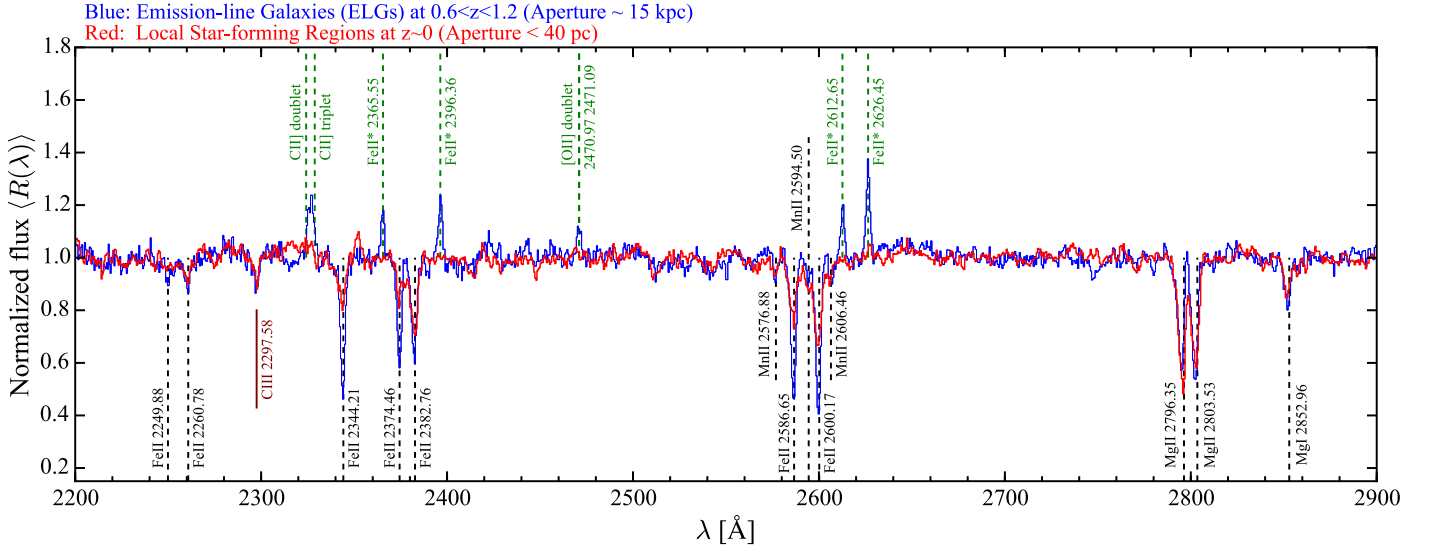


Figure 3. Composite continuum-normalized spectrum of 8620 ELGs at $0.6 < z < 1.2$ (blue). We show the rest-frame positions of emission features with vertical green dashed lines and those of ISM/CGM absorption lines with black dashed lines. The brown solid line marks the stellar photospheric absorption feature C III $\lambda 2298$. The red line shows the composite spectrum of 2310 intervening quasar absorption-line systems with $W_0^{\lambda 2796} > 2 \text{ \AA}$ in the same redshift range.

3.2. The Method

The average S/N per pixel in the continuum region of the individual ELG spectra is low ($\lesssim 1$) and does not allow precise measurements of the absorption features for single objects. To study the gas associated with the ELGs, we construct high-S/N composite continuum-normalized spectra. We use a median estimator, which is less prone to extreme outliers. However, we also tested our analysis with the arithmetic mean estimator and found consistent results, with differences in relative dependences smaller than 1σ .

For each observed spectrum, $F(\lambda)$, we first blueshift it back to its rest frame on a common wavelength grid. We choose the common wavelength grid to have the same logarithmic (or equivalently, velocity) spacing as in the observer frame, i.e., with $d \log_{10} \lambda = 10^{-4}$ or $d\nu = 69 \text{ km s}^{-1}$. In the blueshifting process, we interpolate the spectrum with the cubic-B spline method¹⁶, as in the standard SDSS pipeline. We then mask out absorption and emission features and fit a cubic polynomial function through the rest of the spectrum. Using the best-fit polynomial function as an estimate of the underlying continuum, $\hat{F}_{\text{cont}}(\lambda)$, we normalize the observed spectrum to obtain the continuum-normalized spectrum suited for absorption studies:

$$R(\lambda) \equiv \frac{F(\lambda)}{\hat{F}_{\text{cont}}(\lambda)}. \quad (1)$$

For a given sample, we construct a median composite spectrum of all the continuum-normalized spectra (in the rest frame). Finally, we fit a quadratic polynomial function to the composite spectrum, again with absorption and emission features masked out, to remove any large-scale residuals, though skipping this final step has a negligible effect on the

results. We designate the final composite as $\langle R(\lambda) \rangle$:

$$\langle R(\lambda) \rangle \equiv \left\langle \frac{F(\lambda)}{\hat{F}_{\text{cont}}(\lambda)} \right\rangle. \quad (2)$$

Since we mostly work with composite spectra, we will drop the ensemble symbol $\langle \rangle$ in the text for simplicity.

We quantify the absorption and emission strength in the continuum-normalized spectra with the rest equivalent width W_0 . We define the rest equivalent widths for absorption and emission in such a way that they are both positive. For absorption, the rest equivalent width is given by

$$W_0^{\text{absorption}} \equiv \int_{\lambda_{\min}}^{\lambda_{\max}} [1 - R(\lambda)] d\lambda, \quad (3)$$

and for emission, it is defined as

$$W_0^{\text{emission}} \equiv \int_{\lambda_{\min}}^{\lambda_{\max}} [R(\lambda) - 1] d\lambda, \quad (4)$$

where the integration range ($\lambda_{\min} < \lambda < \lambda_{\max}$) encloses the absorption/emission profile.

Throughout the paper, unless otherwise specified, we estimate the measurement uncertainties for a given sample by bootstrapping (i.e., with replacement) 100 times.

3.3. The Composite Continuum-normalized Spectrum

Figure 3 presents the median composite spectrum of the 8620 ELGs at $0.6 < z < 1.2$ in the wavelength range $2200 \text{ \AA} < \lambda < 2900 \text{ \AA}$. In Figure 4, we zoom in on the most prominent absorption and emission features for a more detailed illustration, and also include the part in the wavelength range $3000 \text{ \AA} < \lambda < 4000 \text{ \AA}$. We have omitted the part between 2900 and 3000 \AA since it is featureless (see Figure 2). To guide the eye, we mark the rest-frame positions of the identified features.

The line features in the NUV can be categorized into three primary groups¹⁷ based upon their origins: stellar photospheric

¹⁶ As the spacing is identical before and after interpolation, linear interpolation yields almost the same results.

¹⁷ In the FUV, stellar wind features comprise another major class of spectral features.

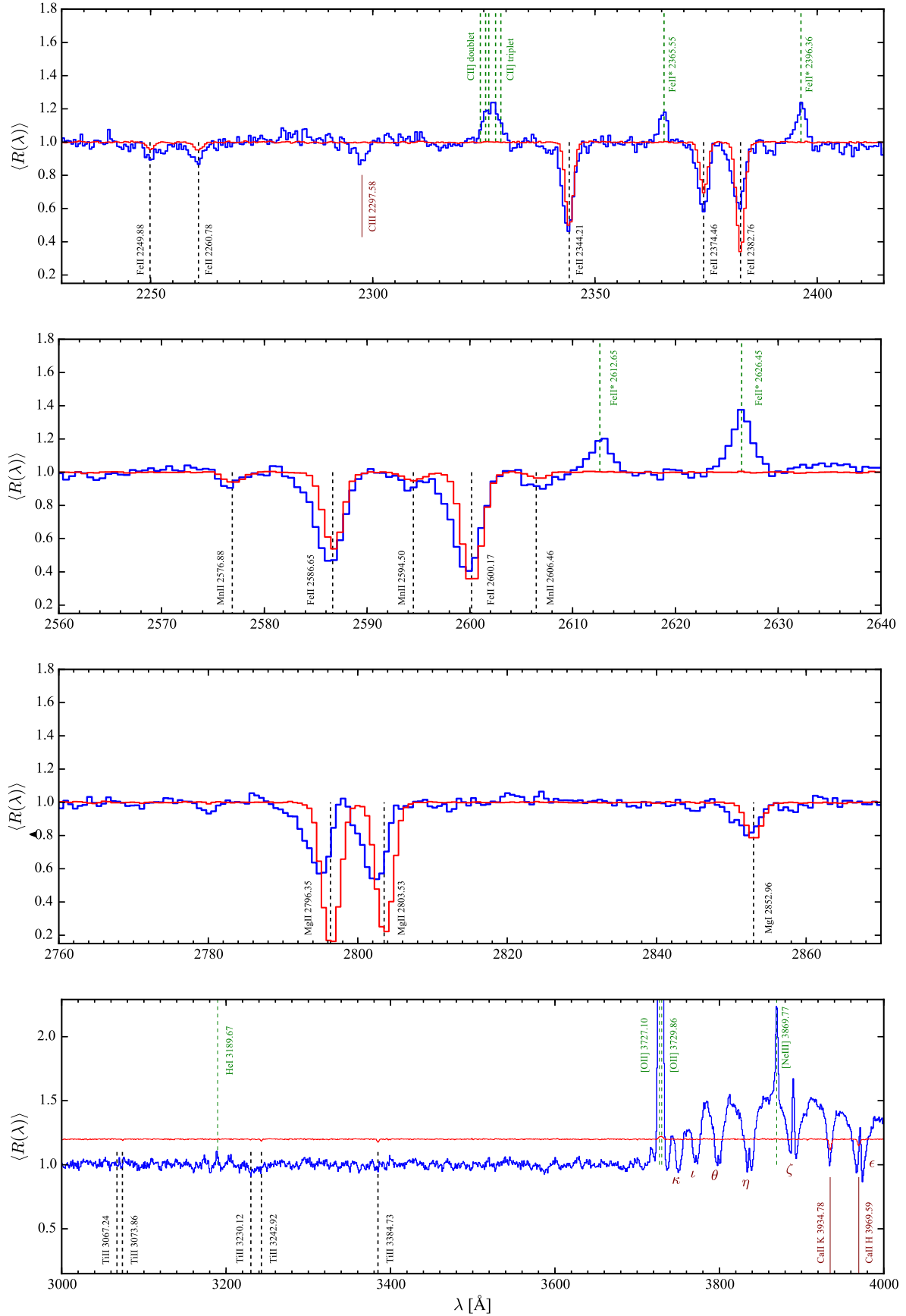


Figure 4. Composite continuum-normalized spectrum of ELGs (blue), zoomed in on prominent features and compared with the composite spectrum of quasar absorbers (red) as in Figure 3. In addition, the bottom panel shows the spectra at $3000 \text{ \AA} < \lambda < 4000 \text{ \AA}$, where we have shifted the quasar absorber composite upward by 0.2 for clarity.

absorption lines, nebular emission lines, and absorption/emission lines due to gas in the ISM and CGM. The last category includes combined effects caused by both the ISM and CGM and is the focus of this work. We briefly discuss the observed features in these groups before investigating the ISM/CGM features in detail.

3.3.1. Stellar Photospheric Absorption Features

At $2200 \text{ \AA} < \lambda < 2900 \text{ \AA}$, we are able to identify only one photospheric absorption line, C III at 2297.58 \AA . However, in subsampling exercises with bootstrapping and jackknife, we notice that there are some weak but persistent features that are not due to noise (also see Section 3.5 below). We do not identify these weak stellar features because the NUV part of the O/B star SEDs has not been sufficiently explored in either theory or observations. The most recent work was by Rodríguez-Merino et al. (2005, the UVBLUE library)¹⁸, who built a suite of stellar spectral templates in the NUV based on the atmospheric model code ATLAS9 (Kurucz 1992; Castelli et al. 1997) and, for O/B stars, compared the model spectra with a few low-resolution spectra taken by *IUE* in 1980s. Although the shape of the underlying stellar continuum is well-understood ($\beta \sim -2.0$, e.g., Kinney et al. 1993, and Section 2.3), the absorption features in theoretical calculations and observations do not match each other. For example, we do not detect the O III line at 2496 \AA predicted by the models in our composite spectrum, nor was it detected in the *IUE* observations of O/B stars (Fanelli et al. 1992; Rodríguez-Merino et al. 2005).

At $3000 \text{ \AA} < \lambda < 4000 \text{ \AA}$, the prominent stellar absorption features are the well-known Balmer series at $\lambda > 3646 \text{ \AA}$, and Ca II H (3969.59 \AA) & K (3934.77 \AA) lines. The Ca II doublet, however, likely has a large contribution from the gaseous Ca^+ in the ISM/CGM (see, e.g., Zhu & Ménard 2013b; Murga et al. 2015).

3.3.2. Nebular Emission Features

Between 2200 and 2900 \AA , we identify two nebular emission features with high confidence: semi-forbidden C II] at about 2326 \AA and forbidden [O II] at about 2471 \AA . The C II] feature is a blend including five transitions from the doublet and the triplet between the ground state and first excited state: C II] $\lambda\lambda 2324, 2325$ and C II] $\lambda\lambda 2326, 2328, 2329$. The [O II] feature is a doublet at 2470.90 and 2471.10 \AA , due to the transitions between the ground state and the second excited state of O^+ . For comparison, the [O II] $\lambda\lambda 3727, 3730$ doublet is due to the transitions between the ground state and the first excited state of O^+ . Both the C II] and [O II] emission lines were observed in H II regions by *IUE* (Dufour 1987). As the low-ionization nebular emission lines in the optical spectra of SFGs, e.g., [O II] $\lambda\lambda 3727, 3730$, [N II] $\lambda\lambda 6550, 6585$ and [S II] $\lambda\lambda 6718, 6733$, they must be dominated by the emission from H II regions, where the UV photons from O/B stars ionized the elements in the surrounding gas to low-ionization states (e.g., Strömgren 1939), though diffuse ionized gas in the ISM, e.g., the warm ionized medium (WIM, McKee & Ostriker 1977), also contributes to the integrated emission (e.g., Reynolds 1984). C^+ can also be abundant in a cooler medium (e.g., photodissociation regions, or PDRs, Tielens &

Hollenbach 1985) because the ionization potential of neutral carbon (11.26 eV) is lower than that of hydrogen or oxygen (both are $\sim 13.6 \text{ eV}$; see Appendix A). It is interesting to note that, though C II] in the NUV has been hardly studied, the fine-structure emission of the C^+ ground term at $157.7 \mu\text{m}$ in the IR is known to be a major coolant in the ISM (Dalgarno & McCray 1972). [C II] $\lambda 157.7 \mu\text{m}$ can be observed for objects at $z \sim 1$ in the submillimeter (e.g., Stacey et al. 2010), thus for the ELG targets in eBOSS and future BAO surveys.

We tentatively identify [Ne IV] (not labeled) at about 2424 \AA , a doublet at 2422.56 and 2425.14 \AA , due to the transitions between the ground state and the first excited state of the triply ionized Ne^{3+} . In SFGs, this doublet is observed mostly in planetary nebulae (e.g., Koeppen & Aller 1987), supernova remnants (e.g., Blair & Panagia 1987), and other environments hotter than H II regions, as the ionization potential of Ne^{2+} (63.4 eV) is larger than He^+ (54.4 eV).

At $3000 < \lambda < 4000 \text{ \AA}$, besides Balmer recombination lines and [O II] $\lambda\lambda 3727, 3730$, we also observe [Ne III] at $\lambda = 3869.86 \text{ \AA}$. Highly sensitive to the ionization parameter, the [Ne III] emission can be combined with [O II] and used to probe the metallicity and other properties of the ISM (Nagao et al. 2006; Levesque & Richardson 2014). There is also a He I line at 3889.74 \AA (not labeled), which is blended with Balmer H ζ . Between 2900 \AA and the Balmer break at 3646 \AA , we only detect the weak He I emission at 3188.67 \AA , which likely sits on top of He I absorption commonly associated with O/B stars (e.g., Morrison 1975).

3.3.3. ISM/CGM Absorption and Emission Features

Most of the absorption lines between 2200 and 2900 \AA are induced by gas in the ISM and/or the CGM, providing us with a unique tool to probe the diffuse gas that is otherwise elusive. From low to high energy, we identify the following lines due to different species:

1. Mg I $\lambda 2853$ (UV1);
2. the Mg II $\lambda\lambda 2796, 2804$ doublet (UV1)¹⁹;
3. the Mn II $\lambda\lambda 2577, 2594, 2606$ triplet (UV1);
4. Fe II $\lambda 2600$ and $\lambda 2587$ (UV1), Fe II $\lambda 2383$ and $\lambda 2374$ (UV2), Fe II $\lambda 2344$ (UV3), Fe II $\lambda 2261$ (UV4), and Fe II $\lambda 2250$ (UV5).

Between 3000 and 4000 \AA , the Ca II H & K lines also trace a significant fraction of gas in the ISM/CGM. All these absorption lines are also commonly seen in intervening quasar absorption-line systems (see the next subsection).

We identify four non-resonant Fe II* emission lines with high confidence:

1. Fe II* $\lambda 2626$ and $\lambda 2613$ (UV1), Fe II* $\lambda 2396$ (UV2), and Fe II* $\lambda 2366$ (UV3).

To illustrate the relationships between the resonant absorption and these non-resonant emission lines, we use the Fe II UV1 multiplet group as an example.

Figure 5 presents the energy-level diagram of Fe II UV1, showing the transitions between the ground state and the first excited state of Fe II. We refer the reader to Appendix A for a

¹⁸ <http://www.inaoep.mx/~modelos/uvblue/uvblue.html>

¹⁹ Compared to the absorption induced by gas in the ISM/CGM, we expect the intrinsic Mg I $\lambda 2853$ and Mg II $\lambda\lambda 2796, 2804$ absorption in the spectra of O/B stars to be very weak, even for metal-rich stars (e.g., Rodríguez-Merino et al. 2005).

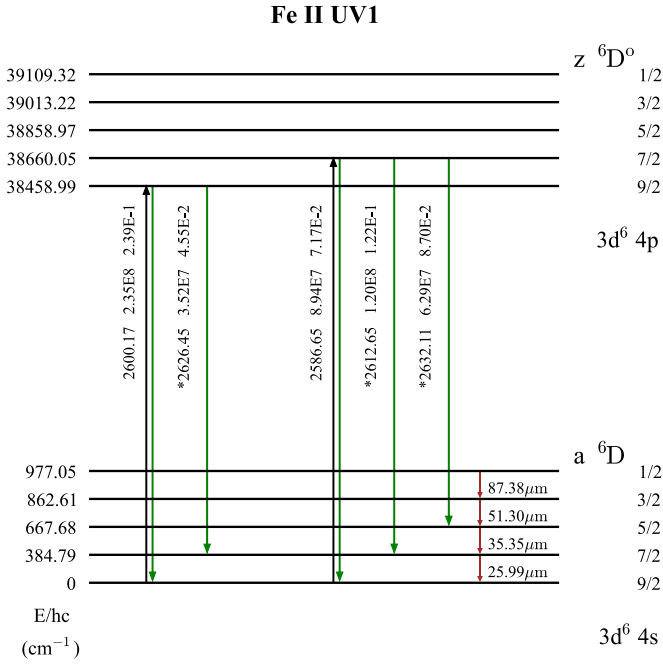


Figure 5. Energy-level diagram for the transitions in the first UV multiplet group (UV1) of Fe II, between the ground state and the first excited state. See Appendix A for a full description of the symbols and terms.

detailed description of the symbols and terms. Fe II $\lambda 2600$ is the transition between the lowest (ground) energy level (with $J = 9/2$) of the ground state and the lowest level (with $J = 9/2$) of the excited state. Because the second lowest energy level of the ground state has the total angular momentum number $J = 7/2$, the excited electron after the resonant absorption has a high probability, i.e., a high Einstein A coefficient, to spontaneously decay to this level, releasing a fluorescent photon at a slightly longer wavelength $\lambda = 2626.45$ Å. The pair Fe II $\lambda 2587$ and Fe II* $\lambda 2613$ also belong to UV1, though with the second energy level of the excited state as the higher anchor level.

The presence of these non-resonant emission lines implies that many of the resonant absorption lines above must be blended with resonant emission filling in, as for most transition groups with non-resonant channels, the decaying probability of the resonant channel is significant compared to the corresponding non-resonant channels. For example, the Einstein A coefficient for the resonant Fe II $\lambda 2600$ ($2.35 \times 10^8 \text{ s}^{-1}$) is over six times higher than that for the non-resonant Fe II* $\lambda 2626$ ($3.52 \times 10^7 \text{ s}^{-1}$), so an excited electron at $z \text{ } ^6\text{D}_{9/2}^0$ has a higher probability to decay to the lowest level ($a \text{ } ^6\text{D}_{9/2}$), instead of the second lowest level ($a \text{ } ^6\text{D}_{7/2}$), and release a Fe II $\lambda 2600$ photon, though if the Fe II optical depth is high, the emitted photon will be absorbed again. For those transition groups without any permitted non-resonant channels, the excited electron only decays through the resonant channel and the effect of emission infill will be greater. The exact amount of emission infill depends on the optical depth and transition probability of the relevant channels and the balance between absorption and emission in the multiple-scattering process. We discuss the emission infill and the relevant radiative transfer processes in detail in Section 4.

We find the velocity profiles of both absorption and emission lines to be asymmetric, skewed toward negative values, i.e., in

the blueshift direction, indicating a larger fraction of the gas sources that cause these features are flowing outward than inward. The profiles of the emission lines appear to be similar, while the degree of asymmetry of the absorption profiles varies from line to line. For example, compared to Fe II $\lambda 2587$ or Fe II $\lambda 2600$ as shown in the second panel in Figure 4, the Mg II $\lambda \lambda 2796, 2804$ lines are blueshifted from their rest-frame positions by a larger amount. Considering these species have similar ionization potentials (7.90 eV for neutral Fe and 7.64 eV for Mg) and likely co-exist spatially, the difference must be due to a larger amount of emission infill on top of the Mg II absorption.

For a better understanding of the absorption and emission in the composite spectrum of ELGs, we present a comparison with a composite spectrum of intervening quasar absorption-line systems in Section 3.4, and with a composite spectrum of local SF regions in Section 3.5. We will then investigate the physical processes with a gas flow model in Section 4.

3.4. Comparison with Intervening Absorbers

The composite spectrum of ELGs exhibits the absorption lines commonly seen in intervening quasar absorption-line systems. It is interesting to compare the so-called “down-the-barrel” spectra of ELGs with the intervening quasar absorber spectra. We select the absorbers from the JHU-SDSS metal absorber catalog (Zhu & Ménard 2013a), updated to the 12th Data Release (DR12, Alam et al. 2015).²⁰ We choose strong absorbers with Mg II $\lambda 2796$ rest equivalent width $W_0^{\lambda 2796} > 2$ Å, because there has been evidence showing that a large fraction of these strong absorbers is physically associated with the CGM of strong SF galaxies (e.g., Bergeron & Boissé 1991; Norman et al. 1996; Bouché et al. 2007; Nestor et al. 2011; Lan et al. 2014). For example, Bouché et al. (2007) detected strong H α emission around two-thirds of absorbers with $W_0^{\lambda 2796} > 2$ Å using near-infrared integral field spectroscopy. Lan et al. (2014) showed that the fraction of absorbers physically associated with SFGs, i.e., detected in the CGM around SFGs, increases with Mg II absorption strength.

In our differential analysis, we will focus on the line ratios, which is a less variable parameter than the absolute absorption strength. This is reasonable considering that (1) for different transitions of the same species, the line ratios are basically determined by quantum mechanics (oscillator strength), and (2) for lines of different species, the ratios are further determined by the abundance ratios, which are expected to be a weak function of the total abundance. For instance, if we have two sightlines, the first passes a single cloud with certain physical properties (such as volume density, temperature, metallicity, relative abundances of different elements), and the second passes through a gas cloud twice as large or a collection of two same-size gas clouds, which share the same physical properties as the cloud along the first sightline, the absolute absorption strength of the second sightline will be about twice that of the first, but the line ratios will be the same (barring saturation effect). In practice, changing the selection criterion, e.g., from $W_0^{\lambda 2796} > 2$ Å to > 3 Å or > 4 Å, does not change our conclusions, as the line ratios do not vary much for absorbers with strengths at $W_0^{\lambda 2796} > 2$ Å (e.g., Dey et al. 2015, and see also Appendix B). From the JHU-SDSS catalog, we select the 2310 absorbers with $W_0^{\lambda 2796} > 2$ Å at $0.6 < z < 1.2$, the same

²⁰ <http://www.pha.jhu.edu/~gz323/jhusdss>

redshift range as the ELGs and construct a median composite continuum-normalized spectrum. For more details regarding the quasar absorbers and how we estimate the continua of background quasars, we refer the reader to Zhu & Ménard (2013a).

We overplot the composite spectrum of quasar absorbers in red in Figures 3 and 4. Note the absorber spectra are based on luminous quasar spectra from SDSS I-III, so the S/N of their composite is orders-of-magnitude higher than the ELG composite. When constructing the composite spectrum, we shifted the absorber spectra to the rest-frame of the *absorbers*, so the absorption profiles are centered on their rest-frame positions. We find two major differences between the ELG composite and the quasar absorber composite:

1. There is no detectable non-resonant emission in the quasar absorber composite, even though its S/N is orders-of-magnitude higher.
2. The *ratios* of the absorption lines are different. For example, the peak absorption strength of Fe II $\lambda 2344$ is similar in both composites, while the peak strengths of Fe II $\lambda 2383$ and Mg II $\lambda \lambda 2796, 2804$ are much larger in the quasar absorber one. We present a more detailed quantification of the line ratios in Section 4.2.3.

In addition to the two main differences, we do not detect Ti II absorption lines in the ELG composite, which we suspect is due to the limited sample size and the low S/N.

In Section 4, we show that the line ratio difference is caused by the emission infill present in the ELG composite but absent in the quasar absorber composite.

3.5. Comparison with Local Star-forming Regions

Spectroscopic observations of SFGs, or astronomical sources in general, have been scarce in the NUV. Leitherer et al. (2011) compiled a UV spectroscopic atlas²¹ of *local* SF galaxies observed with the Faint Object Spectrograph (FOS) and the Goddard High Resolution Spectrograph (GHRS) on *HST*. The atlas includes small-(physical) aperture spectra of 15 regions of 9 SFGs with coverage between 2200 and 3200 Å, providing a rare opportunity for a direct comparison of the integrated NUV SEDs at different physical scales. From this compilation, we select nine spectra of six galaxies with relatively high S/N and strong absorption: NGC 1569, NGC 2403 (all 3 spectra), NGC 4569, NGC 5055, NGC 5253 (1 and 3), and NGC 5457 (NGC 5455). Note that the different spectra of one galaxy are independent from each other, originating from different SF regions in that galaxy. For details regarding their atlas, we refer the reader to Leitherer et al. (2011). With the selected nine spectra, we then construct the composite continuum-normalized spectrum following the same procedure as for the eBOSS ELGs. Before a careful comparison, we here emphasize several characteristics of the observations:

1. The aperture sizes of *HST* FOS/GHRS are one to a few arcseconds, and for all the nine spectra, correspond to physical sizes smaller than 40 pc (2–37 pc, see Table 6 in Leitherer et al. 2011). They are nearly three orders-of-magnitude smaller compared to the aperture size for the

eBOSS ELGs at $0.6 < z < 1.2$, which is about 15 kpc (for $2''$).²²

2. The wavelength calibration of the FOS/GHRS spectra is largely based on the absorption lines induced by the gas in the ISM in the Milky Way, which are often blended with the lines of the low-redshift extragalactic sources. We find that, based on the position of C III $\lambda 2298$, the composite spectrum is offset to longer wavelength by about 0.7 Å (about 91 km s⁻¹); we therefore correct the wavelength by -0.7 Å.
3. The spectral resolutions of FOS/GHRS are one to a few hundred km s⁻¹, a factor of 2–4 lower than that of the BOSS spectrographs.

The last two characteristics prevent us from making a quantitative comparison of the observed velocity profiles.

In Figure 6, we compare the ELG composite (in blue) with the composite spectrum of the nine local SF regions (in red) at $2200 \text{ Å} < \lambda < 2900 \text{ Å}$. We present a zoomed-in version in Appendix B. The two spectra share common absorption features across the wavelength range, including both the stellar photospheric absorption line C III $\lambda 2298$ and the absorption lines due to the ISM/CGM. We also observe some common weak absorption lines that must be intrinsic to the underlying stellar continuum. As discussed in Section 3.3, we do not identify these weak lines yet since they are still poorly understood. We find the following main differences.

1. There is no detectable line emission, either the nebular lines (C II], [O II]) or the non-resonant lines (Fe II*), in the composite of local SF regions.
2. The *ratios* of the absorption lines are different. For instance, the strength of Mg II $\lambda \lambda 2796, 2804$ is similar in both composites, while Fe II $\lambda 2374$, Fe II $\lambda 2587$ and Fe II $\lambda 2600$ are about 50% or more weaker in the composite of local SF regions. We present a more detailed quantification in Section 4.2.3.

We note that in the composite of local SF regions the ratios of the lines are similar to those in the quasar absorber composite (see Figure 27 in Appendix B).

The reasons for the non-detection of different emission lines are likely different. The [O II] doublet at 2471 Å, mostly associated with H II regions, is very weak compared to its lower energy counterpart [O II] $\lambda \lambda 3727, 3730$ and may be buried in the noise. The C II] emission, which is strong in the ELG spectra, is more extended than H II regions (as observed through the fine-structure emission [C II] $\lambda 157.7 \mu\text{m}$, e.g., Pineda et al. 2013) because of the lower ionization potential of neutral carbon, and the small (physical) apertures of FOS/GHRS did not capture enough C II] photons. The non-resonant Fe II* lines are not detected also because the emission is extended, though the emission mechanism is different from C II].

As in the comparison with quasar absorbers, the difference in absorption line ratios must be due to the resonant emission infill in the ELG spectra, which is stronger for some lines than the others. For example, the Mg II $\lambda \lambda 2796, 2804$ lines do not have a corresponding resonant channel, so all the fluorescent emission is through the resonant channel, causing a large amount of emission infill. We expect that, without emission infill, the intrinsic Mg II absorption strength in the ELG spectra would be much stronger than in the local SF region spectra, even though the observed strengths are similar in the two

²¹ <http://www.stsci.edu/science/starburst/templ.html>

²² We note that the average seeing at the SDSS telescope is about $1''.5$.

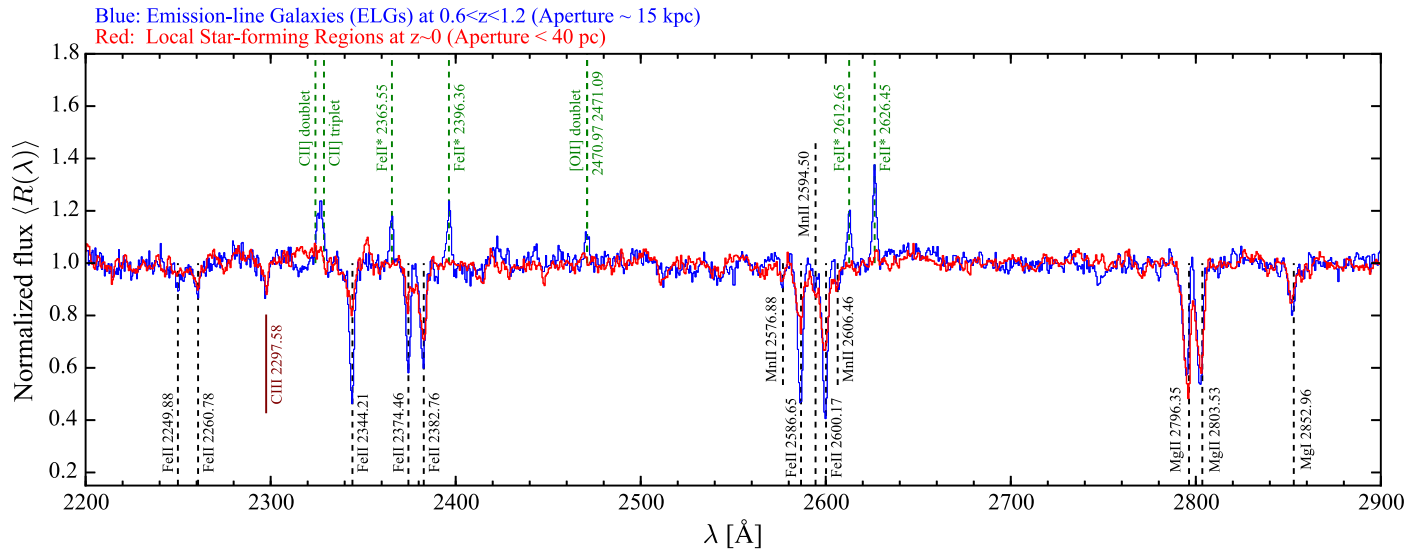


Figure 6. Composite continuum-normalized spectrum of ELGs (blue); the same as in Figure 3 but compared with the composite spectrum of local star-forming regions (red) from Leitherer et al. (2011).

sources. While for Fe II $\lambda 2374$, because the corresponding non-resonant channel has a high Einstein A coefficient, most of the fluorescent emission is through the non-resonant channel, resulting in little resonant emission infill, and the observed strength reflects the intrinsic absolute absorption strength. Under these considerations, the intrinsic absorption strength in the ELG spectra, either of the Fe II $\lambda 2374$ line as observed or of the Mg II doublet after the emission infill is corrected, is much stronger than in the spectra of the local SF regions, and this intrinsic difference indicates that the gas abundance, as manifested in column density and thus absorption strength, is much higher in the eBOSS ELGs than in those local SF regions observed by *HST*. We present a more detailed discussion below in the context of a gas outflow model. As we have limited data from *HST*, we will focus on the line ratios but not the absolute strength, in order to address the effects of emission infill and how to correctly interpret the observations.

4. INTERPRETATION

We have shown that the NUV composite spectrum of eBOSS ELGs display preferentially blueshifted absorption, induced by neutral and singly ionized species, Mg I, Mg II, and Fe II. In addition, we detected non-resonant Fe II* emission lines, which also exhibit a preferentially blueshifted profile and are not detected in either quasar absorber spectra or small-aperture spectra of local SF regions. These observed properties indicate that the gas causing the absorption and emission is predominantly flowing outward, and the outflows must be driven by the strong SF activities in the ELGs and extend to large galactic scales.

Galactic-scale outflows driven by star formation have been observed for over half a century, such as from the starburst galaxy M82 (e.g., Lynds & Sandage 1963; Bland & Tully 1988). The physics of galactic winds has been extensively studied (e.g., Heckman et al. 1990, 2000), though it is not yet conclusive due to the complexity of the baryon processes involved. For our purposes, we circumvent some of the complex processes, such as the origins and properties of the wind and gas, and instead we introduce a phenomenological

gas outflow model and interpret our data with an observation-driven approach in the context of the model.

4.1. A Spherical Gas Outflow Model

We describe the model in three steps. First, we present the key geometrical and physical characteristics of the model. Second, we consider the properties of the observations of the integrated spectra along the line of sight. Finally, we discuss quantitatively the radiative transfer processes and the model predictions for the SFG observations.

4.1.1. Basics of the Gas Outflow Model

Because of the statistical fashion of our composite analysis, we construct our model for the average of an ensemble of galaxies, not for a single source. We illustrate the model in Figure 7²³ and first emphasize the following two key characteristics.

1. **Spherical symmetry**—A basic outflow model for an individual galaxy includes a density profile $n(\mathbf{r})$ (in number) and a velocity profile $v(\mathbf{r})$, both as a function of the vector position \mathbf{r} . Observations have shown that the large-scale outflows driven by star formation are often bipolar, in the form of an expanding envelope (e.g., Heckman et al. 1990). In our composite analysis, we are averaging over all orientations randomly distributed and it is reasonable to assume spherically symmetric profiles $n(r)$ and $v(r)$.
2. **Velocity distribution**—Also due to the statistical nature of our approach, at a given galactocentric distance, there is a distribution of velocities. If gas accretion takes place

²³ The image in the center is a composite image of the central region of M82 with different orientations. The original image is from <http://hubblesite.org/gallery/album/galaxy/pr2006014a/>, courtesy of NASA, ESA, and The Hubble Heritage Team (STScI/AURA).

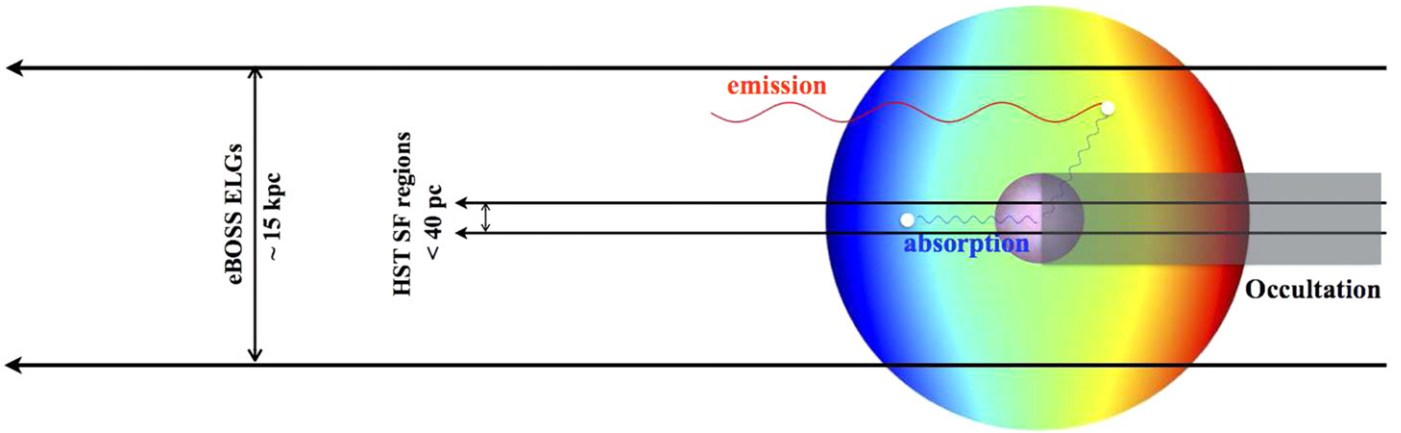


Figure 7. Spherical outflow model. The color scale indicates the mean line of sight velocity of emission/absorption at a given position, assuming velocity $v(r) \propto r^\alpha$, where $\alpha = 2$ is arbitrarily chosen. Resonant absorption takes place in front of the background light source (stars). Fluorescent photons, resonant or non-resonant, are scattered isotropically and only those scattered into the line of sight can be captured. The aperture size of the eBOSS fibers is $2''$, corresponding to about 15 kpc at $0.6 < z < 1.2$. The aperture sizes of *HST* FOS/GHRS are one to a few arcseconds, corresponding to less than 40 pc for the local star-forming regions observed. See Scarlata & Panagia (2015) for a similar model.

around the ELGs and if the infalling gas is enriched with the species we are interested in, it will also induce absorption and contribute to the statistical signatures. At small scales, the gas in the ISM also contributes to the absorption, and its motions, ordered or disordered, also affect the observed velocity distribution.

A statistical gas flow model therefore includes an average density profile, $n(r)$, an average velocity profile, $v(r)$, and a velocity dispersion profile, $\sigma(r)$. We expect the direction of the average velocity $v(r)$ to be outward, as we expect there is more gas flowing outward than inward. The velocity dispersion then accounts for the contributions at different velocities from outflows, inflows, and motions of the ISM at small scales. In addition, in observation, we need to consider the finite instrumental resolution and redshift precision, which can be effectively included in the velocity dispersion through convolution. For the eBOSS ELGs, the mean spectral resolution is about $\mathcal{R} \sim 2000$ ($60\text{--}70 \text{ km s}^{-1}$) and the mean redshift precision is about 20 km s^{-1} at redshift $z \sim 0.8$.

Our model is in principle similar to the one introduced by Scarlata & Panagia (2015, see also Rubin et al. 2011; Prochaska et al. 2011), which the authors used as the basis in their radiative transfer simulations to interpret space-based observations in the FUV, though here we emphasize the statistical aspect of our model. Considering the sample size and S/N of our current data, we cannot yet place strong constraints on the model details, such as the functional form of the profiles or the parameters. In Figure 7, for illustration purposes, we assume a power law for the average velocity profile $v(r) \approx r^\alpha$ with $\alpha = 2$, which is arbitrarily chosen. We leave the full modeling to future work, and focus on the general properties of the model predictions below.

4.1.2. General Model Predictions

Based on the model, we can predict the following general properties of the absorption and emission features in the integrated spectra along the line of sight.

- i. Origins and aperture dependence—In the model, the observed absorption and emission have different origins.

The absorption is induced by gas *in front of* the background light source, e.g., the stellar populations inside the galaxy. The re-emitted (fluorescent) photons, resonant or non-resonant, are scattered isotropically, so the observed emission originates from gas located everywhere within the aperture, except from behind the galaxy due to occultation (see below). The strength of the emission therefore increases with the aperture size until the aperture encloses all the absorbing gas, while the strength of absorption depends little on the aperture size unless the column density varies significantly across the galaxy.

- ii. Net effect—The sum of absorption and emission in a given set of transitions, including all the resonant and non-resonant channels, would be zero if and only if the observer could collect all the re-emitted photons scattered into the line of sight with a very large aperture. However, because of the finite size of a galaxy, the photons behind the galaxy cannot penetrate the high-density regions of the galaxy to be captured. As Scarlata & Panagia (2015), we refer to this effect as occultation. The finite size of galaxies makes the outflow model more complicated than that for stellar winds in which the star can be considered as a point source. The net effect of absorption and emission is therefore *always* absorption. At redshift $z \sim 0.8$, the typical effective *radius* of SFGs with $M_* \sim 10^{10} M_\odot$ is about 2–4 kpc (e.g., Williams et al. 2010; Wuyts et al. 2012).
- iii. Velocity profiles—If outflows are dominant (compared to inflows), the observed emission profile is asymmetric and preferentially blueshifted due to occultation of the redshifted emission behind the galaxy. The profile of the absorption (even without emission infill) is also blueshifted, since it is only induced by the gas in front of the galaxy’s stellar populations (the light source). We expect the degree of blueshift to be smaller for the emission profiles than absorption, because the re-emitted photons are scattered isotropically and only a negligible fraction of photons originating from the observed absorption are scattered into the line of sight, while other re-emitted photons within the aperture are less blueshifted.

iv-1. Emission infill—Like emission via the non-resonant channels, the model also predicts re-emitted photons via the resonant channels, producing emission filling in on top of the absorption. The emission infill is not sufficient to compensate for all the absorption so an observer always sees absorption (see point ii). However, because the emission profile is less blueshifted than absorption (point iii), the *observed* absorption profile is more blueshifted than the “*true*” absorption profile before emission infill. If the emission and absorption profiles are significantly different, e.g., due to large outflow velocities or large aperture (relative to the occultation), we also expect to see P-cygni-like profiles. The amount of emission infill depends on the aperture size, the galaxy (occultation) size, the permitted channels and their transition probabilities, and the optical depth, which determines whether the observed emission originates from a single or multiple scattering process and also the relative strength of different channels. The degree of emission infill (relative to the absorption) is therefore different from line to line. Below we discuss this quantitatively for the lines in the NUV.

4.1.3. General Radiative Transfer Processes

In an expanding envelope, if the velocity gradient is large, the radiative transfer processes can be treated under the Sobolev approximation (Sobolev 1960; Castor 1970; Rybicki & Hummer 1978). Scarlata & Panagia (2015, see also Prochaska et al. 2011) included an excellent discussion of the general radiative transfer processes involved in a galactic outflow, and Prochaska et al. (2011) also pioneered theoretical considerations of the NUV transitions. We refer the reader to those papers for more details. We here present a summary of the formulae most relevant to our analysis.

1. Absorption: in the Sobolev approximation, at a given position, the optical depth is given by

$$\tau(r) = \frac{\pi e^2}{m_e c} f_{lu} \lambda_{lu} n_l(r) \left| \frac{dv(r)}{dr} \right|^{-1}, \quad (5)$$

which is proportional to the density $n_l(r)$ at the lower level, the rest-frame wavelength of the transition $\lambda_{lu} = \lambda_{ul}$, oscillator strength f_{lu} , and the inverse of the velocity gradient (i.e., the thickness of the thin shell with the same velocity). We have ignored stimulated emission and angular dependence. Along the line of sight, the optical depth above applies to the velocity $v(r)$, or equivalently, the wavelength $\lambda_r = \lambda_{lu}[1 - v(r)/c]$, at which the absorption is given by $R_r = e^{-\tau(r)}$.

2. Emission: in a single-scattering event, after the absorption of a photon, the probability that the excited electron can decay from the upper level (u) to a given lower level (l) is given by

$$p_{ul} = \frac{A_{ul}}{\sum_i A_{ui}}, \quad (6)$$

where A_{ui} is the spontaneous emission coefficient from

the upper level u to the lower level i , and the summation is over all the possible channels in the lower state. The above equation ignores stimulated emission, collisional (de-)excitation, and also fine-structure emission within the same state.

If the electron decays to the original level, in our case, the lowest level in the lower state, the re-emitted photon can be absorbed again, resulting in a multiple-scattering process. The escape probability of a resonant photon from a shell of optical depth $\tau(v)$ is given by

$$\beta_{\text{esc}} = \frac{1 - e^{-\tau}}{\tau} \quad (7)$$

(e.g., Mathis 1972), and the fraction of the absorbed photons that are eventually re-emitted via a non-resonant (nr) channel to a lower level l is

$$\begin{aligned} f_{\text{nr},l}(\tau) &= p_{\text{nr},l} \sum_{n=0}^{\infty} [p_r (1 - \beta_{\text{esc}})]^n \\ &= \frac{p_{\text{nr},l}}{1 - p_r (1 - \beta_{\text{esc}})}, \end{aligned} \quad (8)$$

where $p_{\text{nr},l}$ and p_r are the probabilities of decaying to the non-resonant lower level l and the resonant lowest level, respectively (Equation (6)), and we have omitted the upper level symbol u for simplicity. The fraction of the absorbed photons that are eventually re-emitted via the resonant channel and *escape* from the shell is

$$\begin{aligned} f_r(\tau) &= p_r \beta_{\text{esc}} \sum_{n=0}^{\infty} [p_r (1 - \beta_{\text{esc}})]^n \\ &= \frac{p_r \beta_{\text{esc}}}{1 - p_r (1 - \beta_{\text{esc}})}. \end{aligned} \quad (9)$$

When the optical depth of a given shell $\tau(v)$ is small and the escape probability $\beta_{\text{esc}} \approx 1$, we reach the single-scattering approximation, i.e., Equation (6):

$$\begin{aligned} f_{\text{nr},l} &\approx p_{\text{nr},l}, \text{ and} \\ f_r &\approx p_r. \end{aligned} \quad (10)$$

When the optical depth $\tau(v)$ is large and the escape probability $\beta_{\text{esc}} \approx 0$, all the re-emitted photons will be through the non-resonant channels, if there are any, with:

$$\begin{aligned} f_{\text{nr},l} &\approx \frac{p_{\text{nr},l}}{1 - p_r}, \text{ and} \\ f_r &\approx 0. \end{aligned} \quad (11)$$

Note that in both cases, summing over all channels gives

$$\sum_{\text{nr},i} f_{\text{nr},i} + f_r = 1. \quad (12)$$

4.1.4. Radiative Transfer Processes in the NUV

With the formalism above, we now investigate quantitatively the absorption and emission lines in the NUV and their correlations in the context of the outflow model. We focus on eight resonant absorption lines, among which four have non-resonant channels:

1. Fe II $\lambda 2600$ with Fe II* $\lambda 2626$ (UV1),
2. Fe II $\lambda 2587$ with Fe II* $\lambda 2613$ and $\lambda 2632$ (UV1),
3. Fe II $\lambda 2374$ with Fe II* $\lambda 2396$ (UV2),
4. Fe II $\lambda 2344$ with Fe II* $\lambda 2366$ and $\lambda 2381$ (UV3),

and the other four do not:

1. Mg I $\lambda 2853$, Mg II $\lambda 2804$, Mg II $\lambda 2796$, and Fe II $\lambda 2383$ (UV2).

We do not consider Fe II $\lambda 2261$ (UV4), Fe II $\lambda 2250$ (UV5), and Mn II $\lambda \lambda 2577, 2594, 2606$ here because of their lower S/N in the data.

We present the relevant atomic data in Appendix A. We note that we do not detect Fe II* $\lambda 2632$ from UV1, whose Einstein A coefficient is about half that of Fe II* $\lambda 2613$, and Fe II* $\lambda 2381$ from UV3 has an Einstein A coefficient about half that of Fe II* $\lambda 2366$ and is blended with Fe II $\lambda 2383$ from UV2.

Within the context of the outflow model, we can now estimate the degree of the emission infill effect, i.e., the ratio of emission to absorption in the observed spectra, for the eight absorption lines in the NUV.

- iv-2. Degree of emission infill—The effect of emission infill depends on two main factors. For those with non-resonant channels, it depends on the fraction of resonant emission (f_r). In the single-scattering approximation, we have $f_r \approx p_r$ (Equations (6) and (10)) and with the atomic data from Appendix A, we have

$$p_{\text{Fe II}}^{\lambda 2374} < p_{\text{Fe II}}^{\lambda 2587} < p_{\text{Fe II}}^{\lambda 2344} < p_{\text{Fe II}}^{\lambda 2600} < p_{\text{no nr}} = 1, \quad (13)$$

where $p_{\text{no nr}}$ is the probability for lines without permitted non-resonant channels, which is one since the resonant channel is the only allowed transition path. When multiple-scattering events are considered (Equation (9)), this order does not change though the relative difference is smaller. We expect the effect of the emission infill to follow the same order.

When there is no non-resonant channel, it mainly depends on the degree of saturation—the more saturated the absorption line is, the larger an effect the emission infill has on the observation. Note the observed emission and absorption have different origins (point i). Based upon the elemental abundance (Asplund et al. 2009) and oscillator strength (Appendix A), the degree of saturation should be in the order of absorption strength as

$$W_{\text{Mg I}}^{\lambda 2853} < W_{\text{Fe II}}^{\lambda 2383} < W_{\text{Mg I}}^{\lambda 2804} < W_{\text{Mg I}}^{\lambda 2796}. \quad (14)$$

Finally, we expect the degree of emission infill, manifested by the degree of blueshift (due to the difference in the profiles of emission and absorption (point iii)) and the change in the observed absorption strength, to follow the same order given by Equations (13) and (14).

For a direct comparison of observations with the model predictions, it is necessary to understand what the true absorption profiles (before the emission infill) are. In the next Section 4.2, we introduce an observation-driven method to reveal the true absorption profiles.

4.2. Revealing the True Absorption Profiles

To reveal the true absorption profiles, we make two assumptions:

1. All the emission lines share the same normalized velocity profile.
2. All the absorption lines share the same true normalized velocity profile, i.e., prior to the emission infill.

In both cases, the lines are normalized to have the same amplitude. We make these assumptions based on that (1) the ionization potentials for neutral Fe and Mg (from I to II) are about the same, 7.90 eV and 7.64 eV, respectively (Table 1 in Appendix A), so singly ionized Fe⁺ and Mg⁺ exist in very similar physical conditions²⁴; (2) different elements (e.g., Fe and Mg) must be well-mixed at moderate redshift after a few billion years of galaxy evolution; and (3) based on limited high S/N high-resolution spectroscopic observations of quasar absorbers, Fe II and Mg II (as well as Mg I when detected) in quasar absorbers (induced by gas in the CGM) usually share similar velocity profiles (e.g., Churchill et al. 2000, see their Figure 5), and we consider it reasonable to extrapolate these results to the absorption lines in galaxy spectra. Finally, because we work on the observed profile, i.e., $R(\lambda) = e^{-\tau(\lambda)}$, but not the optical depth $\tau(\lambda)$, saturation plays an important role and we will treat the strongest Mg II lines separately in our method.

Under the assumptions, our observation-driven method consists of two steps.

1. We determine the common emission profile from the four non-resonant emission lines, which we call the unified profile and present in Section 4.2.1.
2. With the unified emission profile, we determine the unified true absorption profile with an iterative approach. We describe this process in detail in Section 4.2.2.

4.2.1. The Unified Emission Line Profile

We combine the four non-resonant emission lines, Fe II* $\lambda 2626$, $\lambda 2613$, $\lambda 2396$, and $\lambda 2366$, to determine the unified profile, as shown in Figure 8. The top panel presents the observed velocity profiles, shown in the rest frame of the galaxies. In the middle panel, we normalize all the lines to have the same amplitude, and in the bottom panel, we present the mean normalized profile as the estimate of the unified emission profile. We also plot the 1σ uncertainties determined from bootstrapping. We note that, because the far blue side of Fe II* $\lambda 2613$ at $v \lesssim -600 \text{ km s}^{-1}$ overlaps with the red side of Mn II $\lambda 2606$, to avoid the contamination, we do not include the blue side of Fe II* $\lambda 2613$ at $v < 0 \text{ km s}^{-1}$ while calculating the mean profile.

The unified emission profile appears to be asymmetric. We investigate its asymmetry further in Figure 9. In the upper panel, on top of the unified profile, we overlay a symmetric profile assuming the blue side mirrors the red side. We subtract the symmetric profile from the original one and show the result in the lower panel. The unified non-resonant Fe II* emission exhibits an excess on the blue side, with a confidence level higher than 2σ when integrated over $-500 \text{ km s}^{-1} < v < 0 \text{ km s}^{-1}$, indicating that a larger fraction of emission is blueshifted than redshifted.

²⁴ Neutral magnesium must be distributed in cooler environments. As we only have one Mg I line, we treat it the same way as Fe II and Mg II lines in current analysis.

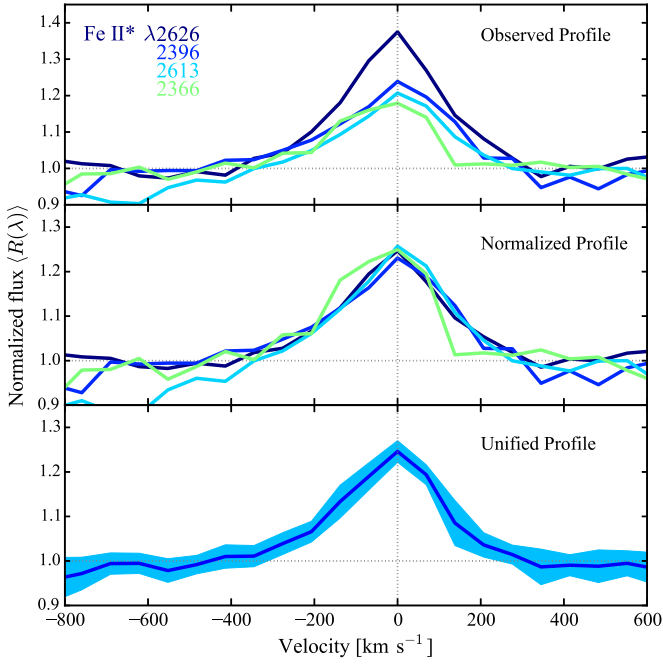


Figure 8. Velocity profiles of the non-resonant emission lines, shown in the rest frame of the galaxies. Top panel: the observed profiles. Middle panel: the observed profiles normalized to the same amplitude. Bottom panel: the mean unified emission profile. The shaded region indicates the 1σ uncertainties determined by bootstrapping.

4.2.2. The Unified Absorption Line Profile

With the unified emission line profile, we determine the emission infill and the unified true absorption line profile simultaneously with an iterative approach.

To proceed, we first investigate the observed velocity profiles in more detail. In Figure 10, we present the observed profiles of the eight absorption lines in the rest frame of the galaxies, normalized to have the same amplitude integrated over $-700 \text{ km s}^{-1} < v < 300 \text{ km s}^{-1}$. We have ordered the lines according to Equations (13) and (14), with bluer color indicating a larger predicted effect from emission infill. Figure 10 shows that: (1) the observed absorption profiles are different; (2) the degree of blueshift follows the order predicted by the model, and (3) the most blueshifted line, Mg II $\lambda 2796$, is about 200 km s^{-1} more blueshifted than the least blueshifted Fe II $\lambda 2374$.

Our iterative approach to determining the true absorption profile consists of the following steps.

1. We first use the normalized profile of Fe II $\lambda 2374$ as the initial guess of the unified true absorption profile, because the fluorescent emission after the Fe II $\lambda 2374$ absorption is dominated by the non-resonant channel Fe II* $\lambda 2396$ (Equation (13)).
2. With the unified absorption profile estimated from the previous step, we fit for the amount of emission that needs to be subtracted from the observed profile. More specifically, we express the observed profile $R_{\text{abs}}^{\text{obs}}(\lambda)$ by

$$R_{\text{abs}}^{\text{obs}}(\lambda) = R_{\text{abs}}^{\text{true}}(\lambda) + [R_{\text{emi}}(\lambda) - 1] \\ = \left\{ 1 - a \left[1 - R_{\text{abs}}^{\text{uni}}(\lambda) \right] \right\} + b \left[R_{\text{emi}}^{\text{uni}}(\lambda) - 1 \right], \quad (15)$$

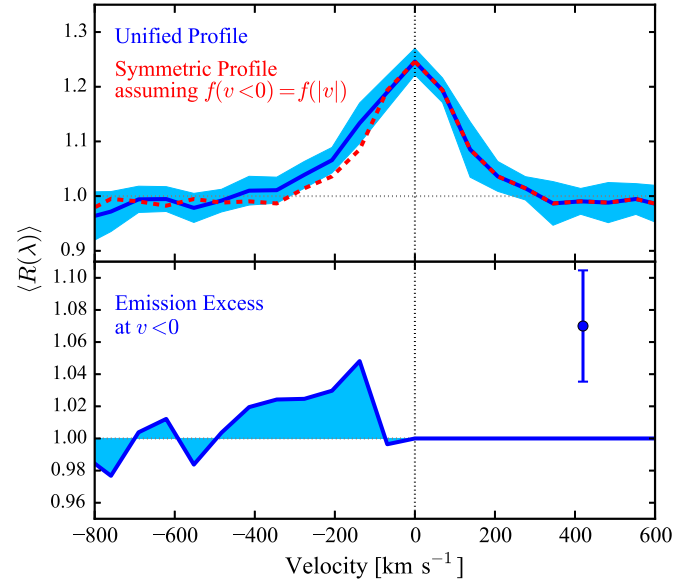


Figure 9. Asymmetry of the unified emission profile. Upper panel: the blue line and the shaded region show the mean unified emission profile and uncertainties as in the bottom panel of Figure 8. The red dashed line shows a symmetric profile assuming the blueshifted side mirrors the observed redshifted side. Lower panel: the emission excess on the blueshifted side. The error bar at the top right indicates the mean uncertainty at a given pixel (velocity).

where $R_{\text{abs}}^{\text{true}}(\lambda)$ and $R_{\text{emi}}(\lambda)$ are the unnormalized true absorption and emission profiles, respectively, and $R_{\text{abs}}^{\text{uni}}(\lambda)$ and $R_{\text{emi}}^{\text{uni}}(\lambda)$ are the unified normalized absorption profile from the previous step and the unified emission profile from Section 4.2.1, respectively. We perform a least-squares fit for the coefficients a and b .

3. We normalize the new absorption profiles $R_{\text{abs}}^{\text{true}}(\lambda)$ from the fitting in Step 2, calculate the mean as the new estimate of the unified absorption profile, and then repeat Step 2.

As discussed above, saturation requires special attention when it is severe. We set $R_{\text{abs}}^{\text{true}}$ at saturated pixels to be zero and do not include Mg II while estimating the unified profile in Step 3. We iterate the steps until the unified absorption profile and the coefficients a and b converge. In practice, we find that three iterations are sufficient to reach convergence.

We show the results in Figure 11. On the left, we show examples of the decomposition (Equation (15)), with the emission infill indicated by the green dashed lines. The emission-corrected absorption profiles, shown with the red lines, are deeper but less blueshifted than the observed ones (blue). On the right, in the top panel, we show the emission-corrected profiles of all the eight absorption lines, with color scales that are the same as in Figure 10. The middle panel shows the emission-corrected profiles normalized to the same amplitude, which we use to estimate the unified true absorption profile. We present the unified profile in the bottom panel, together with the uncertainties estimated via bootstrapping. Note that after emission-infill correction, the Mg II lines are heavily saturated at the line centers and are not used in the calculation of the mean profile.

The unified absorption profile is apparently asymmetric and preferentially blueshifted. With the emission-infill correction and the true absorption profiles estimated, we now investigate the details of the observed and emission-corrected profiles.

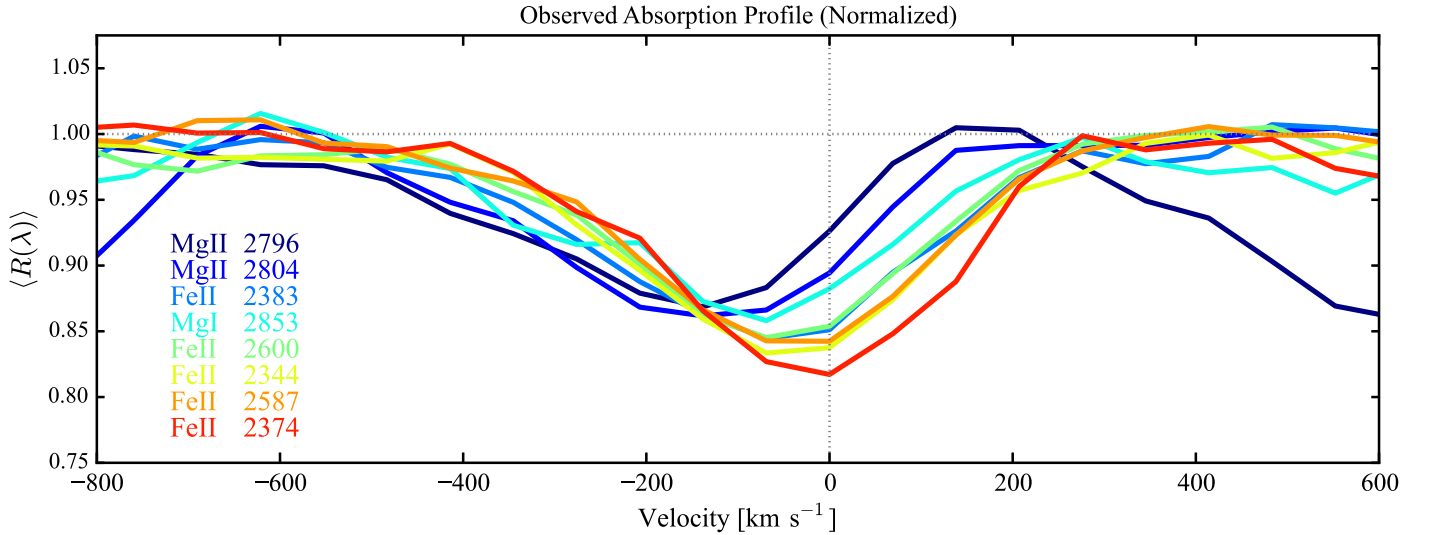


Figure 10. Observed velocity profiles of the absorption lines, presented in the rest frame of the galaxies and normalized to the same amplitude. The color scales indicate the order given by Equations (13) and (14).

4.2.3. Non-parametric Characterization of the True Absorption Profiles

To characterize the absorption profiles, we choose to use non-parametric variables, line ratios based on rest equivalent width (Equation (3)) and velocity offsets.

4.2.3.1. Line Ratios

Because of the different degrees of emission infill, the changes in the absorption strength vary from line to line. We compare line ratios before and after the emission-infill correction to study if the effect of emission infill follows the order of Equations (13) and (14).

We measure the rest equivalent width of the emission-corrected profiles by integrating over $-700 \text{ km s}^{-1} < v < 300 \text{ km s}^{-1}$. For the observed profiles of lines other than the Mg II doublet, we integrate over the same velocity range. We select the integration velocity range $-700 \text{ km s}^{-1} < v < 200 \text{ km s}^{-1}$ for the observed Mg II $\lambda 2796$ and $-600 \text{ km s}^{-1} < v < 300 \text{ km s}^{-1}$ for Mg II $\lambda 2804$ to avoid the contaminations from each other (see Figure 10).

To calculate line ratios, we select Fe II $\lambda 2374$ as the anchor, i.e., the common denominator, which has negligible emission infill. In Figure 12, we compare the line ratios before and after the emission-infill correction with the line ratios in the composite spectrum of strong quasar absorbers (QSOABSs, in the same redshift range) on the left and with those of local SF regions on the right. The variables plotted are the ratios of line ratios:

$$\left(\frac{W_{\lambda_i}}{W_{\lambda 2374}} \right)^{\text{ELG}} \bigg/ \left(\frac{W_{\lambda_i}}{W_{\lambda 2374}} \right)^{\text{QSOABS}} \quad \text{and} \quad \left(\frac{W_{\lambda_i}}{W_{\lambda 2374}} \right)^{\text{ELG}} \bigg/ \left(\frac{W_{\lambda_i}}{W_{\lambda 2374}} \right)^{\text{Local SF}}, \quad (16)$$

where λ_i represents the line names. In the figure, we have ordered the lines according to the predictions of Equations (13) and (14).

Figure 12 shows that the observed line ratios in the composite spectrum of ELGs differ from those of strong

quasar absorbers and also local SF regions, and the degree of the difference basically follows the predicted order. We find that the effect of emission infill (on line strength and thus ratio) can be larger than a factor of two, e.g., for Fe II $\lambda 2383$ and Mg II $\lambda \lambda 2796, 2804$. After the emission-infill correction, we find that the line ratios are consistent in the spectra of all the sources. We remind the reader here that we selected the quasar absorbers from the JHU-SDSS catalog with $W_0^{\lambda 2796} > 2 \text{ \AA}$. In Figure 27, we present the comparisons of line ratios with different selection criteria of quasar absorbers and show that our conclusion is basically not affected by the selections.

We stress that our method of estimating the emission infill is observation-driven, completely independent of any model. We only made the two assumptions about the unified emission and absorption profiles as elaborated at the beginning of this section. We also did not use any information about the strong quasar absorbers or the local SF regions. The agreement of the final line ratios is therefore not by construction, but rather the result of the method. As we expect that the gases inducing the absorption lines in different sources have similar origins, either supernova yields, stellar mass losses or other sources, and the line ratios in different source spectra should be in agreement, we consider our iterative fitting method successful in estimating the emission infill and determining the true absorption profiles.

4.2.3.2. Velocity Offsets

To characterize the velocity profile, we define a velocity offset variable v_{xx} to be the velocity where a fraction of xx percent of the absorption is at velocity $v > v_{xx}$.²⁵ In Figure 13, we show v_{80} , v_{50} , and v_{20} of the observed absorption profiles and of the unified profile. The order of lines is the same as in Figure 12, given by Equations (13) and (14).

Figure 13 (see also Figure 10) shows that, for the observed profiles, the velocity offsets of different lines are different, and the order follows the one predicted by the radiative transfer considerations in Equations (13) and (14) and the difference in the emission and absorption profiles (point iii in Section 4.1).

²⁵ We note that this is a characterization of the *total* absorption profile, including contributions from both outflows and ISM.

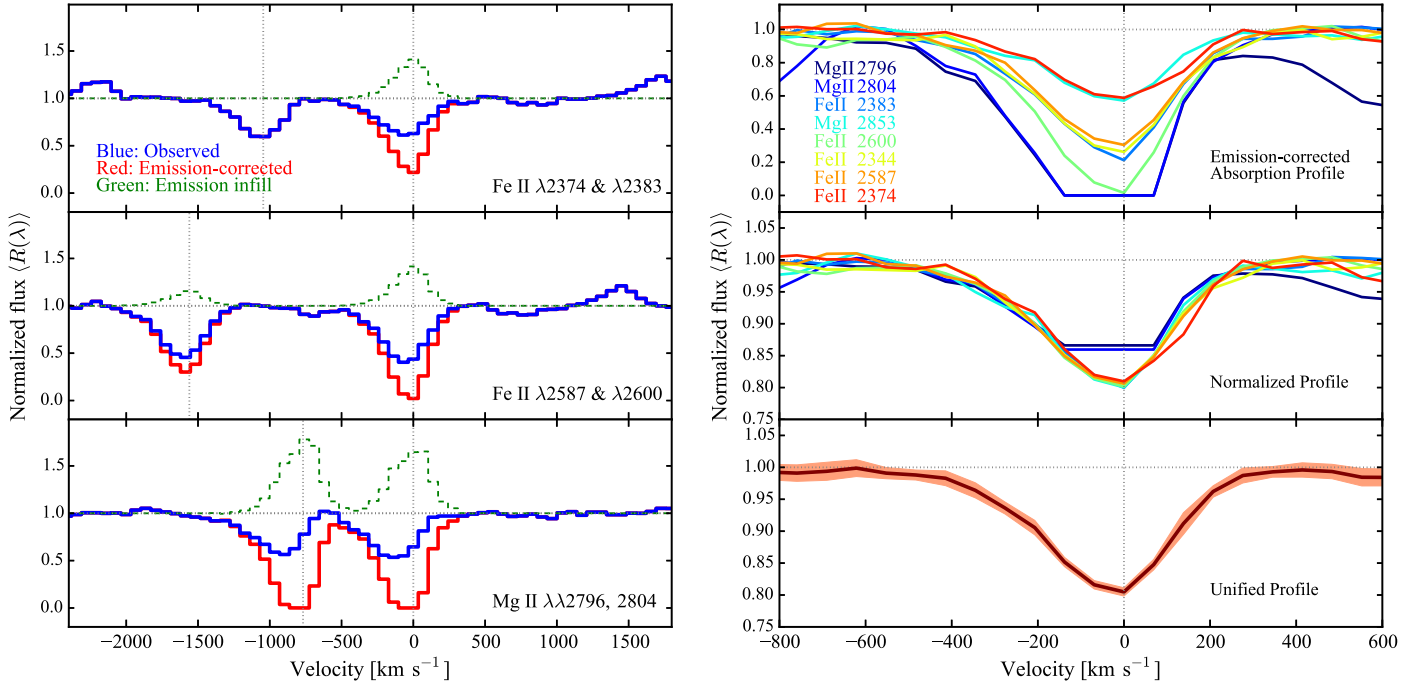


Figure 11. Left panels: examples of emission-infill correction. The blue lines show the observed absorption velocity profiles, red lines show the emission-corrected, and green lines show the subtracted emission. The vertical dotted lines mark the rest-frame positions of the lines and the zero velocity corresponds to the wavelength of the one with lower energy in each panel. Right panels: Top: the emission-corrected absorption velocity profiles. Middle: the emission-corrected profiles normalized to the same amplitude. Bottom: the unified emission-corrected absorption profile. The shaded areas indicate the 1 σ bootstrapping uncertainties. The color scales in the top two panels are the same as in Figure 10.

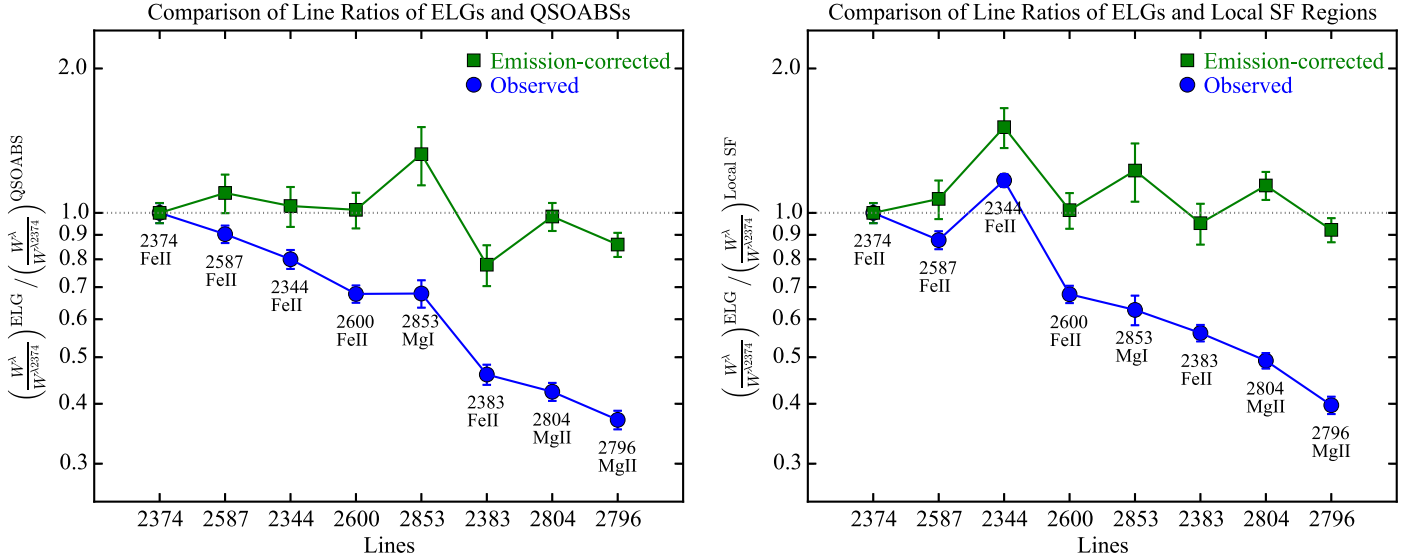


Figure 12. Comparison of line ratios of ELGs with strong quasar absorbers (QSOABSs, left) and local SF regions (right). The blue circles show the observed line ratios, and the green squares show the emission-corrected ones. We use Fe II $\lambda 2374$ as the anchor and order the lines according to Equations (13) and (14). The error bars indicate uncertainties in ELG line ratio measurements determined by bootstrapping, not including the uncertainties in the measurements of QSOABSs or local SF regions.

The unified emission-corrected profile is still asymmetric, but with a smaller degree of blueshift: the 50% velocity offset v_{50} is about -10 km s⁻¹, and $|v_{80}|$ is about 160 km s⁻¹, larger than $|v_{20}| \sim 110$ km s⁻¹. Our fitting result shows that without correcting for the emission infill, v_{80} , the 80% velocity offset, can be overestimated by over a factor of two for the lines most severely affected, e.g., Fe II $\lambda 2383$ and Mg II $\lambda\lambda 2796$, 2804.

4.3. Discussion

We now compare the observations, including the results of our emission-infill correction method, with the predictions of the spherical outflow model presented in Section 4.1. We go over the predictions point by point.

(i) Aperture dependence—The physical aperture size of the eBOSS ELG spectra is about 15 kpc, while that of the *HST*

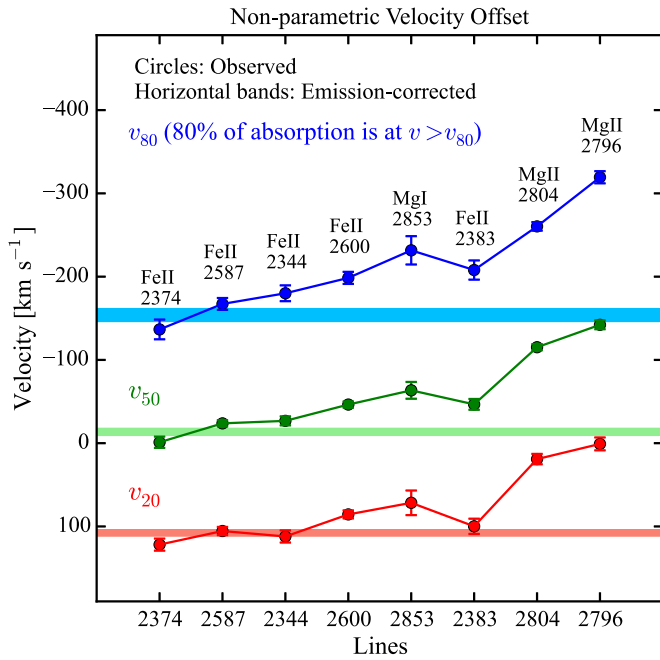


Figure 13. Non-parametric characterization of the absorption velocity profiles. We show v_{80} (blue), v_{50} (green) and v_{20} (red), before (circles) and after (horizontal bands) the emission-infill correction. The order of the lines is the same as in Figure 12. The widths of the horizontal bands indicate the uncertainties. All the uncertainties are determined by bootstrapping.

FOS/GHRS spectra of the local SF regions is smaller than 40 pc. In the spectra of the local SF regions, we do not detect the non-resonant emission that otherwise persist in the ELG ones. This agrees with the model and is because the *HST* FOS/GHRS aperture size is too small to capture the extended fluorescent emission.

We can also explain the absence of the non-resonant emission in the QSOABS spectra in the context of the model. The intervening quasar absorption-line systems are induced by gas clouds in the CGM, on average probably many tens of kpc away from the host galaxy, where the average gas density is small and consequently the surface brightness of fluorescent emission is low. Within the aperture of the quasar absorbers, which has roughly the same collecting area as that of the ELGs, only a negligible amount of fluorescent photons are emitted into the line of sight. If we had a ring-like aperture to collect all the photons in an annulus centered on the galaxy, we would be able to collect hundreds of times more photons and should be able to see some fluorescent emission.

(ii) Net effect—The net effect is always absorption due to occultation in the model, even if the aperture encloses all the emission scattered into the line of sight. In the data, when we sum up all the absorption and emission in a given set of channels, the net result is absorption.

(iii) Velocity profiles—The outflow model predicts that both the emission and (emission-infill corrected) absorption profiles are blueshifted, with the absorption more so than the emission. Figures 9 and 13 quantify the asymmetry and the blueshift of the profiles individually, though in different ways. To compare the two profiles directly, we show them together in Figure 14. For display purposes, we have flipped the absorption profile and also normalized them so that they roughly have the same peak value. The absorption profile is more blueshifted than the emission, as in the model.

As discussed in the basics of the model, the composite spectra include effects from not only the outflows, but also the inflows, the motions of the ISM in the galaxy, the instrumental resolution as well as the redshift precision. If the aperture is large and collects all the re-emitted photons along the line of sight, and if the outflowing gas is extended to a much larger scale than the galaxy, we expect the red side of the emission profiles to be broader than nebular lines, extended to further red. On the other hand, if a substantial fraction of the gas is falling in onto the galaxy at high velocities, we also expect the red side of both the emission and absorption profiles to be broader. In the lower panel of Figure 14, we show the [O III] $\lambda 5008$ profile of the NUV sample. We note that ELGs at $z \gtrsim 1$ do not have [O III] coverage, but they account for a small fraction (10%) of the sample. We find that the [O III] $\lambda 5008$ profile is well-represented by a Gaussian profile and the best-fit width (σ) is about 108 km s^{-1} . We overplot this Gaussian profile in both panels for comparison.

The mean spectral resolution of the BOSS spectrographs is about $60\text{--}70 \text{ km s}^{-1}$ and the average redshift precision of the eBOSS ELGs at redshift $0.6 < z < 1.2$ is about 20 km s^{-1} . The width of the nebular emission line profile (108 km s^{-1}) must therefore be dominated by the intrinsic rotation and disordered motion of the ISM along the line of sight, which account for about 85 km s^{-1} when we subtract the spectral resolution and redshift precision by quadrature. This is consistent with measurements of kinematic properties and the Tully–Fisher relation for bright galaxies at these redshifts (e.g., Vogt et al. 1996; Weiner et al. 2006; Miller et al. 2011).

We find that, on the red side, both the emission and absorption profiles are consistent with [O III] $\lambda 5008$ within the uncertainties. This suggests that, within the uncertainties of our data, we have not observed evidence for outflows on scales larger than the galaxy nor the evidence for inflows. The larger-scale outflows would extend the emission profile to higher velocities (farther on the red side), and the inflows would extend both the emission and absorption profile. However, the former (that we did not see evidence for larger-scale outflows) could be because the aperture size (15 kpc) is not sufficiently large, while the latter could be because the inflow velocities (e.g., $< 200 \text{ km s}^{-1}$, Rubin et al. 2012) are comparable to the ISM motions and the emission/absorption effects of the inflows and the ISM are blended together.

If we assume the emission-corrected absorption on the red side solely originates from the ISM, we can decompose the total absorption into a part due to the ISM with a symmetric profile and the other due to the outflows (e.g., Weiner et al. 2009).²⁶ Applying this decomposition method to the unified emission-corrected absorption profile, we obtain a blueshifted excess profile, more extended than the emission excess at $v < 0 \text{ km s}^{-1}$ as shown in Figure 9, with maximum velocity about -600 km s^{-1} . The ratio of the excess to the subtracted symmetric profile, which represents the ratio of the amount of outflowing gas to that of the ISM assuming the decomposition is ideal, is about 1:3. However, because there could be a broad distribution of outflow velocities, i.e., a large $\sigma(r)$ in the outflow model even without the ISM contribution, it is likely that the symmetric component also includes a large contribution from the outflowing and/or inflowing gas, in

²⁶ We note that Weiner et al. (2009) applied this method to the *observed* Mg II absorption, as they did not consider the emission infill.

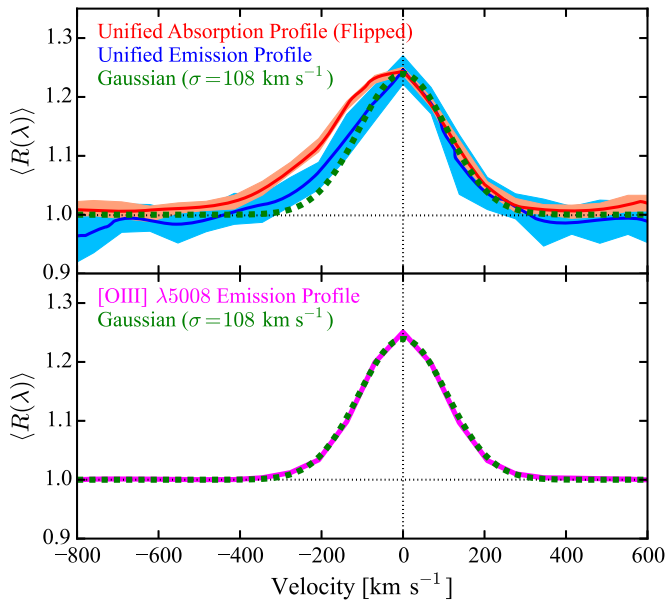


Figure 14. Upper panel: the comparison of the unified, emission-corrected absorption velocity profile (red), the unified emission profile (blue), and a Gaussian profile with the width of 108 km s^{-1} (green). For display purposes, we have flipped the absorption profile and also adjusted the profiles so that they have roughly the same peak value. The shaded regions show the 1σ bootstrapping uncertainties. Lower panel: the comparison of the normalized [O III] $\lambda 5008$ emission profile for ELGs (at $0.6 < z \lesssim 1.2$, magenta) with the same Gaussian profile (green) as in the upper panel. The uncertainties of the [O III] profile are about the same size as the line width.

which case the contribution from the ISM is much smaller than $3/4$.

(iv) (Degree of) Emission infill—The model predicts that, in large-aperture spectra, there is emission filling in on top of the resonant absorption, and because the emission profile is less blueshifted, the infill results in an observed absorption profile that is more blueshifted. The degree of the emission infill depends on the transition probabilities of the permitted channels and the degree of saturation for those without non-resonant channels. We have demonstrated that the data agree with these predictions in Figures 10–13. In particular, we show that the blueshifts, line ratios, and velocity offsets of the observed profiles follow the same order as predicted (Equations (13) and (14)). The observed v_{80} , the 80% velocity offset, can be overestimated by a factor of two compared to that in the emission-corrected profile. After the emission correction, the line ratios in the spectra of ELGs are consistent with those of strong quasar absorbers and local SF regions.

The different degrees of blueshift for different lines were also suggested by Prochaska et al. (2011) and were observed in the Keck spectra of SFGs by Erb et al. (2012) and Kornei et al. (2013) and in the VLT spectra by Tang et al. (2014). Erb et al. (2012, see also Kornei et al. 2013) also found a variety of Mg II profiles in their individual spectra, and suggested some emission might originate from H II regions. In our model, we have ignored such contributions. With our data, we cannot yet quantify the effect of the emission from H II regions on the line profiles in the composite analysis.

We do not observe P-cygni-like profiles in the composite spectrum of the full sample. This is likely because the difference of the emission and absorption profiles on the red side is not large (Figure 14) and the amount of emission infill is

not sufficient, since P-cygni-like profiles require a large amount of emission infill that is more extended on the red side. In the next section, when studying the [O II] $\lambda\lambda 3727, 3730$ dependence, we show that the Mg II absorption features P-cygni-like profiles for the subsample with the higher [O II] $\lambda\lambda 3727, 3730$ rest equivalent width.

In summary, we conclude that our statistical, spherical outflow model can simultaneously explain the multiple observed properties of emission and absorption features in the NUV.

5. CORRELATIONS WITH [O II] $\lambda\lambda 3727, 3730$

Observations have shown that outflow properties, such as the velocity, depend on galaxy properties (e.g., Rupke et al. 2005; Tremonti et al. 2007). From the eBOSS pilot observations, we can measure the [O II] $\lambda\lambda 3727, 3730$ properties of the ELGs. We here study the dependences of the emission and absorption lines in the NUV on the total rest equivalent width ($W_{[\text{O II}]}^{\lambda 3728}$) and luminosity ($L_{[\text{O II}]}^{\lambda 3728}$) of the [O II] doublet.

For each variable, we divide the NUV sample into two subsamples, split at the median values ($\langle W_{[\text{O II}]}^{\lambda 3728} \rangle = 51.4 \text{ \AA}$ and $\langle \log_{10} L_{[\text{O II}]}^{\lambda 3728} \rangle = 41.6 \text{ dex}$). We then perform the same analysis as for the full sample, including constructing the composite spectra, calculating the unified emission profiles, estimating the emission infill and determining the true absorption profiles. We present some of the details in Appendix C, including the distributions of $W_{[\text{O II}]}^{\lambda 3728}$ and $\log_{10} L_{[\text{O II}]}^{\lambda 3728}$ (Figure 28), the observed emission/absorption profiles (Figures 29 and 30), and the (unnormalized) emission-corrected absorption profiles (Figure 31). We here discuss in detail the emission strength, the observed absorption profiles of Mg II, the emission-corrected absorption strength, and the unified velocity profiles.

1. Emission strength—Figure 15 shows the dependences of the non-resonant emission strength on the [O II] $\lambda\lambda 3727, 3730$ rest equivalent width and luminosity. Note for comparison, we have added the data points measured from the full sample in solid symbols, which are correlated with the measurements based on the two subsamples. Within the range probed, we find that the emission strength (in rest equivalent width) scales almost linearly with $W_{[\text{O II}]}^{\lambda 3728}$. In the right panel, we show that the emission equivalent width also positively depends on the [O II] luminosity, but to a lesser degree.
2. Observed absorption profiles—In Figure 16, we present the observed Mg II profiles, which show the strongest dependence on [O II] among the absorption lines (Figure 30). The correlation appears to be stronger with the rest equivalent width than with the luminosity. This must be due to a stronger dependence of the emission infill on the rest equivalent width. The observed Mg II profile for the subsample with higher $W_{[\text{O II}]}^{\lambda 3728}$ has a P-cygni-like shape, indicating a large amount of emission infill.

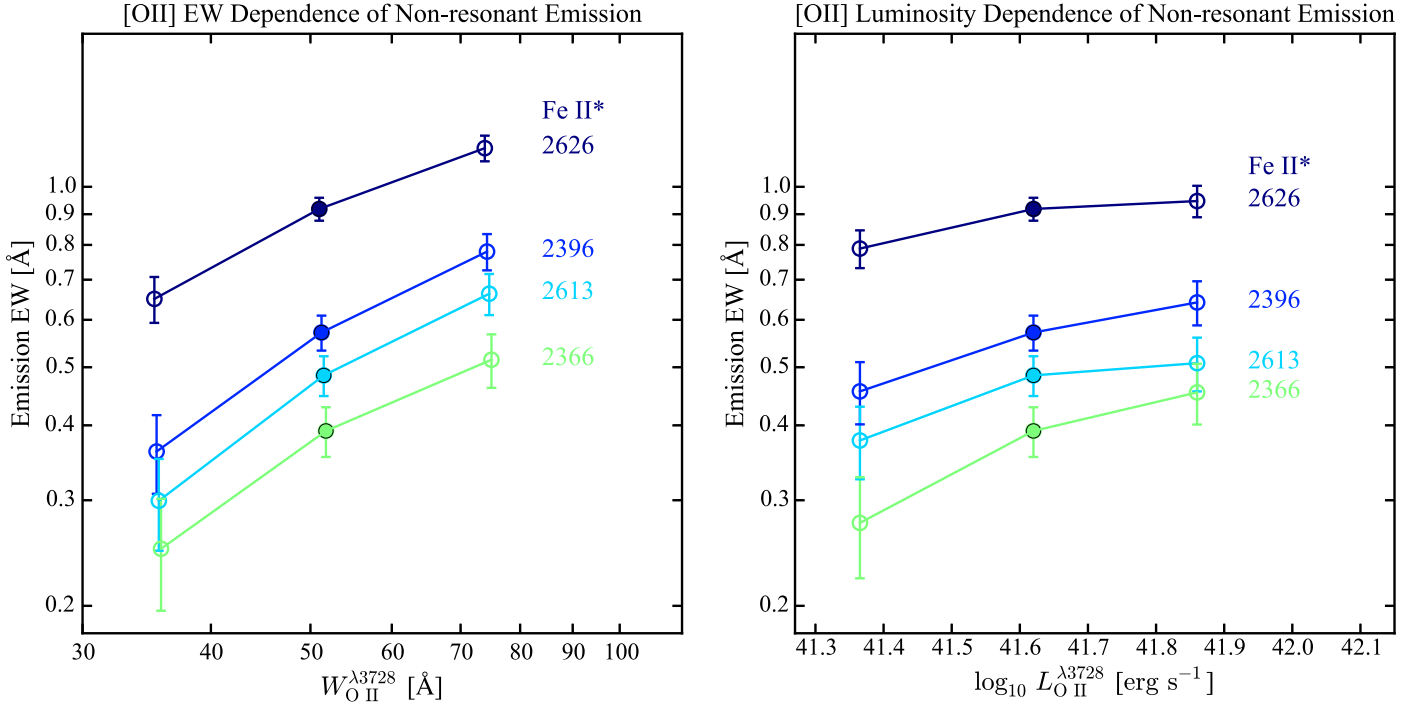


Figure 15. Dependences of the rest equivalent width of the non-resonant emission lines on the [O II] $\lambda\lambda 3727, 3730$ rest equivalent width (left) and luminosity (right). Note that both the x axes are in logarithmic scale.

3. Emission-corrected absorption strength—Figure 17 shows the dependences of the emission-corrected absorption rest equivalent width on the [O II] properties. Except for the saturated Mg II lines, other lines are positively correlated with both $W_{\text{O II}}^{\lambda 3728}$ and $L_{\text{O II}}^{\lambda 3728}$, with the dependence tentatively stronger for the former.

4. Unified velocity profiles—Figure 18 presents the unified emission and absorption profiles as a function of [O II] rest equivalent width and luminosity. Within the uncertainties, for both profiles, we do not find a dependence on either $W_{\text{O II}}^{\lambda 3728}$ or $L_{\text{O II}}^{\lambda 3728}$, although the P-cygni-like shape of the observed Mg II absorption for the subsample with higher $W_{\text{O II}}^{\lambda 3728}$ requires the emission profile to be more extended on the red side than the absorption, unlike for the main sample (Figure 14). In the future, larger samples will help pin down these dependences with high S/N.

Among all the correlations, we find that the strongest one is between the rest equivalent widths of non-resonant emission and [O II], which also results in the strong dependence of the observed absorption profiles, especially of the Mg II lines, on the [O II] rest equivalent width. To the first order, the [O II] luminosity is an indicator of SFR, while the [O II] rest equivalent width is an indicator of specific SFR. Our results suggest that the properties of the emission, and to a lesser degree, the absorption are stronger functions of specific SFR than of SFR. However, considering the uncertainties due to our

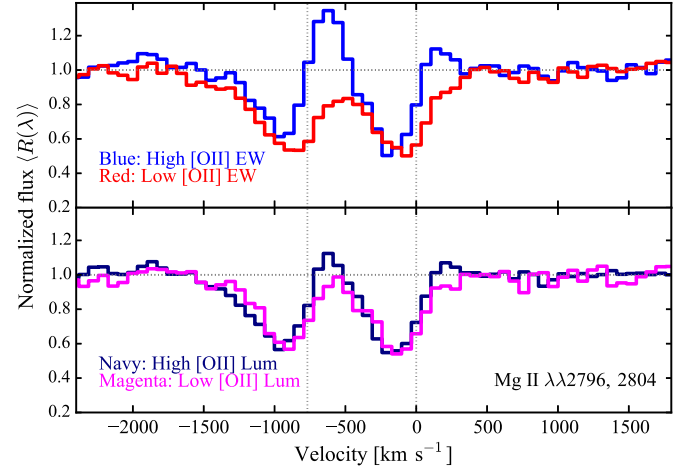


Figure 16. Dependences of the observed absorption velocity profiles of the Mg II lines on the [O II] $\lambda\lambda 3727, 3730$ rest equivalent width (upper panel) and luminosity (lower panel).

sample size, the exact correlations between the properties of the spectral features in the NUV and those of galaxies and their implications for galaxy evolution remain to be determined.

6. SUMMARY

The pilot observations of the ELG program in the eBOSS in SDSS-IV have obtained a sample of 8620 ELGs at $0.6 < z < 1.2$, providing a good opportunity for investigations of the rest-frame near-ultraviolet (NUV) part of the SEDs of SFGs. We constructed median composite continuum-normalized spectra to study the emission and absorption features in the NUV. Our main results are:

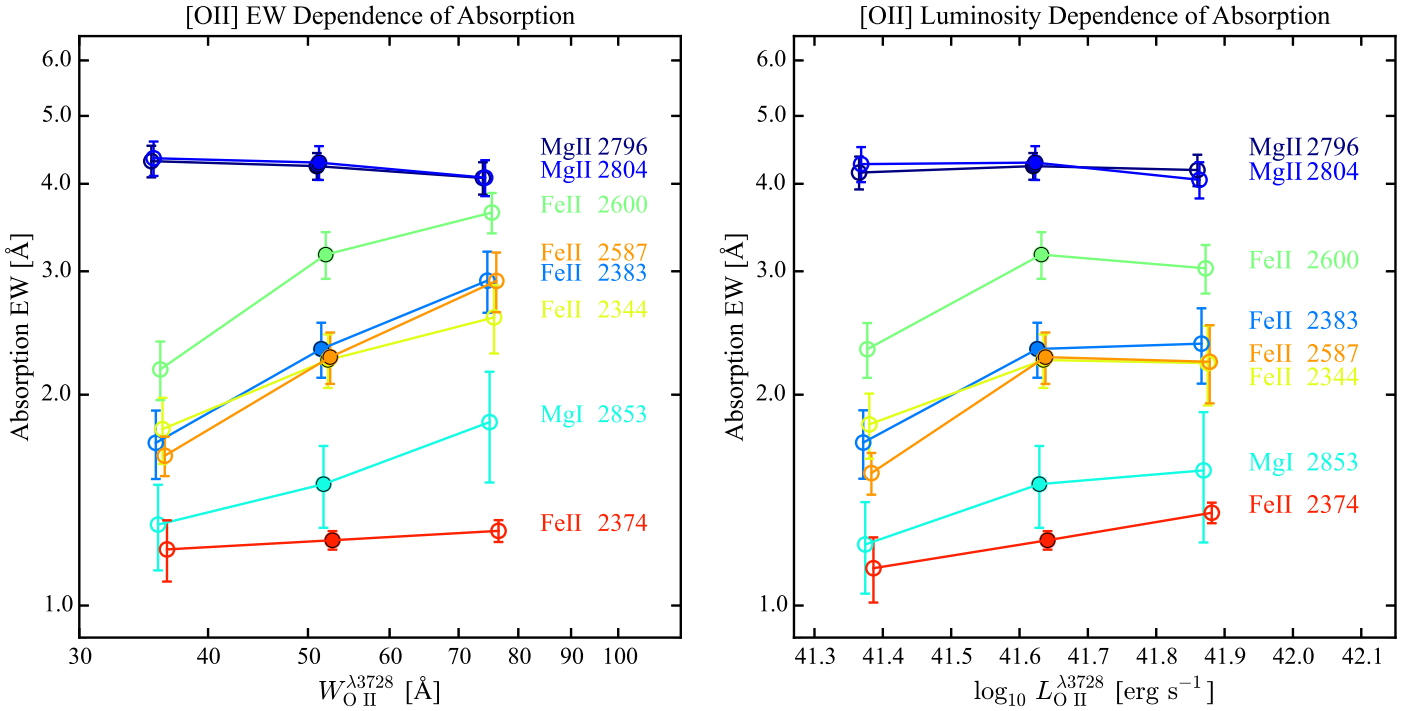


Figure 17. Dependences of the rest equivalent width of the emission-corrected absorption lines on the [O II] $\lambda\lambda 3727, 3730$ rest equivalent width (left) and luminosity (right). The color scales are the same as in Figure 10, based on the orders given by Equations (13) and (14).

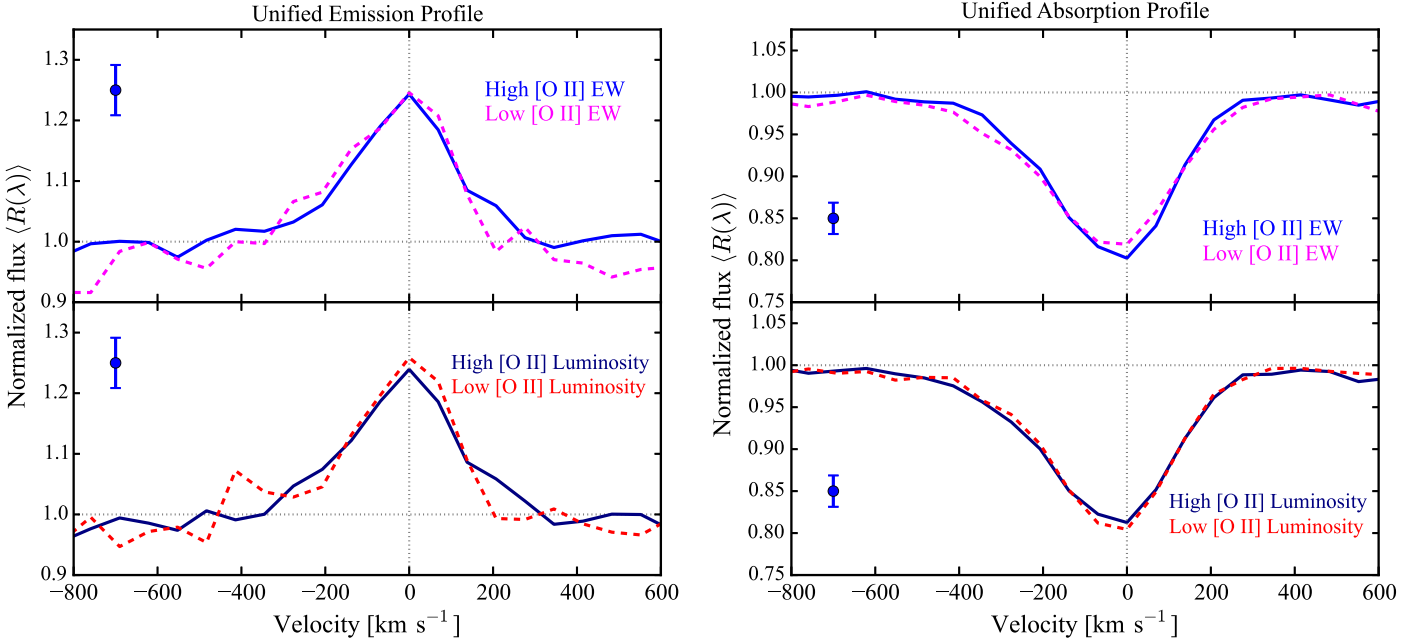


Figure 18. Dependences of the unified emission profile (left) and the unified emission-corrected absorption profile (right) on the [O II] $\lambda\lambda 3727, 3730$ rest equivalent width (upper panels) and luminosity (lower panels).

1. The median composite spectra of the ELGs feature non-resonant Fe II* emission and resonant absorption due to Mg I, Mg II and Fe II. Both the emission and absorption profiles are asymmetric, preferentially blueshifted, indicating ubiquitous outflows driven by star formation at $0.6 < z < 1.2$.
2. We found a variety of velocity profiles for the observed absorption lines with different degrees of blueshift.
3. Comparing the ELG spectra with those of strong intervening quasar absorption-line systems in the same redshift range, we found that they feature the same absorption lines but with different line ratios.
4. We compared the eBOSS ELG spectra with the NUV spectra of the local star-forming regions taken with the FOS and Goddard High-resolution Spectrograph (GHRS) on *HST*. The physical aperture size of the eBOSS ELG

spectra at $0.6 < z < 1.2$ is about 15 kpc, while the aperture size of the FOS/GHRS spectra of the local SF regions is less than 40 pc. We found the FOS/GHRS spectra also display the same (though weaker) absorption lines, but do not exhibit the non-resonant Fe II* emission. We also found different ratios for the resonant absorption lines.

5. We introduced a statistical, spherical outflow model, in which the observed non-resonant emission is the fluorescent (re-emitted) photons after the occurrence of absorption that are scattered into the line of sight. The model predicts that there is scattered resonant emission filling in on top of absorption, and the amount of emission infill depends on the transition probabilities of the allowed channels, resulting in the variety of the observed absorption profiles.
6. We developed an observation-driven, model-independent method to estimate the emission infill and reveal the true absorption profile. We showed that after the emission correction, the absorption line ratios in the ELG spectra are consistent with those in the spectra of strong quasar absorbers and local star-forming regions.
7. We demonstrated that the outflow model can simultaneously explain the multiple observed properties of the emission and absorption features in the NUV, including (i) the aperture dependence, (ii) the net effect, (iii) the emission velocity profiles and the emission infill-corrected absorption profiles, and (iv) the variety of the observed absorption profiles and the degree of emission infill.
8. Finally, we investigated the dependence of NUV features on the [O II] $\lambda\lambda 3727, 3730$ rest equivalent width and luminosity and found that the strongest correlation is between the non-resonant emission strength (in rest equivalent width) and the [O II] rest equivalent width.

Our results have profound implications for galaxy formation and evolution and for correct interpretations of observations. Recent observations of CGM have greatly advanced our understanding of gas outside galaxies, finding a large amount of hydrogen and metals in the CGM around both star-forming and quiescent galaxies to varying degrees (e.g., Steidel et al. 2010; Bordoloi et al. 2011, 2014; Tumlinson et al. 2011; Thom et al. 2012; Borthakur et al. 2013; Stocke et al. 2013; Zhu & Ménard 2013b; Peebles et al. 2014; Werk et al. 2014; Zhu et al. 2014). The origin of the gas in the CGM, especially metals, is now one of the most outstanding open questions. Suggestions include star formation-driven outflows (e.g., Chevalier & Clegg 1985) and AGN-driven outflows (Silk & Rees 1998), among others. The outflow mechanisms can not only expel gas out of galaxies, but can also result in a greatly reduced rate (quenching) in star formation, which is a necessary component in any modern galaxy formation theory in order to match the observed stellar mass function of galaxies and theoretical mass function of dark matter halos and explain the observed bimodality of star-forming and quiescent galaxies (e.g., Croton et al. 2006; Somerville et al. 2008). Our observations provided strong evidence for ubiquitous galactic-scale outflows driven by star formation as one of the most important gas sources, in agreement with previous works (e.g., Heckman et al. 1990, 2000, 2015; Steidel et al. 1996, 2010; Pettini et al. 2001; Shapley et al. 2003; Martin 2005; Rupke et al. 2005; Veilleux et al. 2005; Weiner et al. 2009, among others). The exact mechanisms driving the outflows are still a debated topic,

with propositions including ram pressure from hot outflowing gas from supernovae (e.g., Chevalier & Clegg 1985; Murray et al. 2005) and radiation pressure from massive star clusters (e.g., Nath & Silk 2009; Murray et al. 2011).

Our analysis also demonstrated that the NUV window is an informative region in the spectrum. The series of emission and absorption lines provides a new means to probe the gas physics. The model we introduced (see also Rubin et al. 2011; Prochaska et al. 2011; Scarlata & Panagia 2015) has many important implications, such as the dependences of non-resonant emission on the aperture, outflow, and galaxy (occultation) sizes, and points the future investigations of outflow physics toward new directions. For instance, it is of great interest to explore the surface brightness profile of the non-resonant emission, e.g., through narrow-band imaging or spatially resolved spectroscopy (e.g., Rubin et al. 2011; Martin et al. 2013), to further study the scale dependence of outflows. Moreover, our results demonstrated the importance of correcting the emission infill for accurate interpretations of absorption observations, as also suggested by some recent works (Rubin et al. 2011; Prochaska et al. 2011; Erb et al. 2012; Kornei et al. 2013; Tang et al. 2014).

Besides using the “down-the-barrel” spectra to probe the gas physics directly associated with the galaxies, we can also employ the cross-correlation techniques developed recently (e.g., Steidel et al. 2010; Zhu et al. 2014), using absorption information induced in background source spectra, to probe the CGM of foreground sources. Combining the two different types of observation will produce a more complete picture of the baryon processes in galaxy formation and evolution.

The sample size of the NUV spectroscopic data sets will grow by orders-of-magnitude in the next decade. At the conclusion of the ELG program, eBOSS will obtain spectra for about 200,000 ELGs at $z \gtrsim 0.6$, a sample over 20 times larger than the one used in this paper. DESI (Schlegel et al. 2011; Levi et al. 2013) and PFS (Takada et al. 2014) will obtain higher-resolution spectra with larger telescopes for about 20 million ELGs at higher redshift ($z > 1$), where more lines are redshifted into the optical. Based upon the details revealed in the composite spectra of less than 10,000 galaxies with the 2.5-m SDSS telescope, we expect that NUV spectroscopy will play an important role in future investigations of the properties and evolution of galaxies.

G.B.Z. started this work when he was visiting Princeton University in 2014 December and he would like to thank Michael Strauss and Jim Gunn for their hospitality. He also thanks Bruce Draine, Tim Heckman, Claus Leitherer, Jason X. Prochaska, and Rosie Wise for useful discussions. G.B.Z. acknowledges support provided by NASA through Hubble Fellowship grant #HST-HF2-51351 awarded by the Space Telescope Science Institute, which is operated by the Association of Universities for Research in Astronomy, Inc., under contract NAS 5-26555. We thank an anonymous referee for helpful comments that have helped improve the paper.

J.C. acknowledges financial support from MINECO (Spain) under project number AYA2012-31101. J.-P.K. and T.D. acknowledge support from the LIDA ERC advanced grant. A.R. acknowledges funding from the P2IO LabEx (ANR-10-LABX-0038) in the framework “Investissements d’Avenir” (ANR-11-IDEX-0003-01) managed by the French National Research Agency (ANR).

Table 1
The Ionization Potential^a

Atom	N_p	N_n	I \rightarrow II	II \rightarrow III	III \rightarrow IV	IV \rightarrow V	V \rightarrow VI	VI \rightarrow VII	VII \rightarrow VIII
H	1	0	13.59843
He	2	2	24.58739	54.41776
Li	3	4	5.391715	75.64009	122.4544
Be	4	5	9.322699	18.21115	153.8962	217.7186
B	5	6	8.298019	25.15483	37.93058	259.3715	340.2260
C	6	6	11.26030	24.3845	47.88778	64.49358	392.0905	489.9932	...
N	7	7	14.53413	29.60125	47.4453	77.4735	97.89013	552.0673	667.0461
O	8	8	13.61805	35.12111	54.93554	77.4135	113.8989	138.1189	739.3268
F	9	10	17.42282	34.97081	62.7080	87.175	114.249	157.1631	185.1868
Ne	10	10	21.56454	40.96296	63.4233	97.1900	126.247	157.934	207.271
Na	11	12	5.139077	47.28636	71.6200	98.936	138.404	172.23	208.504
Mg	12	12	7.646235	15.03527	80.1436	109.2654	141.33	186.76	225.02
Al	13	14	5.985768	18.82855	28.44764	119.9924	153.825	190.49	241.76
Si	14	14	8.151683	16.34585	33.493	45.14179	166.767	205.267	246.32
P	15	16	10.48669	19.76949	30.20264	51.44387	65.02511	220.430	263.57
S	16	16	10.36001	23.33788	34.86	47.222	72.5945	88.0529	280.954
Cl	17	18	12.96763	23.81364	39.80	53.24	67.68	96.94	114.2013
Ar	18	22	15.75961	27.62967	40.735	59.58	74.84	91.29	124.41
K	19	20	4.340664	31.625	45.8031	60.917	82.66	99.44	117.56
Ca	20	20	6.113155	11.87172	50.91315	67.2732	84.34	108.78	127.21
Sc	21	24	6.56149	12.79977	24.75684	73.4894	91.95	110.68	137.99
Ti	22	26	6.82812	13.5755	27.49171	43.26717	99.299	119.533	140.68
V	23	28	6.746187	14.618	29.3111	46.709	65.28165	128.125	150.72
Cr	24	28	6.76651	16.48630	30.959	49.16	69.46	90.6349	160.29
Mn	25	30	7.434018	15.63999	33.668	51.2	72.41	95.604	119.203
Fe	26	30	7.902468	16.1992	30.651	54.91	75.0	98.985	124.98
Co	27	32	7.88101	17.0844	33.50	51.27	79.50	102.0	128.9
Ni	28	31	7.639877	18.16884	35.187	54.92	76.06	108.0	132.0
Cu	29	35	7.72638	20.29239	36.841	57.38	79.8	103.0	139.0
Zn	30	35	9.394199	17.96439	39.7233	59.573	82.6	108.0	133.9

Note.

^a In units of eV. Data are taken from the NIST-ASD database (Kramida et al. 2014). Only the most abundant isotopes are included.

This paper represents an effort by both the SDSS-III and SDSS-IV collaborations. Funding for the Sloan Digital Sky Survey IV has been provided by the Alfred P. Sloan Foundation, the U.S. Department of Energy Office of Science, and the Participating Institutions. SDSS-IV acknowledges support and resources from the Center for High-Performance Computing at the University of Utah. The SDSS web site is www.sdss.org.

SDSS-IV is managed by the Astrophysical Research Consortium for the Participating Institutions of the SDSS Collaboration, including the Brazilian Participation Group, the Carnegie Institution for Science, Carnegie Mellon University, the Chilean Participation Group, the French Participation Group, Harvard-Smithsonian Center for Astrophysics, Instituto de Astrofísica de Canarias, The Johns Hopkins University, Kavli Institute for the Physics and Mathematics of the universe (IPMU)/University of Tokyo, Lawrence Berkeley National Laboratory, Leibniz Institut für Astrophysik Potsdam (AIP), Max-Planck-Institut für Astronomie (MPIA Heidelberg), Max-Planck-Institut für Astrophysik (MPA Garching), Max-Planck-Institut für Extraterrestrische Physik (MPE), National Astronomical Observatory of China, New Mexico State University, New York University, University of Notre Dame, Observatório Nacional/MCTI, The Ohio State University, Pennsylvania State University, Shanghai Astronomical Observatory, United Kingdom Participation Group, Universidad Nacional Autónoma de México, University of Arizona, University of Colorado Boulder, University of Oxford, University of Portsmouth,

University of Utah, University of Virginia, University of Washington, University of Wisconsin, Vanderbilt University, and Yale University.

Some of the data (Leitherer et al. 2011) are based on observations made with the NASA/ESA *Hubble Space Telescope*, obtained from the Data Archive at the Space Telescope Science Institute, which is operated by the Association of Universities for Research in Astronomy, Inc., under NASA contract NAS 5-26555.

APPENDIX A ATOMIC DATA

The spectroscopic analysis presented in this paper requires accurate atomic data. In this appendix, we present the data we gathered for completeness and future references.

We collect most of the data from the National Institute of Standards and Technology Atomic Spectra Database (NIST-ASD, Kramida et al. 2014) and have cross-checked the information with either the original or new references we found in the literature.

Most of the conventions used in spectroscopy are well established and we follow them whenever possible. However, we also found some ambiguous terms that may cause confusion, mostly due to historical reasons. We try to be as specific as possible on those occasions. We use Moore (1950, 1972), Cohen et al. (1987), and Draine (2011) as the main references. We briefly summarize the nomenclature we adopt

Table 2
The List of Lines Between 2200 and 7500 Å Associated with Star-forming Galaxies

Name	Wavelength Å (Vac.)	A_{ul} (s^{-1})	f_{lu}	E_l (cm^{-1})	E_u (cm^{-1})	Multiplet No.	References
Fe II λ 2250	2249.88	3.00E+06	1.82E-03	0	44446.905	UV5	(1), (2)
Fe II λ 2261	2260.78	3.18E+06	2.44E-03	0	44232.540	UV4	(1), (2)
Fe II* λ 2270	2269.52	4.00E+05	3.10E-04	384.7872	44446.905	UV5	(1), (2)
Fe II* λ 2281	2280.62	4.49E+06	4.38E-03	384.7872	44232.540	UV4	(1), (2)
C III λ 2298	2297.58	1.38E+08	1.82E-01	102352.04	145876.13	UV8	(3)
C II] λ 2324	2324.21	0	43025.3	UV0.01	(3), (4)
C II] λ 2325	2325.40	0	43003.3	UV0.01	(3), (4)
C II] λ 2326	2326.11	63.42	43053.6	UV0.01	(3), (4)
C II] λ 2328	2327.64	63.42	43025.3	UV0.01	(3), (4)
C II] λ 2329	2328.83	63.42	43003.3	UV0.01	(3), (4)
Fe II λ 2344	2344.21	1.73E+08	1.14E-01	0	42658.244	UV3	(1), (2)
Fe II* λ 2366	2365.55	5.90E+07	4.95E-02	384.7872	42658.244	UV3	(1), (2)
Fe II λ 2374	2374.46	4.25E+07	3.59E-02	0	42114.838	UV2	(1), (2)
Fe II* λ 2381	2381.49	3.10E+07	3.51E-02	667.6829	42658.244	UV3	(1), (2)
Fe II λ 2383	2382.76	3.13E+08	3.20E-01	0	41968.070	UV2	(1), (2)
Fe II* λ 2396	2396.35	2.59E+08	2.79E-01	384.7872	42114.838	UV2	(1), (2)
[Ne IV] λ 2423	2422.56	0	41278.89	UV1	(5)
[Ne IV] λ 2425	2425.14	0	41234.43	UV1	(5)
[O II] λ 2471.0	2470.97	0	40470.00	1.01F	(3), (6)
[O II] λ 2471.1	2471.09	0	40468.01	1.01F	(3), (6)
Mn II λ 2577	2576.88	2.80E+08	3.58E-01	0	38806.691	UV1	(7), (8), (9)
Fe II λ 2587	2586.65	8.94E+07	7.17E-02	0	38660.054	UV1	(1), (2)
Mn II λ 2594	2594.50	2.76E+08	2.79E-01	0	38543.122	UV1	(7), (8), (9)
Fe II λ 2600	2600.17	2.35E+08	2.39E-01	0	38458.993	UV1	(1), (2)
Mn II λ 2606	2606.46	2.69E+08	1.96E-01	0	38366.232	UV1	(7), (8), (9)
Fe II* λ 2613	2612.65	1.20E+08	1.22E-01	384.7872	38660.054	UV1	(1), (2)
Fe II* λ 2626	2626.45	3.52E+07	4.55E-02	384.7872	38458.993	UV1	(1), (2)
Fe II* λ 2632	2632.11	6.29E+07	8.70E-02	667.6829	38660.054	UV1	(1), (2)
Mg II λ 2796	2796.35	2.60E+08	6.08E-01	0	35760.88	UV1	(10), (11)
Mg II λ 2804	2803.53	2.57E+08	3.03E-01	0	35669.31	UV1	(10), (11)
Mg I λ 2853	2852.96	4.91E+08	1.80E-00	0	35051.264	UV1	(10), (11)
Ti II λ 3067	3067.24	3.47E+07	4.89E-02	0	32602.626	5	(10)
Ti II λ 3074	3073.86	1.71E+08	1.21E-01	0	32532.354	5	(10)
He I λ 3189	3188.67	5.64E+06	2.58E-02	159855.97	191217.05	3	(12)
Ti II λ 3230	3230.12	2.93E+07	6.87E-02	0	30958.585	2	(10)
Ti II λ 3243	3242.92	1.47E+08	2.32E-01	0	30836.425	2	(10)
Ti II λ 3385	3384.73	1.39E+08	3.58E-01	0	29544.454	1	(10)
[O II] λ 3727	3727.10	0	26830.57	1F	(3), (6)
[O II] λ 3730	3729.86	0	26810.55	1F	(3), (6)
[Ne III] λ 3870	3869.86	0	25840.72	1F	(13)
He I λ 3890	3889.74	9.47E+06	6.45E-02	159855.97	185564.60	2	(12)
[Ne III] λ 3969	3968.59	642.876	25840.72	1F	(13)
Ca II λ 3935	3934.77	1.40E+08	6.48E-01	0	25414.40	1	(14)
Ca II λ 3970	3969.59	1.36E+08	3.21E-01	0	25191.51	1	(14)
[S II] λ 4070	4069.75	0	24571.54	1F	(15)
[O III] λ 4364	4364.44	20273.27	43185.74	2F	(3), (6)
He I λ 4473	4472.76	2.46E+07	1.23E-01	169086.91	191444.48	14	(12)
[O III] λ 4960	4960.30	113.178	20273.27	1F	(3), (6)
[O III] λ 5008	5008.24	306.174	20273.27	1F	(3), (6)
[N I] λ 5199	5199.35	0	19233.177	1F	(3), (4)
[N I] λ 5202	5201.70	0	19224.464	1F	(3), (4)
Mg I λ 5169	5168.76	1.13E+07	1.35E-01	21850.405	41197.403	2	(10), (11)
Mg I λ 5174	5174.12	3.37E+07	1.35E-01	21870.464	41197.403	2	(10), (11)
Mg I λ 5185	5185.05	5.61E+07	1.36E-01	21911.178	41197.403	2	(10), (11)
He I λ 5877	5877.29	7.07E+07	6.10E-01	169086.91	186101.55	11	(12)
Na I λ 5892	5891.58	6.16E+07	6.41E-01	0	16973.366	1	(11)
Na I λ 5898	5897.56	6.14E+07	3.20E-01	0	16956.170	1	(11)
[O I] λ 6302	6302.05	0	15867.862	1F	(3), (6)
[O I] λ 6366	6365.54	158.265	15867.862	1F	(3), (6)
[O I] λ 6394	6393.50	226.977	15867.862	1F	(3), (6)
[N II] λ 6550	6549.86	48.7	15316.2	1F	(3), (4)
[N II] λ 6585	6585.27	130.8	15316.2	1F	(3), (4)
He I λ 6680	6680.00	6.37E+07	7.10E-01	171134.90	186104.96	46	(12)

Table 2
(Continued)

Name	Wavelength Å (Vac.)	A_{ul} (s^{-1})	f_{lu}	E_l (cm^{-1})	E_u (cm^{-1})	Multiplet No.	References
[S II] λ 6718	6718.29	0	14884.73	2F	(15)
[S II] λ 6733	6732.67	0	14852.94	2F	(15)
He I λ 7067	7067.20	2.78E+07	6.95E-02	169086.91	183236.79	10	(12)
[Ar III] λ 7138	7137.77	0	14010.00	1F	(16)
[O II] λ 7322	7322.01	26810.55	40468.01	2F	(3), (4)
[O II] λ 7332	7331.69	26830.57	40470.00	2F	(3), (4)
[O II] λ 7333	7332.75	26830.57	40468.01	2F	(3), (4)

References. (1) Fuhr & Wiese (2006), (2) Nave & Johansson (2013), (3) Gallagher & Moore (1993), (4) Wiese & Fuhr (2007), (5) Kramida et al. (1999), (6) Wiese et al. (1996), (7) Kramida & Sansonetti (2013), (8) Aldenius (2009), (9) Den Hartog et al. (2011), (10) Ruffoni & Pickering (2010), (11) Kelleher & Podobedova (2008), (12) Wiese & Fuhr (2009), (13) Kramida & Nave (2006), (14) Safronova & Safronova (2011), (15) Podobedova et al. (2009), (16) Saloman (2010).

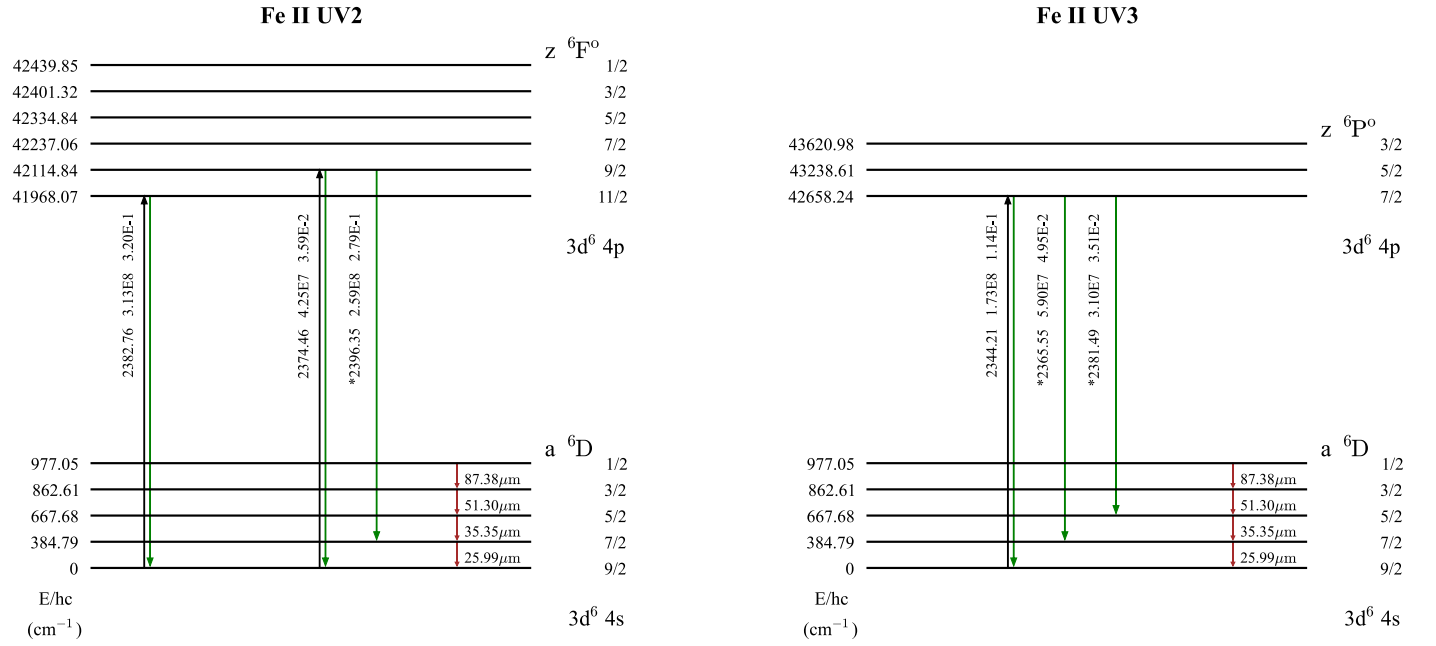


Figure 19. Energy-level diagrams for the Fe II UV2 and UV3 groups. The numbers next to the arrows represent the vacuum wavelength, the Einstein A coefficient, and the oscillator strength.

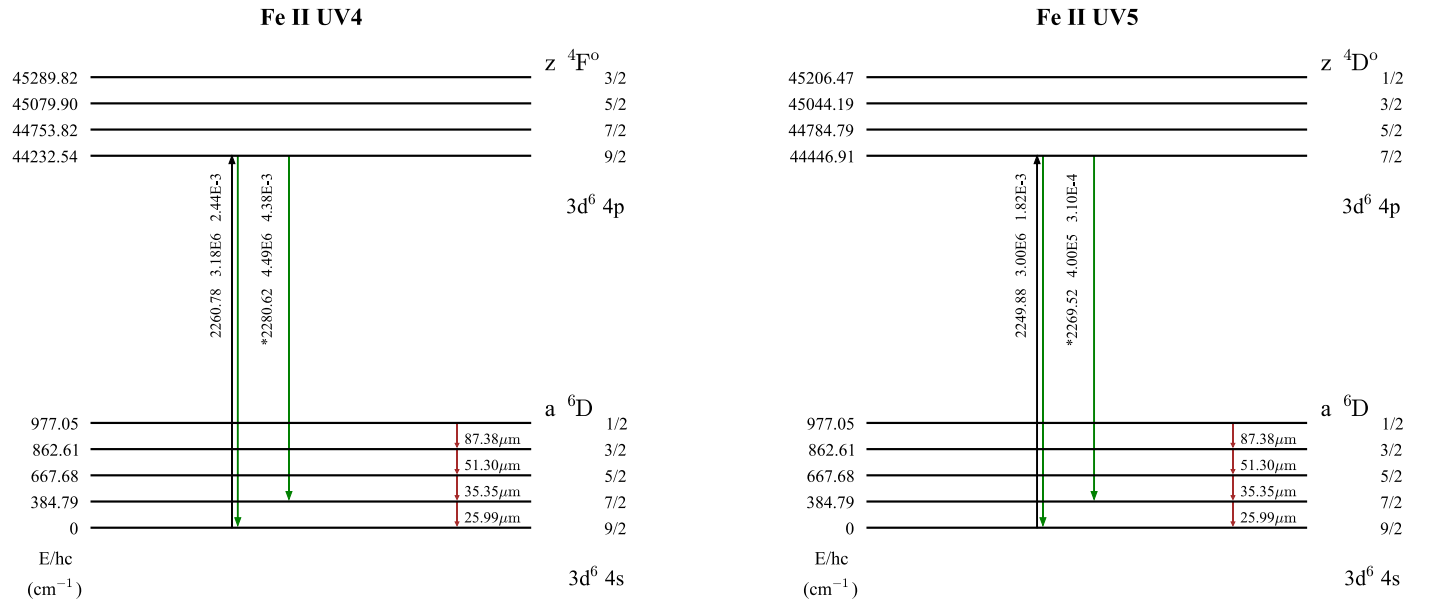


Figure 20. Energy-level diagrams for the Fe II UV4 and UV5 groups.

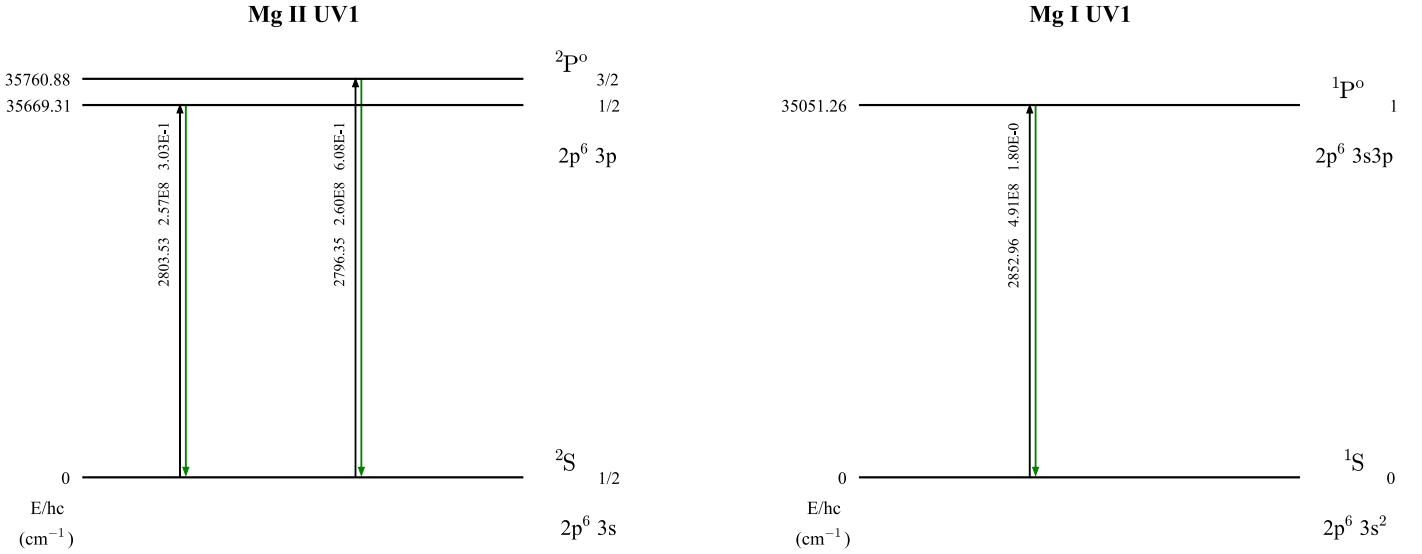


Figure 21. Energy-level diagrams for the Mg II UV1 and Mg I UV1 groups.

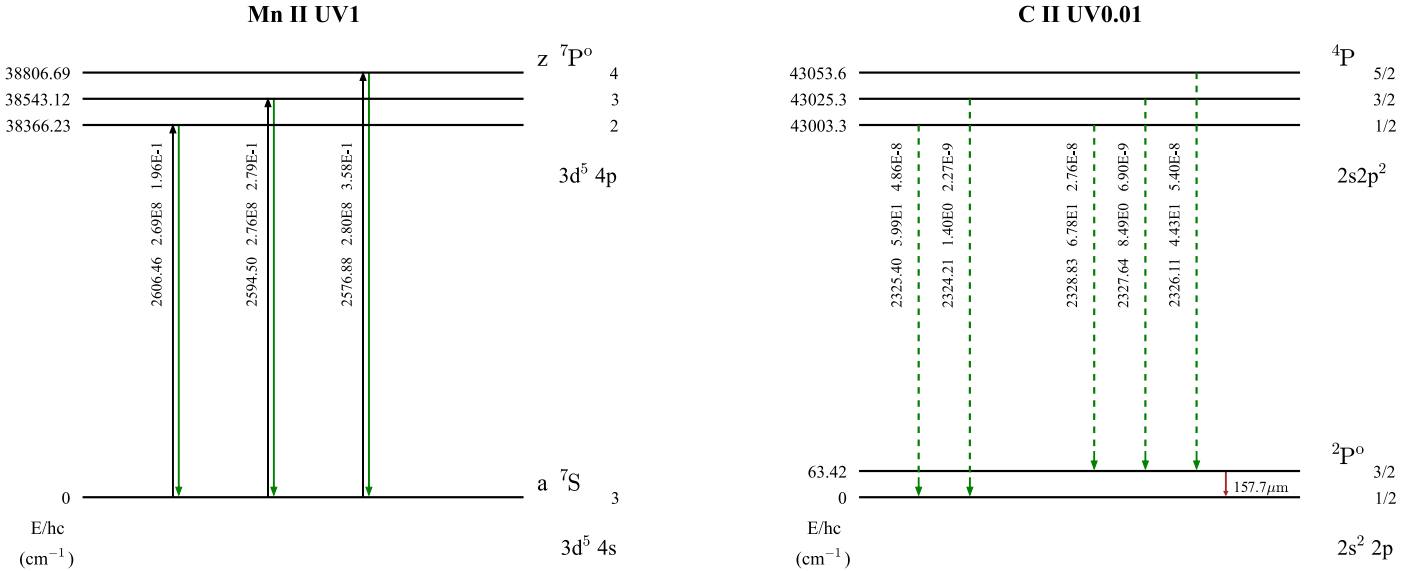


Figure 22. Energy-level diagrams for the Mn II UV1 and C II UV0.01 groups. Note that although we show the Einstein A coefficient and the Oscillator strength of the C II transitions, they are very low for these semi-forbidden lines.

below. We only include those definitions that are most relevant to our discussion or that may cause confusion. For a complete description, we refer the reader to the references above. We note our intention is not to give a comprehensive review or to resolve all the disagreements between the nomenclature in observational astronomy and that in quantum theory, but rather to make our presentation clear while maintaining consistency with the literature in astronomy.

A.1. Nomenclature

1. Roman numerals: To specify the spectrum of a z -fold ionized atom, we use a small capital roman numeral corresponding to $z+1$ written with a thin space following the chemical symbol. For example, H I denotes the spectrum of neutral hydrogen (H⁰), Mg II that of

singly ionized magnesium (Mg⁺), C III that of doubly ionized carbon (C²⁺). Recently, this convention has also been used by many authors to specify the ionized atom itself, not only the spectrum.

2. Electron configuration: an atomic electron configuration is indicated symbolically by

$$(nl)^k (n'l')^{k'} \quad (17)$$

in which k, k', \dots are the numbers of electrons with principal quantum numbers n, n', \dots and orbital angular momentum quantum numbers l, l', \dots , respectively. The orbital angular momentum numbers $l = 0, 1, 2, 3$, etc. are indicated by s, p, d, f, g, h, i, and k, and the parentheses are often omitted. For example, the electron configuration of the ground state of Fe⁺ is given by

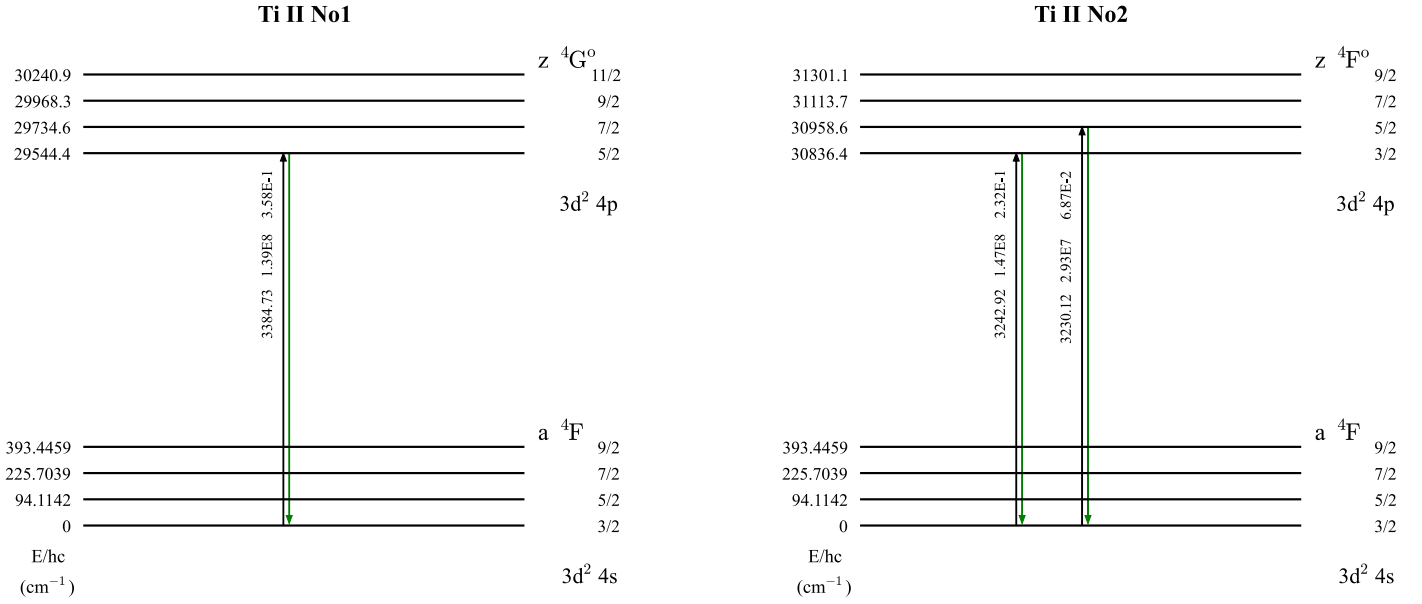


Figure 23. Energy-level diagrams for the Ti II No1 and No2 groups.

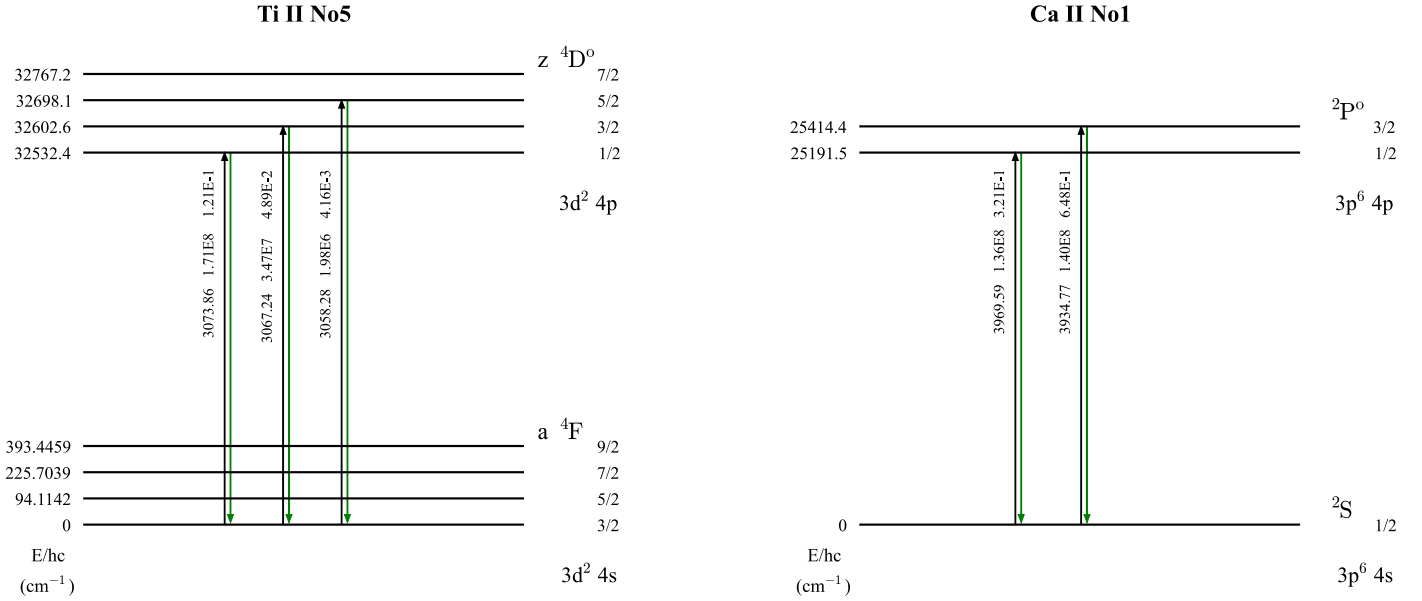


Figure 24. Energy-level diagrams for the Ti II No5 and Ca II No1 groups.

$1s^2 2s^2 2p^6 3s^2 3p^6 3d^6 4s$. In practice, we only show the last two or three subshells, e.g., $3d^6 4s$ for Fe^+ .

3. Spin-orbit (L - S) coupling: In L - S coupling, a given combination of (L , S) defines an atomic *term*. A given set of (L , S , J) defines an atomic *level*, and is indicated by

$$2S+1L_J^p, \quad (18)$$

where p represents parity and is blank for even parity and “o” for odd. Cohen et al. (1987) defines an atomic *state* as a level with a given set of L , S , J and M_J . We find that this definition is not used frequently in astronomy. In this paper, we use *term* and *state* interchangeably. We suggest using *microstate* or

quantum state for a given set of L , S , J and M_J (or L , S , M_S and M_L). With our choices, the ground *term* (*state*) of Fe^+ has $L=2$ (D) and $S=5/2$, with configuration $3d^6 4s$ and even parity, and is split into five *levels* with $J=1/2, 3/2, 5/2, 7/2, 9/2$, among which the lowest (ground) level is ${}^6\text{D}_{9/2}$. The first excited *term* (*state*) of Fe^+ (that is relevant in the NUV spectroscopy) has $L=2$ (D) and $S=5/2$, with configuration $3d^6 4p$ and odd parity, and is split into five *levels* with $J=1/2, 3/2, 5/2, 7/2, 9/2$, among which the lowest level is ${}^6\text{D}_{9/2}$. Note that each level has a degeneracy of $g=2J+1$ and the total multiplicity of a given term is $(2S+1)(2J+1)$.

For a multiple-(sub)shell system, there are multiple

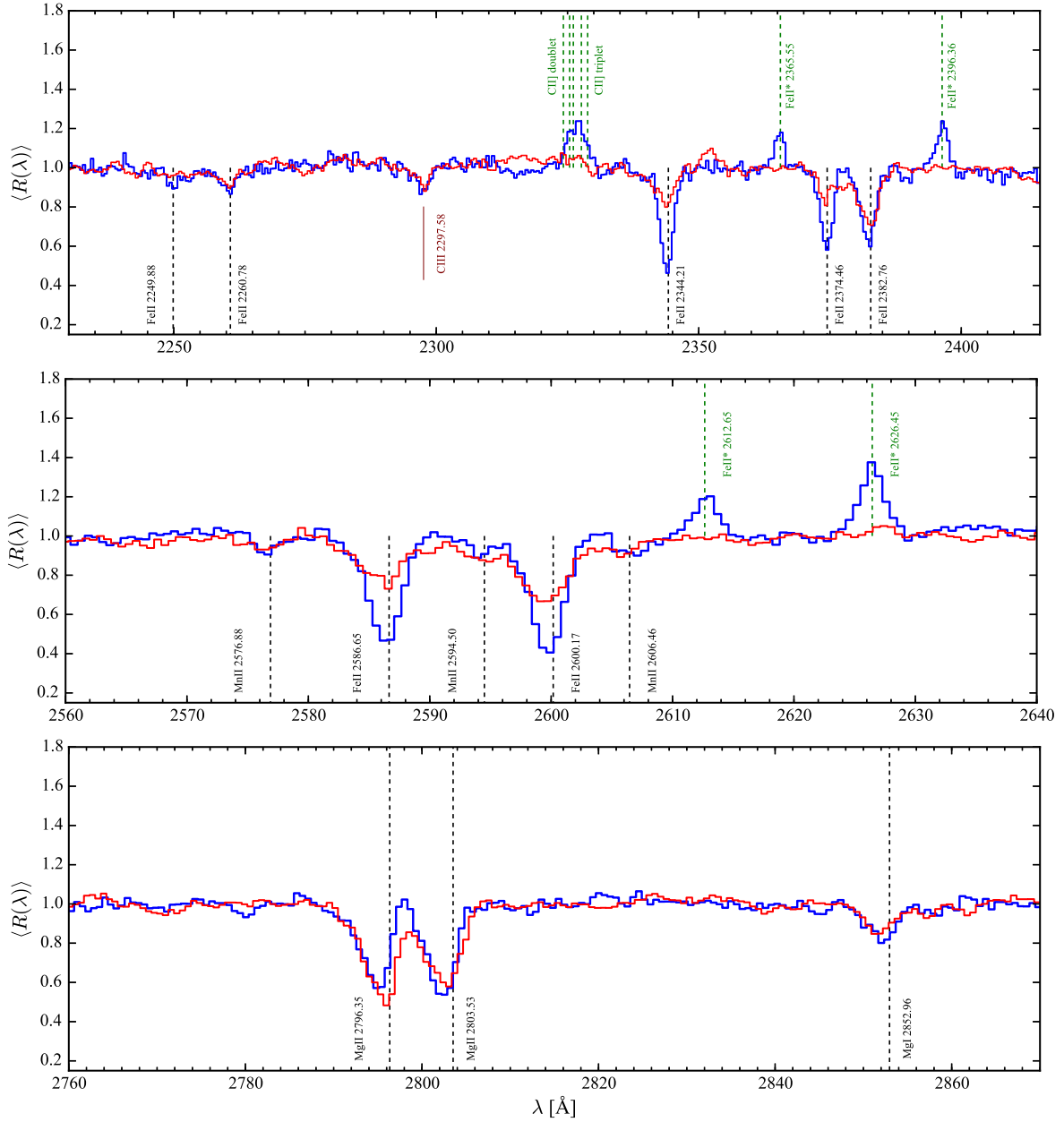


Figure 25. Composite continuum-normalized spectrum of 8620 ELGs at $0.6 < z < 1.2$ (blue) in eBOSS, compared with the composite spectrum of local star-forming regions (red) taken with the FOS/GHRS on *HST*.

terms with the same L and S for the outmost electron(s) due to different terms of electrons in the inner (sub) shells. Moore (1945) labeled different terms with a front lowercase letter “a”–“z” to distinguish them and this labeling method has been used since. We also use this convention, with the labeling letters extracted from the NIST-ASD database.

4. Resonance: we refer to a transition between two different terms as a resonant transition if and only if the lower level of the transition is the lowest level of the ground term. This definition is different from that given by Morton (2003), who considered transitions whose lower term is the ground term as resonant transitions, regardless of which level. For a permitted non-resonant transition, we label it with a right superscript asterisk “*.” Note that we

only apply this to permitted transitions, so forbidden (semi-forbidden) lines like [O III] $\lambda 5008$ (C II] $\lambda 2326$), although the lower energy level is not the lowest level, are labeled with the brackets “[]” (“]”) only.²⁷ We refer to a transition between two different levels, i.e., with different J -values, within the same term as a fine-structure transition. Fine-structure transitions are forbidden since the configuration does not change and thus $\Delta l = 0$.

²⁷ According to the selection rules, the transitions in Fe II UV4 and UV5 shown here, $\lambda 2250$, $\lambda 2261$, (*) $\lambda 2270$, and (*) $\lambda 2281$, are semi-forbidden. Because the selection rules apply to emission lines and historically Fe II lines were more often observed in absorption, these lines are usually not marked with “[].” Nonetheless, their transition probabilities are several orders-of-magnitude higher than other semi-forbidden lines. We treat them as permitted transitions here.

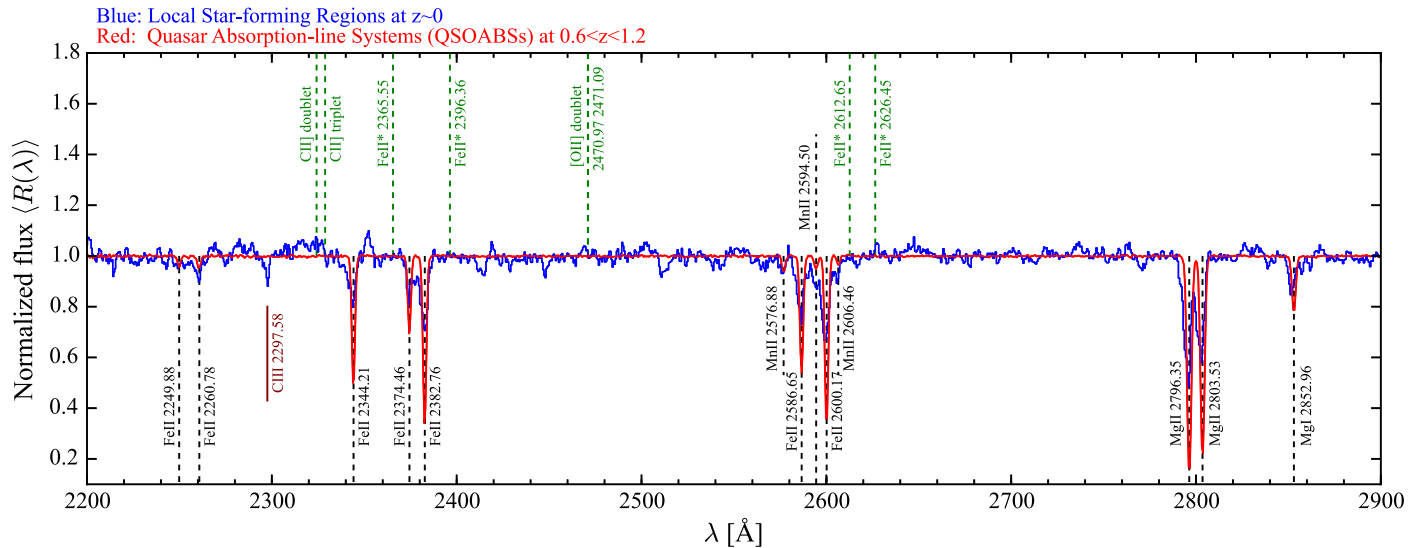


Figure 26. Composite continuum-normalized spectrum of local star-forming (SF) regions (blue), compared with the composite spectrum of intervening quasar absorption-line systems (QSOABSS) with $W_0^{\lambda 2796} > 2 \text{ \AA}$ at $0.6 < z < 1.2$ (red).

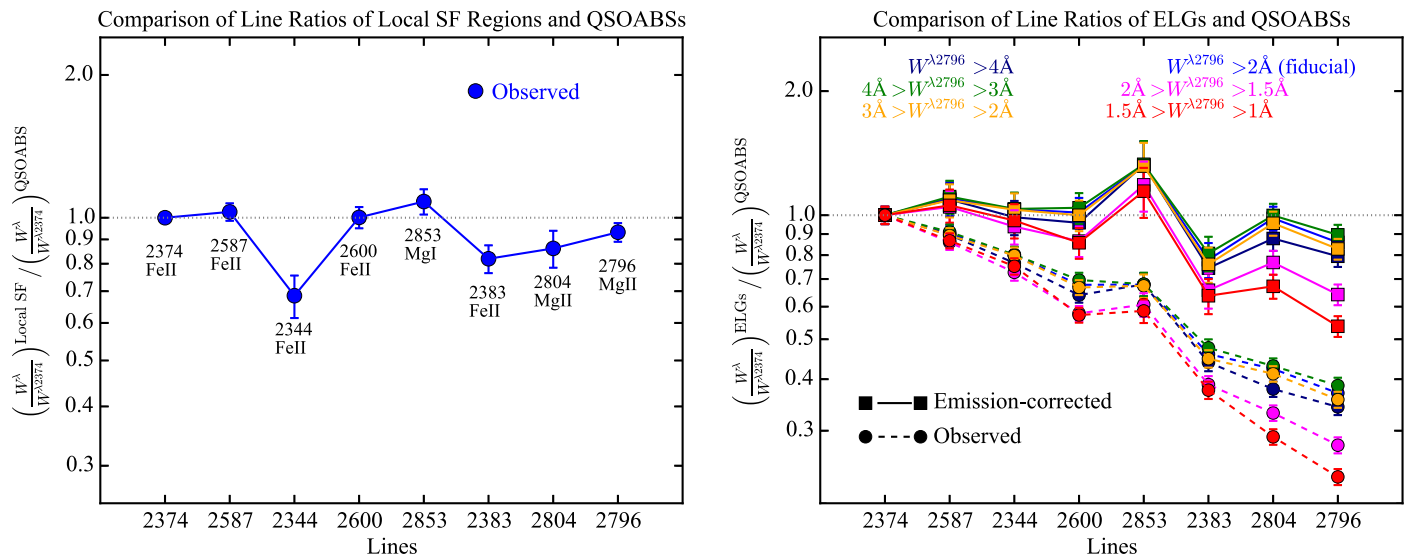


Figure 27. Left: comparison of line ratios of local SF regions with strong quasar absorbers (QSOABSs) with $W_0^{\lambda 2796} > 2 \text{ \AA}$ at $0.6 < z < 1.2$. The error bars show the uncertainties in the local SF regions determined by jackknife by removing one spectrum at a time. Right: comparison of observed (circles, dashed lines) and emission-corrected (squares, solid lines) line ratios of ELGs with quasar absorbers (QSOABSs) with different Mg II strengths (indicated by different colors). The error bars are bootstrapping errors of ELG line ratios.

5. Multiplet groups: Moore (1945) first labeled the multiplets in order of increasing excitation energy of the lower term then the higher term. At wavelength $\lambda \gtrsim 3000 \text{ \AA}$, the multiplets were included in the Revised Multiplet Table (Moore 1972), and at shorter wavelength in the Ultraviolet Multiplet Table (Moore 1950, 1952). Though the data have improved over the years, this convention has been used by many authors. Newly identified multiplet groups were usually added between the original groups by a decimal system (e.g., Gallagher & Moore 1993) and forbidden lines are denoted with “F” following the multiplet number. We notice that, in practice, the multiplet numbers are rarely used for transitions in the optical. Nonetheless, for consistency with the literature, we follow the same convention, and present the multiplet

numbers taken from Moore (1950, 1952, 1972) or new references we found in the literature.

A.2. Ionization Potentials

Table 1 presents the ionization potential for elements with atomic number up to 30, in unit of eV. We have included the most abundant isotopes ionized up to seven times. The columns N_p and N_n are the numbers of protons and neutrons. When available, we show seven significant figures.

A.3. Line List

In Table 2, we list the lines associated with SFGs between 2200 and 7500 Å. We detect most of them in the composite spectra of the ELGs from the eBOSS pilot observations. We do

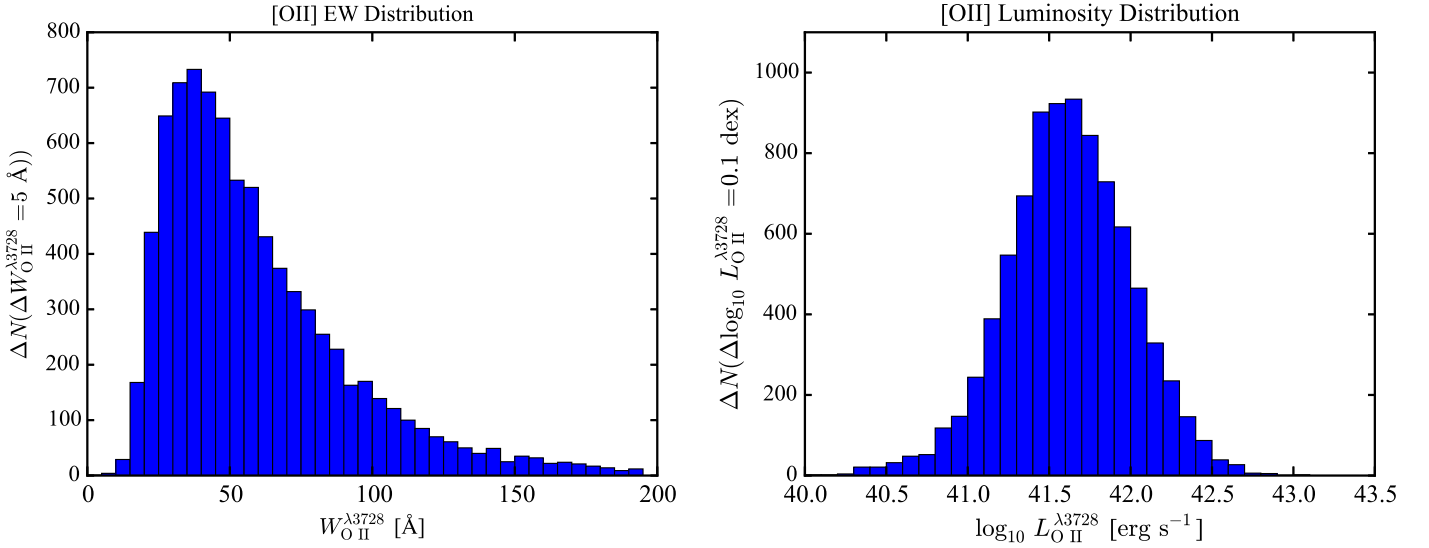


Figure 28. Distributions of the total [O II] $\lambda\lambda 3727, 3730$ rest equivalent width (left) and luminosity (right, in logarithmic scale). To calculate the luminosity, we assume the Λ CDM cosmological model.

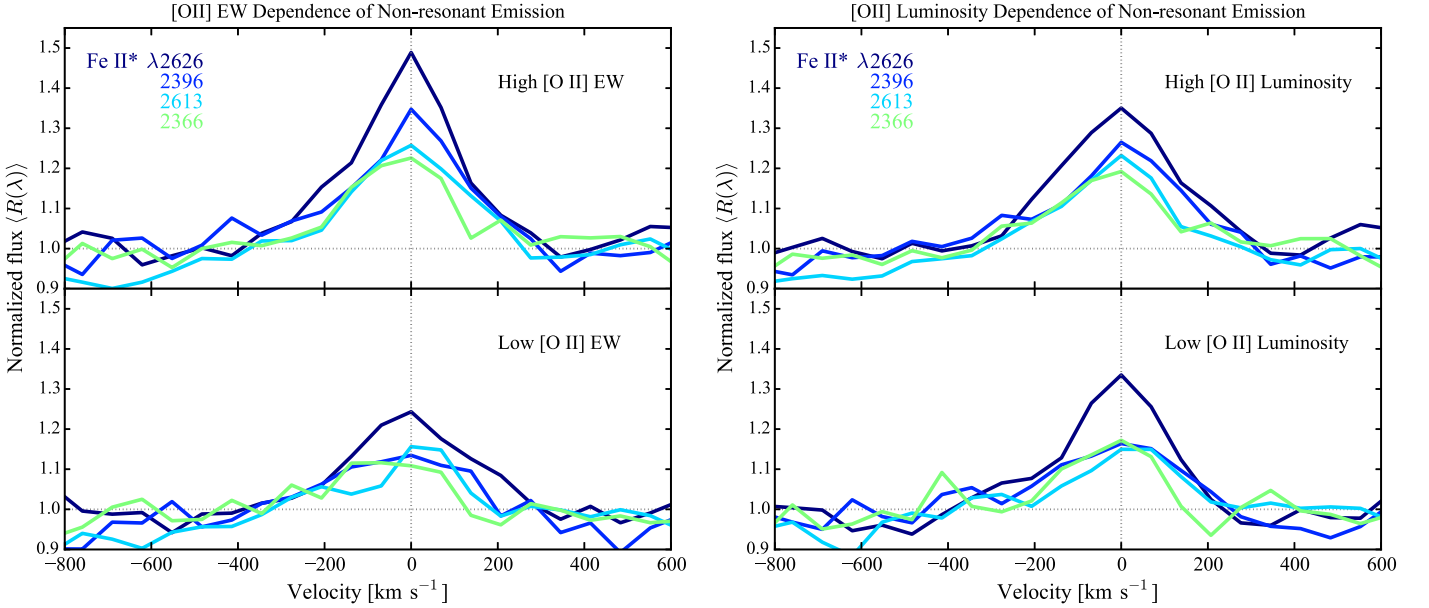


Figure 29. Dependences of the emission velocity profiles on the [O II] $\lambda\lambda 3727, 3730$ rest equivalent width (left) and luminosity (right).

not list the categories of origin and refer the reader to Section 3.3 for a summary of typical origins for the lines in the NUV. We present vacuum wavelength and some of the lines are therefore labeled as 1 \AA longer than if labeled with the air wavelength, such as [O III] $\lambda 5008$. For useful formulae for the conversion between vacuum and air wavelengths, we refer the reader to Ciddor (1996). We have omitted the hydrogen lines, a recent compilation of which can be found in Wiese & Fuhr (2009), and the G4300-band, which is a blend of many lines predominantly by CH and Fe I (e.g., Worthey et al. 1994).

For permitted transitions, we list the Einstein A coefficient (A_{ul}) and oscillator strength (f_{ul}), which are essential quantities for the radiative transfer analysis presented in this paper. For all the transitions, we list the energies of the lower (E_l) and higher levels (E_u), relative to the ground level (of the ground term). The energies are in units of cm^{-1} , and can be converted to eV

when multiplied by $1.2398\text{E-}4$. The transition wavelength (in \AA) can be derived with $1\text{E}8/(E_u - E_l)$.

A.4. Energy-level Diagrams

The relationships between the different resonant and non-resonant channels are essential to our analysis of radiative transfer processes. We illustrate these relationships with the energy-level diagrams of the corresponding multiplet groups. The diagram for the Fe II UV1 group is presented in Section 3.3 (Figure 5). Here we present those for Fe II UV2-UV5 (Figures 19 and 20), Mg II UV1 and Mg I UV1 (Figure 21). We also include C II UV0.01 and Mn II UV1 (Figure 22), Ti II No1, No2 and No5 (Figures 23 and 24), and Ca II No1 (Figure 24) as they merit further attention once we obtain more data in the near future. For other lines identified in the

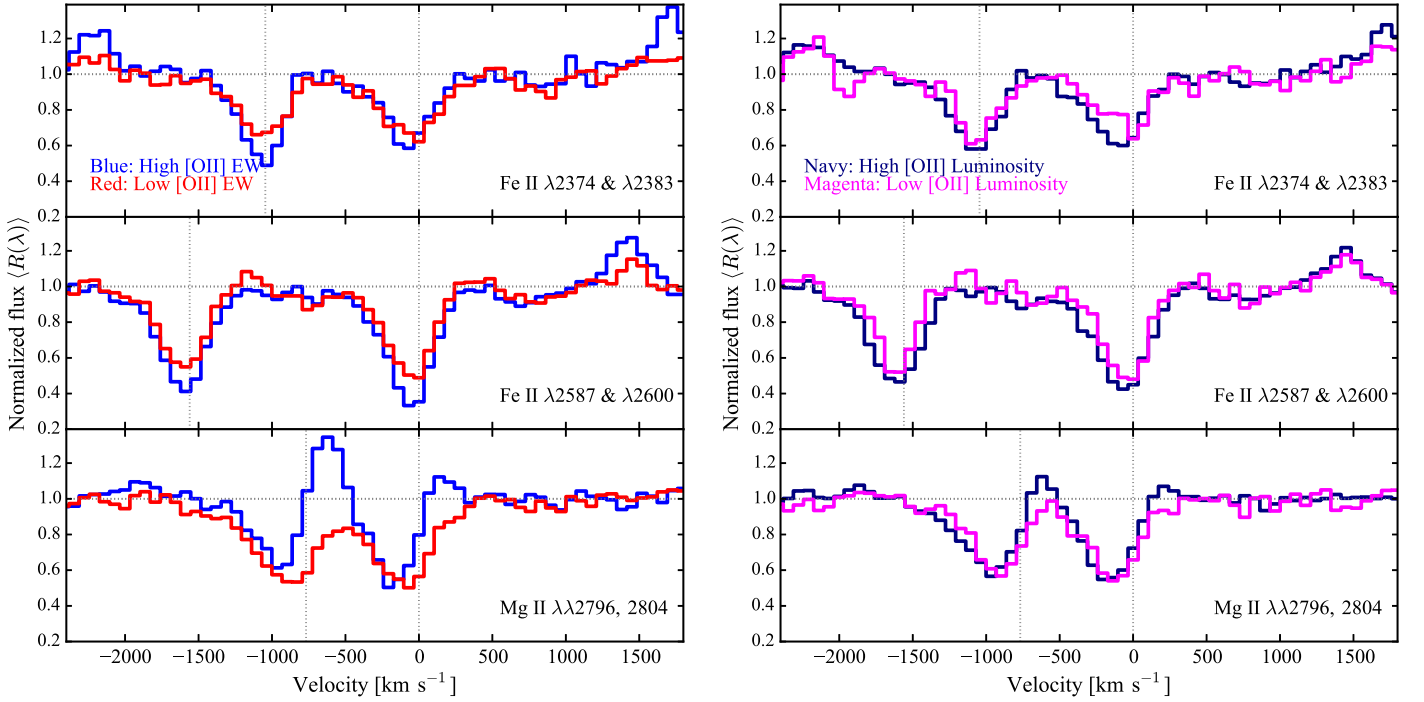


Figure 30. Dependences of the observed absorption velocity profiles on the [O II] $\lambda\lambda 3727$, 3730 rest equivalent width (left) and luminosity (right).

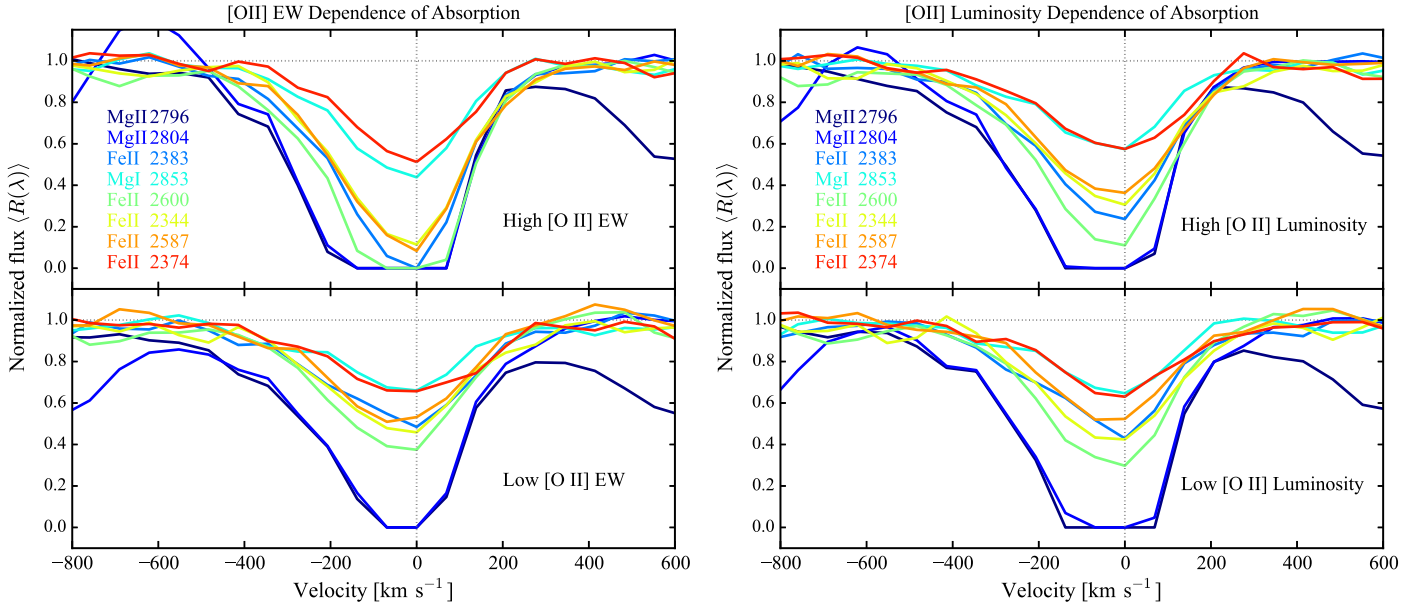


Figure 31. Dependences of the emission-corrected absorption velocity profiles on the [O II] $\lambda\lambda 3727$, 3730 rest equivalent width (left) and luminosity (right). The color scales are the same as in Figure 10, based on the orders given by Equations (13) and (14).

composite spectra of ELGs, such as [O II] $\lambda\lambda 2471.0$, 2471.1, their energy-level diagrams can be found in standard textbooks (e.g., Appendix E in Draine 2011).

The terms and symbols were introduced in the nomenclature above. For each transition, we show the vacuum wavelength, the Einstein A coefficient, and the oscillator strength. The black lines with upward arrows represent the observed absorption lines. The green lines with downward arrows show the observed or expected emission lines, with solid indicating permitted lines, dashed semi-forbidden (C II). The

brown lines with downward arrows represent fine-structure transitions.

APPENDIX B ADDITIONAL INFORMATION ABOUT THE SPECTRA OF DIFFERENT SOURCES

In Section 3.5, we compare the ELG composite spectrum (in blue) with the composite of the nine local SF regions (in red) at $2200 \text{ \AA} < \lambda < 2900 \text{ \AA}$ in Figure 6. In Figure 25, we zoom in on the most prominent features to show the details, as we did in

Figure 4 for the comparison with quasar absorption-line systems. Because the UV atlas by Leitherer et al. (2011) does not have wavelength coverage longer than 3200 Å, we do not compare the spectra at $3000 \text{ Å} < \lambda < 4000 \text{ Å}$ as in the bottom panel of Figure 4. As mentioned in Section 3.5, we have corrected the original wavelength in Leitherer et al. (2011) by -0.7 Å based on the position of $\text{C III } \lambda 2298$. The main differences are in the non-resonant emission lines and the absorption line ratios. See the main text for details.

In Figure 26, we present a comparison of the composite spectrum of the local SF regions and that of strong quasar absorbers. In the left panel of Figure 27, we show that the line ratios in the two composite spectra are very similar. Note that the abnormal behavior of $\text{Fe II } \lambda 2344$ is due to noises in the spectra of local SF regions since we have limited data from *HST* (only nine spectra).

In addition, in the right panel of Figure 27, we compare the observed and emission-corrected line ratios in the ELG spectra with the line ratios in the spectra of quasar absorbers with different Mg II strengths. We show that at $W_0^{\lambda 2796} > 2 \text{ Å}$, different selections have no effect on our conclusions in this paper. When we consider weaker quasar absorbers ($W_0^{\lambda 2796} < 2 \text{ Å}$), the Mg II -to- $\text{Fe II } \lambda 2374$ ratio in the ELG composite after emission correction appears to be slightly lower. However, our conclusion that the emission infill is significant does not change. We note that after emission correction, the Mg II absorption strength in the ELG composite is about 4 Å.

APPENDIX C

THE DEPENDENCES OF THE NUV FEATURES ON $[\text{O II}]$ EQUIVALENT WIDTH AND LUMINOSITY

The wavelength coverage of eBOSS allows us to study the dependences of the NUV features in the ELG spectra on the $[\text{O II}] \lambda \lambda 3727, 3730$ properties. We divide the NUV sample of 8620 ELGs into half subsamples based on the *total* rest equivalent width and luminosity of the $[\text{O II}] \lambda \lambda 3727, 3730$ doublet. In Section 5, we discuss in depth the emission strength, the observed absorption profiles of Mg II , the emission-corrected absorption strength, and the unified velocity profiles. Here we present some additional details of the analysis.

In Figure 28, we present the distributions of total rest equivalent width ($W_{[\text{O II}]}^{\lambda 3728}$) and luminosity (in logarithmic scale, $\log_{10} L_{[\text{O II}]}^{\lambda 3728}$). The median value of $W_{[\text{O II}]}^{\lambda 3728}$ is about 51.4 Å and the median of $\log_{10} L_{[\text{O II}]}^{\lambda 3728}$ is about 41.6 dex.

Figure 29 presents the observed velocity profiles of the non-resonant Fe II^* emission. The dependence on the $[\text{O II}]$ rest equivalent width is larger than on the luminosity.

We show examples of the *observed* absorption profiles for the different subsamples in Figure 30. The observed profiles are affected by the scattered emission filling in on top of the true absorption. The largest correlation is between the Mg II profiles and the $[\text{O II}]$ rest equivalent width, which we discuss in Section 5.

Figure 31 presents the emission-corrected absorption profiles, based on the observation-driven iterative method described in Section 4.2. We show the correlations between the rest equivalent width of the emission-corrected absorption with the $[\text{O II}] \lambda \lambda 3727, 3730$ properties in Figure 17.

REFERENCES

- Alam, S., Albareti, F. D., Allende Prieto, C., et al. 2015, *ApJS*, **219**, 12
- Aldenius, M. 2009, *PhST*, **134**, 014008
- Asplund, M., Grevesse, N., Sauval, A. J., & Scott, P. 2009, *ARA&A*, **47**, 481
- Baldwin, J. A., Phillips, M. M., & Terlevich, R. 1981, *PASP*, **93**, 5
- Bell, E. F., Wolf, C., Meisenheimer, K., et al. 2004, *ApJ*, **608**, 752
- Bergeron, J. 1986, *A&A*, **155**, L8
- Bergeron, J., & Boissé, P. 1991, *A&A*, **243**, 344
- Blair, W. P., & Panagia, N. 1987, in *Exploring the Universe with the IUE Satellite*, Vol. 129 (Dordrecht: Reidel), 549
- Bland, J., & Tully, B. 1988, *Natur*, **334**, 43
- Bolton, A. S., Schlegel, D. J., Aubourg, É., et al. 2012, *AJ*, **144**, 144
- Bordoloi, R., Lilly, S. J., Knobel, C., et al. 2011, *ApJ*, **743**, 10
- Bordoloi, R., Tumlinson, J., Werk, J. K., et al. 2014, *ApJ*, **796**, 136
- Borthakur, S., Heckman, T., Strickland, D., Wild, V., & Schiminovich, D. 2013, *ApJ*, **768**, 18
- Bouché, N., Murphy, M. T., Péroux, C., et al. 2007, *ApJL*, **669**, L5
- Burbidge, E. M., & Kinman, T. D. 1966, *ApJ*, **145**, 654
- Castelli, F., Gratton, R. G., & Kurucz, R. L. 1997, *A&A*, **318**, 841
- Castor, J. I. 1970, *MNRAS*, **149**, 111
- Chevalier, R. A., & Clegg, A. W. 1985, *Natur*, **317**, 44
- Churchill, C. W., Mellon, R. R., Charlton, J. C., et al. 2000, *ApJS*, **130**, 91
- Ciddor, P. E. 1996, *ApOpt*, **35**, 1566
- Cohen, E. R., Giacomo, P., Commission, P., et al. 1987, *Symbols, Units, Nomenclature and Fundamental Constants in Physics* (Amsterdam: North-Holland)
- Cole, S., Percival, W. J., Peacock, J. A., et al. 2005, *MNRAS*, **362**, 505
- Comparat, J., Delubac, T., Jovel, S., et al. 2015a, arXiv: 1509.05045
- Comparat, J., Kneib, J.-P., Bacon, R., et al. 2013, *A&A*, **559**, A18
- Comparat, J., Richard, J., Kneib, J.-P., et al. 2015b, *A&A*, **575**, A40
- Croton, D. J., Springel, V., White, S. D. M., et al. 2006, *MNRAS*, **365**, 11
- Dalgarno, A., & McCray, R. A. 1972, *ARA&A*, **10**, 375
- Dawson, K. S., Kneib, J.-P., Percival, W. J., et al. 2015, arXiv:1508.04473
- Dawson, K. S., Schlegel, D. J., Ahn, C. P., et al. 2013, *AJ*, **145**, 10
- Den Hartog, E. A., Lawler, J. E., Sobek, J. S., Sneden, C., & Cowan, J. J. 2011, *ApJS*, **194**, 35
- Dey, A., Torrey, P., Rubin, K. H. R., Zhu, G. B., & Suresh, J. 2015, *MNRAS*, **451**, 1806
- Draine, B. T. 2011, *Physics of the Interstellar and Intergalactic Medium* (Princeton, NJ: Princeton Univ. Press)
- Dufour, R. J. 1987, in *Exploring the Universe with the IUE Satellite*, Vol. 129 (Dordrecht: Reidel), 577
- Eisenstein, D. J., Annis, J., Gunn, J. E., et al. 2001, *AJ*, **122**, 2267
- Eisenstein, D. J., Weinberg, D. H., Agol, E., et al. 2011, *AJ*, **142**, 72
- Eisenstein, D. J., Zehavi, I., Hogg, D. W., et al. 2005, *ApJ*, **633**, 560
- Erb, D. K., Quider, A. M., Henry, A. L., & Martin, C. L. 2012, *ApJ*, **759**, 26
- Faber, S. M., Willmer, C. N. A., Wolf, C., et al. 2007, *ApJ*, **665**, 265
- Fanelli, M. N., O'Connell, R. W., Burstein, D., & Wu, C.-C. 1992, *ApJS*, **82**, 197
- Flaugher, B. L., Abbott, T. M. C., Angstadt, R., et al. 2012, *Proc. SPIE*, **8446**, 844611
- Francis, P. J., Hewett, P. C., Foltz, C. B., et al. 1991, *ApJ*, **373**, 465
- Fuhr, J. R., & Wiese, W. L. 2006, *JPCRD*, **35**, 1669
- Fukugita, M., Ichikawa, T., Gunn, J. E., et al. 1996, *AJ*, **111**, 1748
- Gallagher, J., & Moore, C. E. 1993, *Tables of Spectra of Hydrogen, Carbon, Nitrogen, and Oxygen Atoms and Ions* (Boca Raton, FL: CRC Press)
- Gunn, J. E., Carr, M., Rockosi, C., et al. 1998, *AJ*, **116**, 3040
- Gunn, J. E., Siegmund, W. A., Mannery, E. J., et al. 2006, *AJ*, **131**, 2332
- Heckman, T. M. 1980, *A&A*, **87**, 152
- Heckman, T. M., Alexandroff, R. M., Borthakur, S., Overzier, R., & Leitherer, C. 2015, *ApJ*, **809**, 147
- Heckman, T. M., Armus, L., & Miley, G. K. 1990, *ApJS*, **74**, 833
- Heckman, T. M., Lehnert, M. D., Strickland, D. K., & Armus, L. 2000, *ApJS*, **129**, 493
- Ho, L. C., Filippenko, A. V., & Sargent, W. L. W. 1997, *ApJ*, **487**, 568
- Hopkins, A. M. 2004, *ApJ*, **615**, 209
- Jones, T., Stark, D. P., & Ellis, R. S. 2012, *ApJ*, **751**, 51
- Jovel, S., Delubac, T., Comparat, J., et al. 2015, arXiv:1509.07121
- Kelleher, D. E., & Podobedova, L. I. 2008, *JPCRD*, **37**, 267
- Kennicutt, R. C., Jr. 1992, *ApJ*, **388**, 310
- Kinney, A. L., Bohlin, R. C., Calzetti, D., Panagia, N., & Wyse, R. F. G. 1993, *ApJS*, **86**, 5
- Koeppen, J., & Aller, L. H. 1987, in *Exploring the Universe with the IUE Satellite*, Vol. 129 (Dordrecht: Reidel), 589
- Kornei, K. A., Shapley, A. E., Martin, C. L., et al. 2012, *ApJ*, **758**, 135

- Kornei, K. A., Shapley, A. E., Martin, C. L., et al. 2013, *ApJ*, **774**, 50
- Kramida, A., Ralchenko, Y., Reader, J. & NIST ASD Team 2014, NIST Atomic Spectra Database (ver. 5.2), [Online] Available: <http://physics.nist.gov/asd> [2015, June 25]. National Institute of Standards and Technology, Gaithersburg, MD
- Kramida, A., & Sansonetti, J. E. 2013, *ApJS*, **205**, 14
- Kramida, A. E., Bastin, T., Biémont, E., Dumont, P.-D., & Garnir, H.-P. 1999, *EPJD*, **7**, 525
- Kramida, A. E., & Nave, G. 2006, *EPJD*, **37**, 1
- Kurucz, R. L. 1992, in IAU Symp. 149, The Stellar Populations of Galaxies, ed. B. Barbuy & A. Renzini (Dordrecht: Kluwer), 225
- Lan, T.-W., Ménard, B., & Zhu, G. 2014, *ApJ*, **795**, 31
- Lang, D., Hogg, D. W., & Schlegel, D. J. 2014, arXiv:1410.7397
- Leitherer, C., Tremonti, C. A., Heckman, T. M., & Calzetti, D. 2011, *AJ*, **141**, 37
- Levesque, E. M., & Richardson, M. L. A. 2014, *ApJ*, **780**, 100
- Levi, M., Bebek, C., Beers, T., et al. 2013, arXiv: 1308.0847
- Lynds, C. R., & Sandage, A. R. 1963, *ApJ*, **137**, 1005
- Madau, P., & Dickinson, M. 2014, *ARA&A*, **52**, 415
- Madau, P., Ferguson, H. C., Dickinson, M. E., et al. 1996, *MNRAS*, **283**, 1388
- Martin, C. L. 2005, *ApJ*, **621**, 227
- Martin, C. L., & Bouché, N. 2009, *ApJ*, **703**, 1394
- Martin, C. L., Shapley, A. E., Coil, A. L., et al. 2012, *ApJ*, **760**, 127
- Martin, C. L., Shapley, A. E., Coil, A. L., et al. 2013, *ApJ*, **770**, 41
- Mathis, J. S. 1972, *ApJ*, **176**, 651
- McKee, C. F., & Ostriker, J. P. 1977, *ApJ*, **218**, 148
- Miller, S. H., Bundy, K., Sullivan, M., Ellis, R. S., & Treu, T. 2011, *ApJ*, **741**, 115
- Moore, C. E. 1945, CoPri, **20**, 1
- Moore, C. E. 1950, NBS Circular (Washington: US Government Printing Office (USGPO))
- Moore, C. E. 1952, NBS Circular (Washington: US Government Printing Office (USGPO)) c1952
- Moore, C. E. 1972, NSRDS-NBS (Washington: US Department of Commerce) Rev. edition
- Morrison, N. D. 1975, *ApJ*, **202**, 433
- Morton, D. C. 2003, *ApJS*, **149**, 205
- Moustakas, J., Coil, A. L., Aird, J., et al. 2013, *ApJ*, **767**, 50
- Murga, M., Zhu, G., Ménard, B., & Lan, T.-W. 2015, *MNRAS*, **452**, 511
- Murray, N., Ménard, B., & Thompson, T. A. 2011, *ApJ*, **735**, 66
- Murray, N., Quataert, E., & Thompson, T. A. 2005, *ApJ*, **618**, 569
- Nagao, T., Maiolino, R., & Marconi, A. 2006, *A&A*, **459**, 85
- Nath, B. B., & Silk, J. 2009, *MNRAS*, **396**, L90
- Nave, G., & Johansson, S. 2013, *ApJS*, **204**, 1
- Nestor, D. B., Johnson, B. D., Wild, V., et al. 2011, *MNRAS*, **412**, 1559
- Norman, C. A., Bowen, D. V., Heckman, T., Blades, C., & Danly, L. 1996, *ApJ*, **472**, 73
- Peeples, M. S., Werk, J. K., Tumlinson, J., et al. 2014, *ApJ*, **786**, 54
- Pettini, M., Shapley, A. E., Steidel, C. C., et al. 2001, *ApJ*, **554**, 981
- Pineda, J. L., Langer, W. D., Velusamy, T., & Goldsmith, P. F. 2013, *A&A*, **554**, A103
- Podobedova, L. I., Kelleher, D. E., & Wiese, W. L. 2009, *JPCRD*, **38**, 171
- Prochaska, J. X., Kasen, D., & Rubin, K. 2011, *ApJ*, **734**, 24
- Raichoor, A., Comparat, J., Delubac, T., et al. 2015, arXiv:1505.01797
- Reynolds, R. J. 1984, *ApJ*, **282**, 191
- Rodríguez-Merino, L. H., Chavez, M., Bertone, E., & Buzzoni, A. 2005, *ApJ*, **626**, 411
- Rubin, K. H. R., Prochaska, J. X., Koo, D. C., et al. 2014, *ApJ*, **794**, 156
- Rubin, K. H. R., Prochaska, J. X., Koo, D. C., & Phillips, A. C. 2012, *ApJL*, **747**, L26
- Rubin, K. H. R., Prochaska, J. X., Koo, D. C., Phillips, A. C., & Weiner, B. J. 2010, *ApJ*, **712**, 574
- Rubin, K. H. R., Prochaska, J. X., Ménard, B., et al. 2011, *ApJ*, **728**, 55
- Ruffoni, M. P., & Pickering, J. C. 2010, *ApJ*, **725**, 424
- Rupke, D. S., Veilleux, S., & Sanders, D. B. 2005, *ApJS*, **160**, 115
- Rybicki, G. B., & Hummer, D. G. 1978, *ApJ*, **219**, 654
- Safronova, M. S., & Safronova, U. I. 2011, *PhRvA*, **83**, 012503
- Saloman, E. B. 2010, *JPCRD*, **39**, 033101
- Scarlata, C., & Panagia, N. 2015, *ApJ*, **801**, 43
- Schlegel, D., Abdalla, F., Abraham, T., et al. 2011, arXiv:1106.1706
- Schmidt, M. 1963, *Natur*, **197**, 1040
- Shapley, A. E., Steidel, C. C., Pettini, M., & Adelberger, K. L. 2003, *ApJ*, **588**, 65
- Silk, J., & Rees, M. J. 1998, *A&A*, **331**, L1
- Smee, S. A., Gunn, J. E., Uomoto, A., et al. 2013, *AJ*, **146**, 32
- Sobolev, V. V. 1960, Moving Envelopes of Stars (Cambridge: Harvard Univ. Press)
- Sobral, D., Matthee, J., Best, P. N., et al. 2015, arXiv:1502.06602
- Somerville, R. S., Hopkins, P. F., Cox, T. J., Robertson, B. E., & Hernquist, L. 2008, *MNRAS*, **391**, 481
- Stacey, G. J., Hailey-Dunsheath, S., Ferkinhoff, C., et al. 2010, *ApJ*, **724**, 957
- Steidel, C. C., Erb, D. K., Shapley, A. E., et al. 2010, *ApJ*, **717**, 289
- Steidel, C. C., Giallisco, M., Pettini, M., Dickinson, M., & Adelberger, K. L. 1996, *ApJL*, **462**, L17
- Steidel, C. C., & Sargent, W. L. W. 1992, *ApJS*, **80**, 1
- Stocke, J. T., Keeney, B. A., Danforth, C. W., et al. 2013, *ApJ*, **763**, 148
- Strömberg, B. 1939, *ApJ*, **89**, 526
- Takada, M., Ellis, R. S., Chiba, M., et al. 2014, *PASJ*, **66**, R1
- Talia, M., Mignoli, M., Cimatti, A., et al. 2012, *A&A*, **539**, A61
- Tang, Y., Giallisco, M., Guo, Y., & Kurk, J. 2014, *ApJ*, **793**, 92
- Thom, C., Tumlinson, J., Werk, J. K., et al. 2012, *ApJL*, **758**, L41
- Tielens, A. G. G. M., & Hollenbach, D. 1985, *ApJ*, **291**, 722
- Tremonti, C. A., Moustakas, J., & Diamond-Stanic, A. M. 2007, *ApJL*, **663**, L77
- Trouille, L., Barger, A. J., & Tremonti, C. 2011, *ApJ*, **742**, 46
- Tumlinson, J., Thom, C., Werk, J. K., et al. 2011, *Sci*, **334**, 948
- Vanden Berk, D. E., Richards, G. T., Bauer, A., et al. 2001, *AJ*, **122**, 549
- Veilleux, S., Cecil, G., & Bland-Hawthorn, J. 2005, *ARA&A*, **43**, 769
- Vogt, N. P., Forbes, D. A., Phillips, A. C., et al. 1996, *ApJL*, **465**, L15
- Weiner, B. J., Coil, A. L., Prochaska, J. X., et al. 2009, *ApJ*, **692**, 187
- Weiner, B. J., Willmer, C. N. A., Faber, S. M., et al. 2006, *ApJ*, **653**, 1049
- Werk, J. K., Prochaska, J. X., Tumlinson, J., et al. 2014, *ApJ*, **792**, 8
- Wiese, W. L., & Fuhr, J. R. 2007, *JPCRD*, **36**, 1287
- Wiese, W. L., & Fuhr, J. R. 2009, *JPCRD*, **38**, 565
- Wiese, W. L., Fuhr, J. R., & Deters, T. M. (ed.) 1996, Atomic Transition Probabilities of Carbon, Nitrogen, and Oxygen: A Critical Data Compilation (Washington, DC: American Chemical Society)
- Williams, R. J., Quadri, R. F., Franx, M., et al. 2010, *ApJ*, **713**, 738
- Worthey, G., Faber, S. M., Gonzalez, J. J., & Burstein, D. 1994, *ApJS*, **94**, 687
- Wright, E. L., Eisenhardt, P. R. M., Mainzer, A. K., et al. 2010, *AJ*, **140**, 1868
- Wuyts, S., Förster Schreiber, N. M., Genzel, R., et al. 2012, *ApJ*, **753**, 114
- Yan, R., Ho, L. C., Newman, J. A., et al. 2011, *ApJ*, **728**, 38
- Zhao, G. B., Wang, Y., Ross, A. J., et al. 2015, arXiv:1510.08216
- Zhu, G., & Ménard, B. 2013a, *ApJ*, **770**, 130
- Zhu, G., & Ménard, B. 2013b, *ApJ*, **773**, 16
- Zhu, G., Ménard, B., Bizyaev, D., et al. 2014, *MNRAS*, **439**, 3139
- Zhu, G., Moustakas, J., & Blanton, M. R. 2009, *ApJ*, **701**, 86